

**KONYA FOOD AND AGRICULTURE UNIVERSITY
THE GRADUATE SCHOOL OF NATURAL AND
APPLIED SCIENCES
COMPUTER ENGINEERING**

**MULTIPLICATIVE NOISE REDUCTION USING
VARIATIONAL METHODS**

MASTER OF SCIENCE THESIS

GÜLAY AKSOY

**KONYA
AUGUST, 2019**

**KONYA FOOD AND AGRICULTURE UNIVERSITY
THE GRADUATE SCHOOL OF NATURAL AND
APPLIED SCIENCES**

**MULTIPLICATIVE NOISE REDUCTION USING
VARIATIONAL METHODS**

GÜLAY AKSOY

**Thesis Advisor: Assist. Prof. Dr. Fatih NAR
Computer Engineering**

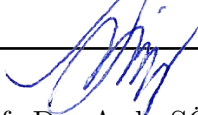
**KONYA
AUGUST, 2019**

I certify that I have read this thesis and that in my opinion it is fully adequate, in scope and in quality, as a thesis of the degree of Master



Assist. Prof. Dr. Fatih NAR (Advisor)

I certify that I have read this thesis and that in my opinion it is fully adequate, in scope and in quality, as a thesis of the degree of Master



Assist. Prof. Dr. Arda SÖYLEV

I certify that I have read this thesis and that in my opinion it is fully adequate, in scope and in quality, as a thesis of the degree of Master



Assist. Prof. Dr. Burak ALTINOKLU

I certify that I have read this thesis and that in my opinion it is fully adequate, in scope and in quality, as a thesis of the degree of Master



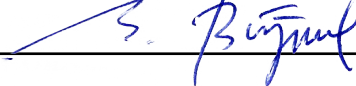
Assist. Prof. Dr. Zafer ARICAN

I certify that I have read this thesis and that in my opinion it is fully adequate, in scope and in quality, as a thesis of the degree of Master



Dr. Atilla ÖZGÜR

I certify that I have read this thesis and that in my opinion it is fully adequate, in scope and in quality, as a thesis of the degree of Master



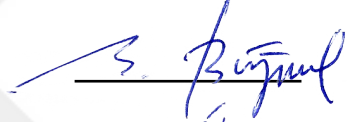
Prof. Dr. Sencer BUZRUL
Director of the Institute of Natural and Applied Sciences

Approval of the thesis:

MULTIPLICATIVE NOISE REDUCTION USING VARIATIONAL METHODS

This study titled “Multiplicative Noise Reduction Using Variational Methods” and presented as master thesis by **GÜLAY AKSOY** has been evaluated in compliance with the relevant provisions of KFAU Graduate Education and Training Regulation and KFAU Institute of Science Education and Training Direction and jury members written below have decided for the defence of this thesis and it has been declared by consensus / majority of votes that the candidate has succeeded in thesis defence examination dated.

Prof. Dr. Sencer BUZRUL
Director, **Institute of Natural and Applied Science**



Assist. Prof. Dr. Arda SÖYLEV
Head of Department, **Computer Engineering**



Assist. Prof. Dr. Fatih NAR
Supervisor, **Computer Engineering, KGTU**



Examining Committee Members:

Assist. Prof. Dr. Arda SÖYLEV
Computer Engineering, KGTU



Assist. Prof. Dr. Fatih NAR
Computer Engineering, KGTU



Assist. Prof. Dr. Burak ALTINOKLU
Electrical-Electronics Engineering, KGTU



Assist. Prof. Dr. Zafer ARICAN
Electrical-Electronics Engineering, KGTU



Dr. Atilla ÖZGÜR
Logistics Engineering, Jacobs University



Date: 06.08.2019

ÖZET

DEĞİŞİMSEL YÖNTEMLERLE ÇARPIMSAL GÜRÜLTÜ AZALTIMI

AKSOY, Gülay

Yüksek Lisans, Bilgisayar Mühendisliği Bölümü

Tez Yöneticisi: Dr. Öğr. Üyesi. Fatih NAR

Ağustos 2019, 91 sayfa

Sentetik Açıklıklı Radar (SAR) görüntüleri kullanan görsel ve otomatik analizler, doğal olarak oluşan benek gürültüsünden dolayı zordur. Bu nedenle, ayrıntıları korurken benek gürültüsünü azaltmak SAR görüntü analizi için önemli bir araştırma alanıdır. Benek gürültüsünün azaltılması sırasında, homojen bölgelerin düzeltilmesi gerekirken kenarlar ve nokta saçıcılar korunmalıdır. SAR görüntülerinde baskın gürültü tipi, Gamma dağılımı ile çarpımsaldır, ancak SAR görüntüleri ayrıca genellikle ihmal edilen Gauss dağılımına sahip düşük miktarda toplamsal gürültü içerir. Bu tez çalışmasında, hem çarpımsal gürültü modelini hem de toplamsal gürültü modelini hesaba katan yeni bir seyrek odaklı benek gürültü azaltma yöntemi önerilmiştir. Önerilen benek gürültüsü azaltma yönteminde, toplam değişkenlik pürüzsüzlüğü terimine ek olarak, çoklayıcı ve ek veri terimleriyle birlikte değişken bir maliyet fonksiyonu kullanılmaktadır. Ayrıca, aynı anda çoklayıcı ve toplamsal gürültü ile ilgilenen önerilen değişimsel maliyet fonksiyonu için verimli ve kararlı bir sayısal en küçükleme yaklaşımı önerilmiştir. Önerilen yöntemin benek azaltma performansı, gerçek dünya SAR görüntüleri ve sentetik olarak üretilen SAR görüntüleri üzerinde gösterilmektedir.

Anahtar Kelimeler: sentetik açıklıklı radar, çarpımsal benek gürültü, Gamma dağılımı, toplamsal gürültü, Gauss dağılımı, toplam değişim.

ABSTRACT**MULTIPLICATIVE NOISE REDUCTION USING VARIATIONAL
METHODS**

AKSOY, Gülay

M.S., Department of Computer Engineering

Supervisor:

AUGUST 2019, 91 pages

Visual and automatic analyses using Synthetic Aperture Radar (SAR) images is challenging due to inherently formed speckle noise. Thus, reducing speckle noise in SAR images while preserving details is an important research area for SAR image analysis. During speckle reduction, edges and point scatterers should be preserved while homogeneous regions needs to be smoothed. Dominant noise type in SAR images is multiplicative with Gamma distribution but SAR images also contain low amount of additive noise with Gaussian distribution that is generally neglected. In this thesis, a novel sparsity-driven speckle reduction method is proposed that takes both multiplicative noise model and additive noise model into consideration. Proposed speckle reduction method employs a cost function with multiplicative and additive data terms in addition to total variation smoothness term. Also, an efficient and stable numerical minimization scheme is proposed for the proposed variational cost function which deals with multiplicative and additive noise simultaneously. Speckle reduction performance of the proposed method is shown on real-world SAR images and synthetically generated SAR images.

Keywords: synthetic aperture radar, multiplicative speckle noise, gamma distribution, additive noise, Gaussian distribution, total variation.

ACKNOWLEDGMENTS

I would like to express my deepest gratitude to my supervisor Dr. Fatih NAR for his uncomplaining support. I would especially like to thank him for sharing invaluable life experiences for helping me through the process. He has provided constant guidance and also helped me patiently correcting and supporting me whenever I needed help with various topics.

I owe thanks to a very special person, my precious husband Hüseyin AKSOY who never left me alone with her spiritual support, for his financial assistance and for his continued and unconditional love, support and understanding during my pursuit of this degree that made the completion of my thesis possible.

I appreciate my little daughter, Gülsüm AKSOY for the patience she showed during my thesis writing.



To my lovely family

YEMİN METNİ

I declare and honestly confirm that my study titled “Multiplicative Noise Reduction Using Variational Methods”, and presented as Master’s Thesis has been written without applying to any assistance inconsistent with scientific ethics and traditions and all sources I have benefited from are listed in bibliography and I have benefited from these sources by means of making references.

Gülay AKSOY



TEXT OF OATH

I declare and honestly confirm that my study titled “Multiplicative Noise Reduction Using Variational Methods”, and presented as Master’s Thesis has been written without applying to any assistance inconsistent with scientific ethics and traditions and all sources I have benefited from are listed in bibliography and I have benefited from these sources by means of making references.

Name, Surname : Gülay AKSOY

Signature :



TABLE OF CONTENTS

ÖZET	v
ABSTRACT	vi
ACKNOWLEDGMENTS	vii
TABLE OF CONTENTS	xi
LIST OF TABLES	xiv
LIST OF FIGURES	xv
LIST OF ABBREVIATIONS	xix
CHAPTERS	
1 INTRODUCTION	1
1.1 Synthetic Aperture Radar (SAR)	3
1.1.1 History of Synthetic Aperture Radar	5
1.1.2 SAR Platforms in Turkey	7
1.1.3 Usage Areas of SAR Imaging	8
1.1.4 Geometry of SAR system	10
1.1.5 Basics of SAR Imaging	12
2 LITERATURE SURVEY ON DESPECKLING	14
2.1 Speckle Noise	14
2.2 Speckle Reduction Methods	18
2.2.1 Common Methods	18

2.2.1.1	Mean Filter	19
2.2.1.2	Gaussian Filter (Gaussian Blur, Gaussian Smoothing)	19
2.2.1.3	Median Filter	19
2.2.2	Traditional Speckle Reduction Filters	20
2.2.2.1	Wiener Filter	21
2.2.2.2	Lee Filters	22
2.2.2.3	Frost Filters	23
2.2.2.4	Kuan Filters	24
2.2.2.5	Gamma Map Filter	24
2.2.3	State-of-the-art Speckle Reduction Methods	25
2.2.3.1	Non-Local (NL) Based Methods	25
2.2.3.2	Probabilistic Patch-Based (PPB) Filter	26
2.2.3.3	Block-Matching-3D and SAR-BM3D Filtering	27
2.2.3.4	Transform Domain Techniques	27
2.2.3.5	Wavelet Based Methods	28
2.2.3.6	Diffusion Based Methods	28
2.2.3.7	Sparsity-driven Methods	31
2.2.3.8	Variational Models Principle	32
2.2.4	Sparsity-Driven Methods	33
2.2.4.1	Rudin, Osher and Fatemi	33
2.2.4.2	Aubert and Aujol	34
2.2.4.3	Sparsity-Driven Despeckling	35
3	MULTIPLICATIVE ADDITIVE DESPECKLING (MAD)	38
3.1	Proposed Cost Function	38

3.2	Minimization of the Cost Function	39
3.3	Convexity analysis	44
3.4	Computational Complexity Analysis	45
4	EXPERIMENTAL ANALYSIS OF THE MULTIPLICATIVE ADDITIVE DESPECKLING METHOD	47
4.1	MAD Parameters Test on Synthetic Image	47
4.2	Comparison of MAD and AA Method	52
4.3	Comparison of MAD and Other Methods	54
4.4	Experimental Results on Real Dataset	57
4.5	Execution Time of MAD and Other Methods Despeckling	71
5	SUMMARY AND CONCLUSION	72
	BIBLIOGRAPHY	73
	APPENDICES	
A	REAL-WORLD SAR IMAGE DATASET	81
B	METRICS FOR QUANTIFYING SPECKLE NOISE	86
C	SPARSE MATRICES	88
D	EXPLICIT AND IMPLICIT METHODS	89

LIST OF TABLES

TABLES

Table 3.1	Computational complexity of the loop in MAD method	45
Table 3.2	Computational complexity of MAD	46
Table 4.1	Comparison MAD with AA	53
Table 4.2	Denosided Image Comparison MAD and Other Methods	55
Table A.1	Barcelona SAR Image Information	82
Table A.2	Toronto SAR Image Information	82
Table A.3	Singapore-2 SAR Image Information	82
Table A.4	Singapore SAR Image Information	83
Table A.5	Gulf of Mexico SAR Image Information	83
Table A.6	Germany SAR Image Information	83
Table A.7	North Sea SAR Image Information	84
Table A.8	Dessau SAR Image Information	84
Table A.9	Rügen SAR Image Information	84
Table A.10	Island Rügen SAR Image Information	85

LIST OF FIGURES

FIGURES

Figure 1.1	Relation between Real Aperture Radar (RAR) and Synthetic Aperture Radar (SAR) (Rarvssar, 2018)	4
Figure 1.2	Comparison of Radar and Optical image penetration of clouding (RadarOptical, 2018)	5
Figure 1.3	Aerial SAR image (on the right) taken in 1957 of a Volkswagen Beetle compared to an aerial photograph (picture on the left) illustrates the power of SAR applications from the earliest applications (OldSAR, 2018).	6
Figure 1.4	Comparison of Real SAR images , the pyramids of Giza, in 90s and 2000s. [(a) 20 m resolution, C-band, radar illumination from the left] [(b) 1 m resolution, X-band, radar illumination from the right (2007)](Moreira et al., 2013).	6
Figure 1.5	Current and Future SAR satellites (SARHistory, 2018)	7
Figure 1.6	Dalaman Mugla Turkiye (SARPER, 2018)	8
Figure 1.7	Haitian Supreme Court site. Red indicates >90 percent damage, yellow >75 percent Optical image © GeoEye2009. COSMO-SkyMed product © Agenzia Spaziale Itali-ana 2009-2010. All rights reserved	9
Figure 1.8	Oil spill observed off the Belgian coast near Zeebrugge on 08/10/2015 after a collision between two vessels (modified Copernicus Sentinel data [2015]) (OilSpil, 2018)	10
Figure 1.9	SAR Operation Geometry (Samuel et al., 2004)	11
Figure 1.10	Interpreting SAR Images	13

Figure 2.1	Affect of noise types in the same image and their image quality metrics	15
Figure 2.2	SAR image and the zoomed patch (Spain, Barcelona - ORI, SE (Sarimagesamplegallery, 2018))	16
Figure 2.3	Gamma Distribution	16
Figure 2.4	The implementation of different level speckle noise on a synthetic image. (a) Original image (b) Low Speckle (SNR:33.75 PSNR:36.70 SSIM:0.91) (c) Middle Speckle (SNR:14.76 PSNR:17.94 SSIM:0.40) (d) High Speckle (SNR:5.67 PSNR:9.00 SSIM:0.09)	17
Figure 2.5	Application of common filters to the original SAR image	20
Figure 2.6	Application of Wiener filter to the original SAR image	22
Figure 2.7	Application of Lee filters to the original SAR image	23
Figure 2.8	Application of Frost filters to the original SAR image	24
Figure 2.9	Application of Kuan filter to the original SAR image	25
Figure 2.10	Application of PPB filter to the original SAR image	26
Figure 2.11	Application of SAR-BM3D based filter to the original SAR image	27
Figure 2.12	Application of anisotropic diffusion filters to the original SAR image	29
Figure 2.13	Application of anisotropic diffusion filters to the original SAR image	29
Figure 2.14	Application of SRAD filter to the original SAR image	30
Figure 2.15	Effect of denoising for a real SAR image of Dictionary Learning Method	31
Figure 2.16	Application of AA based filter to the original SAR image	35
Figure 2.17	Application of SDD, SDD-QL and Fast SDD-QL based filters to the original SAR image	37

Figure 3.1	Absolute function and quadratic approximations of absolute function for different z values ($z = 0$ and $z = 1$)	40
Figure 3.2	MAD ($\alpha = 0.5$) ℓ_1 -norm approximations at 0.5 and 4.0	41
Figure 3.3	Difference between the original cost function in Equation 3.2 and the smoothly approximated cost function in Equation 3.15 ($\lambda_S = 1$).	45
Figure 3.4	MAD Execution Time with respect to Image Size $k = (n \times n)$	46
Figure 4.1	Synthetic Image (Aubert and Aujol, 2008)	47
Figure 4.2	Speckle reduction results of MAD method using different λ_s and ϵ ($\lambda_a = 1, \lambda_p = 0.5, \alpha = 0.3, n_{max} = 50$ and image size = 364×367)	48
Figure 4.3	Speckle reduction results of MAD method using different λ_s and λ_a ($\epsilon = 10^{-5}, \lambda_p = 1, \alpha = 0.3, n_{max} = 50$ and image size = 362×361)	49
Figure 4.4	MAD based image denoising using different images with same parameters (a) Original Lena image (b) Original Elif image (c) Noisy Lena image (d) Noisy Elif image (e) MAD denoised Lena image (f) MAD denoised Elif image	50
Figure 4.5	Synthetic Images used for Comparison MAD and AA	52
Figure 4.6	Synthetic Images used for Calculating Best Parameters of MAD and Other Methods on Different Speckle Levels	54
Figure 4.7	Despeckling results of synthetic Lena image using MAD and others	56
Figure 4.8	MAD and other methods despeckling results on Dessau image (see Table A.8 for image Details)	58
Figure 4.9	Despeckled part of Dessau Image (see Table A.8 for image Details)	59
Figure 4.10	MAD and other methods despeckling results on Barcelona image (see Table A.1 for image Details)	60
Figure 4.11	Despeckled part of Barcelona Image (see Table A.1 for image Details)	61

Figure 4.12	MAD and other methods despeckling results on Singapore image (see Table A.4 for image Details)	63
Figure 4.13	MAD and other methods despeckling results on Rügen image (see Table A.9 for image Details)	64
Figure 4.14	MAD and other methods despeckling results on island Rügen image (see Table A.10 for image Details)	65
Figure 4.15	MAD and other methods despeckling results on Germany image (see Table A.6 for image Details)	66
Figure 4.16	MAD and other methods descpeckling results on North Sea image (see Table A.7 for image Details)	67
Figure 4.17	MAD and other methods despeckling results on Gulf of Mexico image (see Table A.5 for image Details)	68
Figure 4.18	MAD and other methods despeckling results on Toronto image (see Table A.2 for image Details)	69
Figure 4.19	MAD and other methods despeckling results on Singapore-2 image (see Table A.3 for image Details)	70
Figure 4.20	Execution times of MAD and other methods	71
Figure B.1	Noise/SNR: a) low/high, b) mild/average, c) high/low	86
Figure D.1	Explicit method versus implicit method $\Delta t = 1.0$	90
Figure D.2	Explicit method versus implicit method $\Delta t = 1.5$	91
Figure D.3	Comparison of the Forward Euler method and the Forward- Backward Euler method $timestep = 0.05$ and $timestep = 0.025$ (Im- plicit, 2019)	91

LIST OF ABBREVIATIONS

<u>Symbols</u>	<u>Explanation</u>
λ_s	Smoothing level
λ_a	Additive noise data fidelity term
λ_p	Slow-step regularization (SSR) term
ϵ	Small positive constant
μ	Mean
σ	Standard deviation
f	Despeckled image
g	Image with speckle noise
∇	The gradient operator

Abbreviations

AA	Aubert and Aujol
AD	Anisotropic Diffusion
BM3D	Block-Matching 3
BV	Bounded Variation
CN	Condition Number
DL	Dictionary Learning
E-Lee	Enhanced Lee
EM	Electromagnetic
Eqs.	Equation
ICP	Incomplete Cholesky Preconditioner
LP	Low-pass
MAP	Maximum a Posteriori Estimation
MAD	Multiplicative Additive Despeckling
MMSE	Minimum Mean Square Error

MSE	Mean Square Error
NL	Non-Local
NLM	Non-Local Means
ODE	Ordinary Differential Equation
PCG	Preconditioned Conjugate Gradient
PDE	Partial Differential Equation
PDF	Probability Density Function
PMAD	Perona and Malik Anisotropic Diffusion
PPB	Probability Patch-Based
PSNR	Peak Signal-to-Noise Ratio
RADAR	Radio Detection and Ranging
RMS	Root Mean Square
ROC	Receiver Operating Characteristic
ROF	Rudin, Osher, and Fatemi
SAR	Synthetic Aperture Radar
SAR-BM3D	Synthetic Aperture Radar The Block-Matching 3-D
SDD	Sparsity Driven Despeckling
SNR	Signal-to-Noise Ratio
SSR	Slow-Step Regularization
SRAD	Speckle Reducing Anisotropic Diffusion
SSIM	Structural Similarity Index
TV	Total Variation
WT	Wavelet Transform

CHAPTER 1

INTRODUCTION

One of the most important features of life on our planet is its incredible diversity and constant change in this diversity due to natural forces and human kind. Many areas such as oceans, lands, forests, natural resources, urban areas and military areas are constantly changing. Due to the increase in the world population, these changes have more affected in lives of people. However, this effect is of critical importance which should be constantly monitored if the population growth of billions of people is taken into consideration. Both naturally destructive disasters, such as a tsunami, earthquakes, wildfire and human mobility on natural sources such as mines, oceans, and plants are sources of the such changes. Evaluation of these changes is of great importance of our future, but monitoring the changes we have mentioned inherently contains many challenges. For example, oil spilt into the ocean can spread to an area that finds miles. Many remote sensing methods and systems have been developed to overcome such challenges by allowing us to observe the earth surface. Among various remote sensing systems, optical systems and radars are the most important ones.

The range, which is also called look direction is the pulses of active microwave electromagnetic energy that is illuminated slices of terrain at right angles orthogonal to the travel direction of an imaging platform (i.e. aircraft or satellite). Radars have a wide range of uses due to the different capabilities they offer. In general, objects with a perpendicular angle to direction provide more reflection than smaller ones. As a result, depending on the look direction, the same place may appear in different levels of gray in some pictures.

Radar systems with Real Aperture Radar (RAR) (RAR, 2018) and Synthetic Aperture Radar (SAR) (Moreira et al., 2013) are open radars that use the flight path of a moving platform such as an airplane. While RAR systems require huge antennas for observing a scene, SAR systems use much smaller antennas that can be realized in practice while observing the same scene. Thus, SAR systems provide higher image resolution than RAR systems so they are usable as a radar imaging sensors in real life. Therefore, SAR systems are used in wider application areas compared to RAR systems since the resolution constraints on conventional radar systems are significant and indeed their physical production is not plausible. SAR has been developed to reduce the limitations of the conventional radar system to reasonable levels of physical reality. In SAR systems, advanced signal processing methods and platform motion can be used together to create artificial antenna sizes that cannot be realized in practice. In SAR imaging, the reflections of the shocks transmitted are recorded for a certain period of time. To increase the range resolution of these radars, it is necessary to shorten the pulse duration. However, the shortening of the pulse duration reduces the signal-to-noise ratio (SNR). While SAR sensors on aircraft platforms have a resolution to 10 centimeters, SAR sensors of satellite platforms can provide a resolution up to 30 centimeters.

Although initially proposed to military purposes, today observing the Earth using SAR has a wide range of practical military and civil applications in the oceans and land. In aerial surveillance applications, SAR sensors provide significant gains in all kinds of weather conditions and with their ability to operate without interruption. We cannot observe most of the spots or natural resources beneath the ground in the world because of climate conditions such as cloudy or rainy or less than daylight. Therefore, SAR is suitable for tropical countries. SAR overcomes this problem and ensures that visible parts of the earth's surface appear in high resolution. Unlike optic sensors, SAR also provides phase information that allows various new methods that are not possible or very challenging in optic sensors. For example, Interferometric SAR is such an application area based on SAR sensors that use phase information. Wave interference is the basis of the term interferometry, where interference comprises two waves (sound, light, ocean, electromagnetic, and seismic). Thus, it has become a technology with an increasing demand for various remote sensing applications.

Comparing SAR and optical remote sensing, SAR has more advantages such as getting data in all weather conditions. However, SAR images are degraded by the presence of a granular noise fused on actual SAR signal called speckle which is a variation of pixels in reflectivity (intensity) (Goodman, 1976; Lee et al., 1994; Argenti et al., 2013). The source of speckle noise, which is in a granular form, is the signal and limitations of the resolution cell itself that are inherent in SAR imaging systems. The performances of applications for SAR images of information extraction may diminish according to the amount of speckle noise. Also, SAR image does not have a constant average radiometric level in especially in homogeneous areas because of speckle noise (Lopes and Bruniquel, 1976). Increasing importance of SAR imaging systems increases the need for higher quality SAR images. Image quality should be as high as possible in order to process it quickly and reliably, either visually or automatically. Therefore, it must reduce the negative effects on the fine details in the images caused by speckle noise, especially for remote sensing applications. Speckle noise in SAR images is predominantly in a form of multiplicative noise and also in a small amount of additive noise. So speckle reduction, also known as despeckling, becomes complex and difficult, especially as noise levels get higher. Because of this need, researchers developed a considerable number of filters to reduce speckle noise over the last years. New generation of SAR satellite systems (SarSatellites, 2018) that are launched motivates more researchers to work on signal processing for this problem and existence of many publications in the literature support this situation (Argenti et al., 2013).

In this thesis, Multiplicative Additive Despeckling (MAD) method is proposed as an alternative method to the AA (Aubert and Aujol, 2008) filter which is superior to many filters, is developed that provides better speckle noise reduction with nice computational requirements. AA filter uses an explicit numerical solver (see Appendix D) which is not stable while MAD method uses an implicit solver which is unconditionally stable and also fast. The proposed method prevents the deterioration of the edges and point scatterers in the SAR image, while softening homogeneous regions. Thus, a better noise reduction is provided. Speckle noise reduction performance and we have experimented execution time with synthetically created images and real-world SAR images where proposed method is compared with well-known despeckling methods.

In the first chapter, history and geometry of SAR, advantages and disadvantages of

SAR, and the importance of SAR in our country and in the world are described in detail. In the second chapter, despeckling methods in the literature are examined in detail. Sample denoising results, advantageous and disadvantageous features of these methods are given. The base methods, so called variational approaches, that lead the MAD are explained. In the third chapter MAD method is explained in detail. Also, the convexity analysis and computational complexity analysis are given. In the fourth chapter, experimental studies of MAD method and other methods on synthetic and real-world SAR images are given. MAD method is compared with other methods' execution time quantitatively and despeckling quality by visually and quantitatively. In the fifth and last chapter, the importance of the MAD method, the literature contribution and general evaluations are given as conclusions.

1.1 Synthetic Aperture Radar (SAR)

Remote sensing is a technique of measuring, recording and examining the properties of objects from air and space by parts of the electromagnetic (EM) spectrum between X-rays and sound waves. In remote sensing, there is no contact with the object and there is no restriction on the distance angle. But, there must be a sensor to link to the target. These sensors can be divided into two categories: (a) passive systems and (b) active systems. In active remote sensing systems, the radiation is created by the system itself, so they are light independent. But in the passive systems, the sensor energy is created by external radiation source and illuminated target, so it is light dependent (i.e. created by sun). The diffusion of radar energy unlike sun light gives better information about surface features compared to optical sensors. Radar (Lewis, 1998; Munson and Visentin, 1989) and LiDAR are examples of active systems.

Remote sensing radar systems are divided into Real Aperture Radar (RAR) and Synthetic Aperture Radar (SAR) according to antenna positions (Franceschetti and Lanari, 1999). In the RAR systems, a narrow energy beam is directed to the flight direction of the carrier platform perpendicularly. The energy pulse is transmitted through the radar antenna, and the reflected signals are collected and processed to form the image of a narrow strip. The platform path is a straight line where this path is called the azimuth flight direction. In the RAR systems, while parallel to the flight direction, the pulse duration in the azimuth direction is shortened to increase the resolution. However, shortening the pulse duration reduces the signal-to-noise ratio (SNR) (see Appendix B). In order to achieve the desired resolution in RAR systems, required antenna sizes are not plausible in practice. The RAR system is generally preferred in applications where resolution is not critical. In order to get high-resolution images, a very long antenna must be transported by the platform which is not plausible. To eliminate large antenna needs, SAR uses the small antenna that acts as a large antenna, using the advantage of the motion of the platform (Moreira et al., 2013). So, SAR has been developed as a method of eliminating the constraints of the Real Aperture Radar system. In the SAR approach, the radar carried by a satellite or an aircraft is moving in the forward direction at a constant speed as much as possible. The radar sends a certain number of pulses for a certain period during the forward movement. The reflections of the pulses sent by the radar are also collected by the radar. The placement of the receivers at different angles and angles to the plane of the antenna ensures that all the waves reflected from the target are collected correctly and the objects in the complex structure can

be evaluated. The collected signals are recorded and combined appropriately which creates a synthetic aperture. The physical size of the synthetic aperture is determined by the speed of the platform and the total impact sending time. Each point in the SAR method can be observed in a long time. The relation between RAR and SAR is given in Figure 1.1.

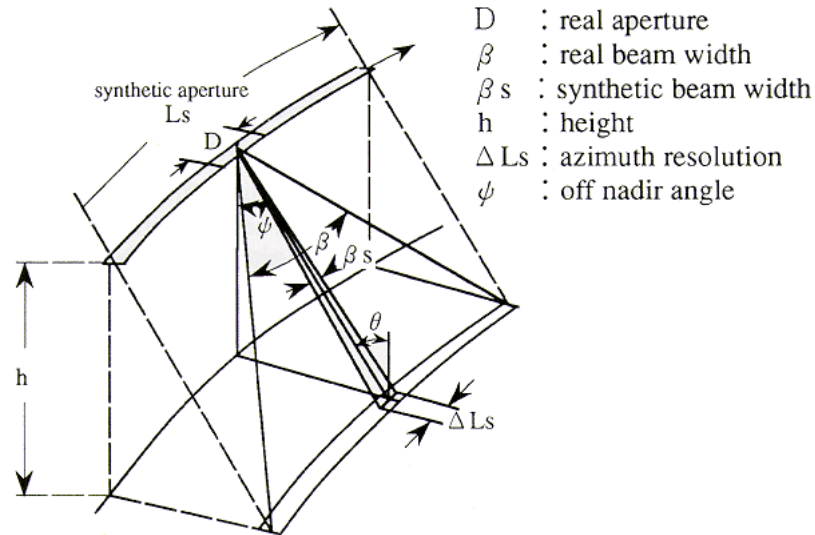


Figure 1.1: Relation between Real Aperture Radar (RAR) and Synthetic Aperture Radar (SAR) (Rarvssar, 2018)

To understand SAR, comparing it with more commonly used sensors like optical ones that can be a photo or video camera is a good choice. Optical sensors use electromagnetic waves using different parts of the electromagnetic spectrum to visualize images as SAR. The visible light spectrum is used by optical sensors, so captured images are nearly the same as what we see. SAR is developed by using a small antenna that works like it is much larger by electronically to imitate a very long antenna. SAR sensors use the advantage of signals that have a longer wavelength to form imagery that is two or three-dimensional images of objects in a gray level form. Optical sensors provide imagery that is similar to what we see, but SAR is in advantage compared to optical sensors because of overcome the problems of illumination source, wavelength, and resolution than optical sensors simply cannot.

Figure 1.2 shows that optical images are useful when the conditions are optimum but SAR is always optimum of itself in all conditions. For example, when there is no light (i.e. from sun) or there are clouds optical images does not provide desired information of Earth's surface.

SAR doesn't need a source of illumination because it has its own illumination. Therefore, it is able to create images day and night independent from environmental illumination. The distance that SAR transmits and receives wavelengths is longer than optical sensors. This allows SAR to penetrate dust, fog, smoke, clouds, moderate rainfall, sunlight illumination or other atmospheric obstructions and to penetrate into the agricultural soil of the ground surface. Thus, SAR has the capability to create images in almost all weather conditions. Because of these developments,

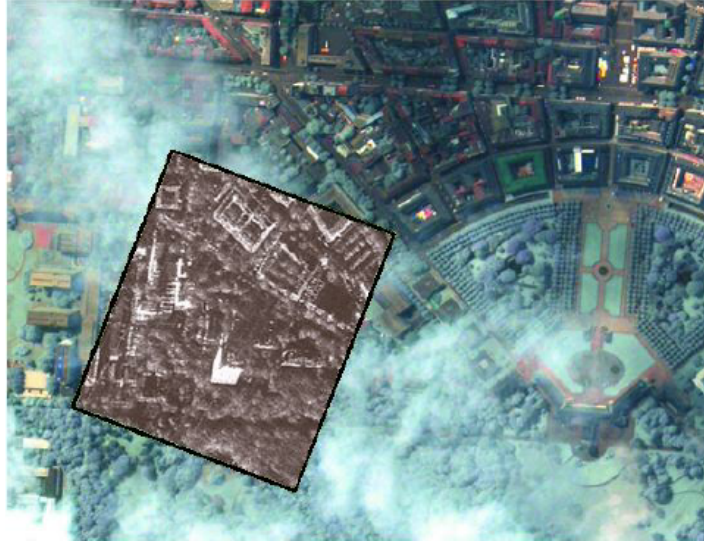


Figure 1.2: Comparison of Radar and Optical image penetration of clouding (RadarOptical, 2018)

SAR imaging enables various application areas and attracts more researchers in the remote sensing community.

1.1.1 History of Synthetic Aperture Radar

Carl A. Wiley working at Goodyear Aircraft as a mathematician in 1951 invented SAR during research about ICBM guidance systems (Wiley, 1985). In 1953, the University of Illinois and University of Michigan (UM) researchers independently developed SAR (WikipediaSAR, 2018). First successful focused airborne SAR image shown as in Figure 1.3 (FirstSAR, 2018) that illustrates the power of SAR applications from the earliest applications is produced by UM in 1957.

The quality and resolution of images weren't efficient in that years, so SAR studies are canceled for a time. In 1957 the amount of aimed resolution was 50 foot but nowadays even sub-millimeter resolution is obtained. Figure 1.3 shows the evolution of the SAR image clearly.

With the development of technologies, airborne systems has gained momentum for civilian applications after the 1970s. Geo / bio-physical variables of the surface of the earth have been observed more easily since air control is easier than ground control and less affected by many factors. In this regard, SAR has always been one step ahead of technological advancements, and then pioneered space-based missions. It is clear to visualize the evolution of SAR from Figure 1.4 (on the right), created similar resolution that corresponds the best of 90s (picture on the right) and a SAR image created with the newest of high-resolution SAR (picture on the left). SAR development is boosted by various factors, such as the launch of Seasat as the first civilian SAR satellite mission in 1978 and various advancements in technology. The need for SAR technologies of countries and the development of new technologies such as digital beam-forming, bi-static and multi-static, MIMO, large reflector antennas

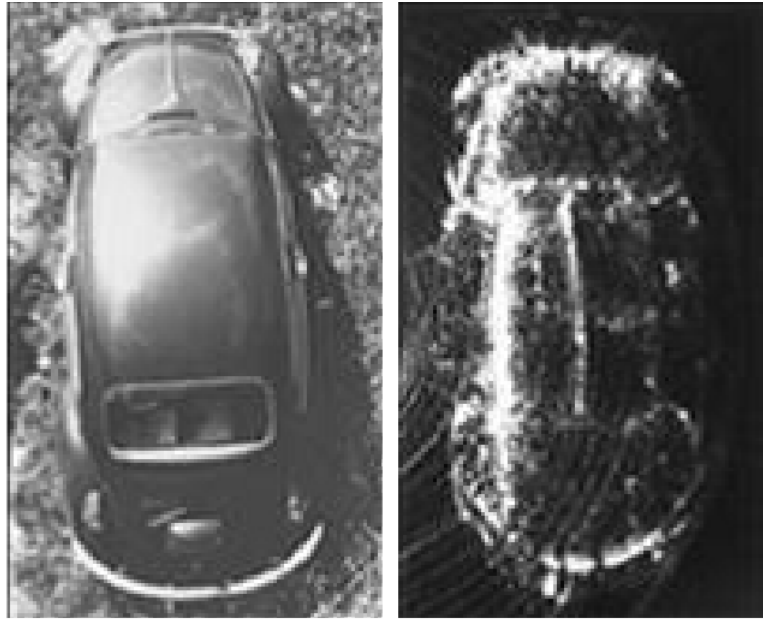


Figure 1.3: Aerial SAR image (on the right) taken in 1957 of a Volkswagen Beetle compared to an aerial photograph (picture on the left) illustrates the power of SAR applications from the earliest applications (OldSAR, 2018).

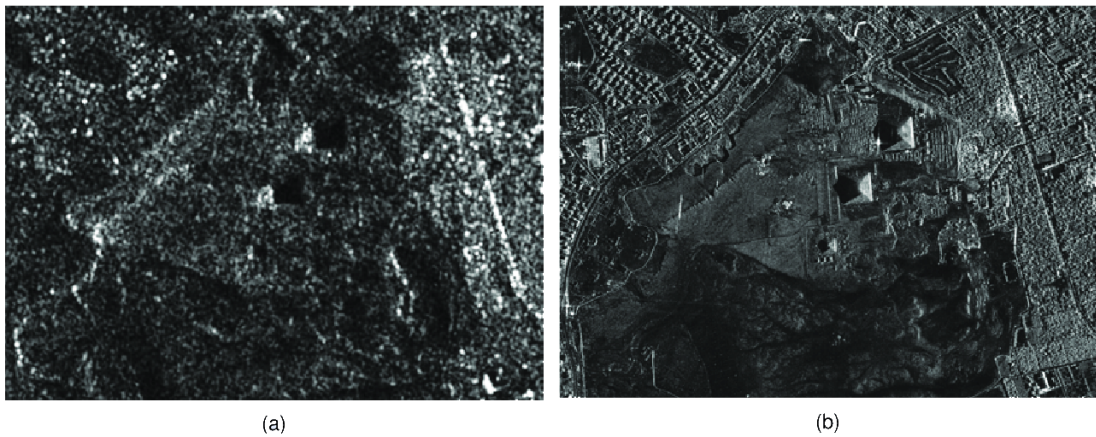


Figure 1.4: Comparison of Real SAR images , the pyramids of Giza, in 90s and 2000s. [(a) 20 m resolution, C-band, radar illumination from the left] [(b) 1 m resolution, X-band, radar illumination from the right (2007)](Moreira et al., 2013).

that allow improved SAR systems makes the countries research on this technology. The SAR image quality increases day by day, as shown in Figure 1.5 and naturally a lot of countries are working on SAR imaging. A recent technical specification compilation of current and near future SAR Satellites are explained in (Erbay, 2014; Argenti et al., 2013) and Figure 1.5 shows past, present, and planned SAR satellite missions.

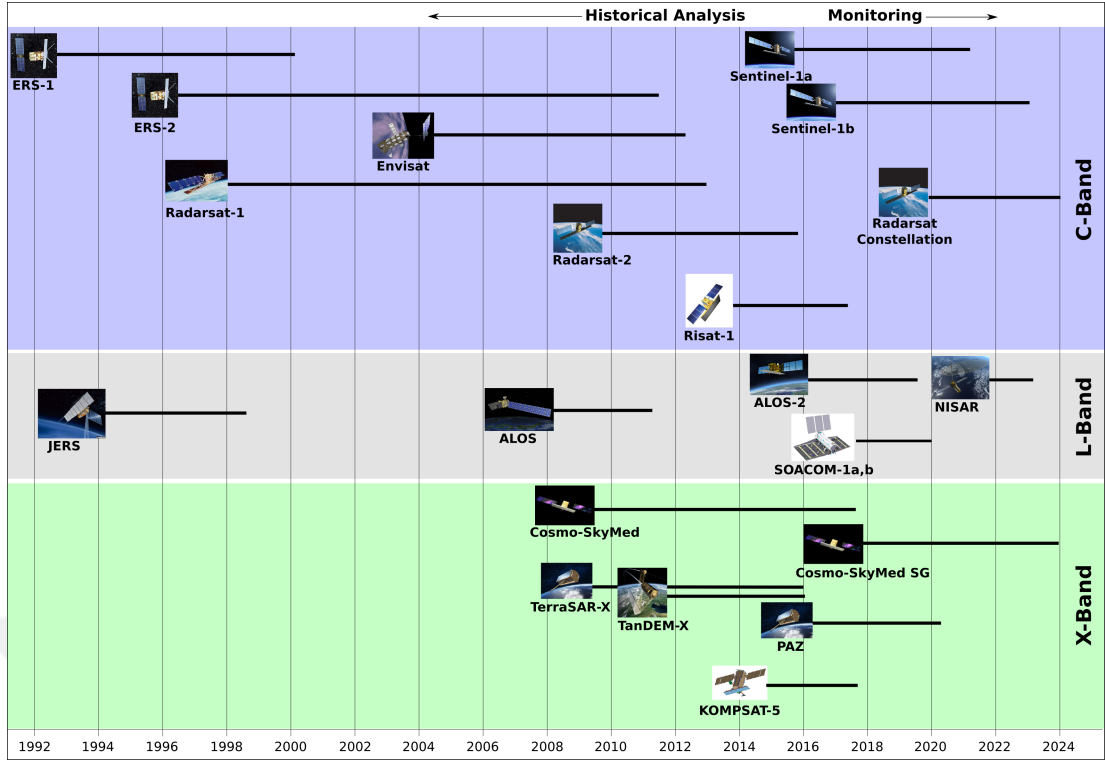


Figure 1.5: Current and Future SAR satellites (SARHistory, 2018)

1.1.2 SAR Platforms in Turkey

Developments in the world regarding SAR made it possible to concentrate on SAR in our country. National high resolution SAR sensor called SARPER (SARPER, 2018) developed by Aselsan in cooperation with Space and Defense Technologies (SDT). The SARPER sensor was integrated into an unmanned aerial vehicle ANKA and the flight acceptance tests were successfully completed in October 2016. A sample SAR image from SARPER sensor is shown in Figure 1.6.

SARPER is the first local, national and original SAR system to be integrated into the aerial platforms that targets ground observation with a high range and wide coverage for a day and night on land and sea for harsh weather conditions. It has been developed by two companies, Space and Defence Technologies (SDT) and ASELSAN. Reconnaissance and surveillance capabilities gained through applications such as Stripmap, Spotlight, GMTI, ISAR, Marine Search, Automatic Target Recognition, Phase-Compliant Change Detection and Pedestrian Detection (SARPER, 2018). m-SAR is another Turkish SAR system (mSAR, 2018) that is currently in development.

Launch of Göktürk-3 satellite until 2020 (Gokturk, 2018) is planned by Turkish government to obtain more benefit from SAR technology. The Göktürk-3 SAR satellite will be able to work independently from air conditions and at the low altitude orbit. It will be the first national SAR satellite program to meet the exploration and surveillance needs of Turkish Armed Forces. Other governmental institutions will also use SAR images gained from Göktürk-3 SAR satellite.



(a) Optical image from Google Earth

(b) SARPER image

Figure 1.6: Dalaman Mugla Turkiye (SARPER, 2018)

1.1.3 Usage Areas of SAR Imaging

SAR systems provide several advantages over optical systems. Although electro-optical imaging systems can achieve higher resolution and true color images, weather conditions and image acquisition time have a huge impact on their usage. Infrared systems are capable of night viewing, but they have a dependency on weather conditions, as other electro-optic systems also do (Spaceborne, 2018). Since SAR systems have its own microwave illuminator because of electromagnetic energy emitted by them, they are able to display with no daylight and create images almost in all weather conditions. Its microwave operating frequencies are chosen so that the radar imaging is unaffected by the change of weather or light (Crockett, 2013).

When SAR is compared to the optical sensors, it has some advantages which makes it best for taking topographical data like determining the contours of the earth. SAR can operate not only on the surface of the earth but also under the earth's surface (up to a certain degree) and its different reflections get valuable information. SAR can detect moving objects, which is also quite useful, especially in reconnaissance applications. Observing the Earth, oceans and the land, using the SAR sensors introduces various practical applications (Özdemir, 2012)

- Agriculture: SAR is mainly used for plant classification and monitoring in large areas, quantifying soil moisture, and biomass estimation. The crop producing model may be used to simulate the plant grow and predict crop yields.
- Geology: In geology, SAR is mainly used for prediction and quantification. It is used for obtaining accurate distance measurements (interferometry), measuring the dislocation extent at the source of an earthquake, and measuring small height variations because of the filling and dra-

ining of magma chambers under volcanoes. It is also used for assessing potential risk or hazards because of landslides, floods and subsidence, surface deformation, erosion in coastal regions, and measuring motions of a glacier (shown in Figure 1.7 (Brett and Guida, 2012)).

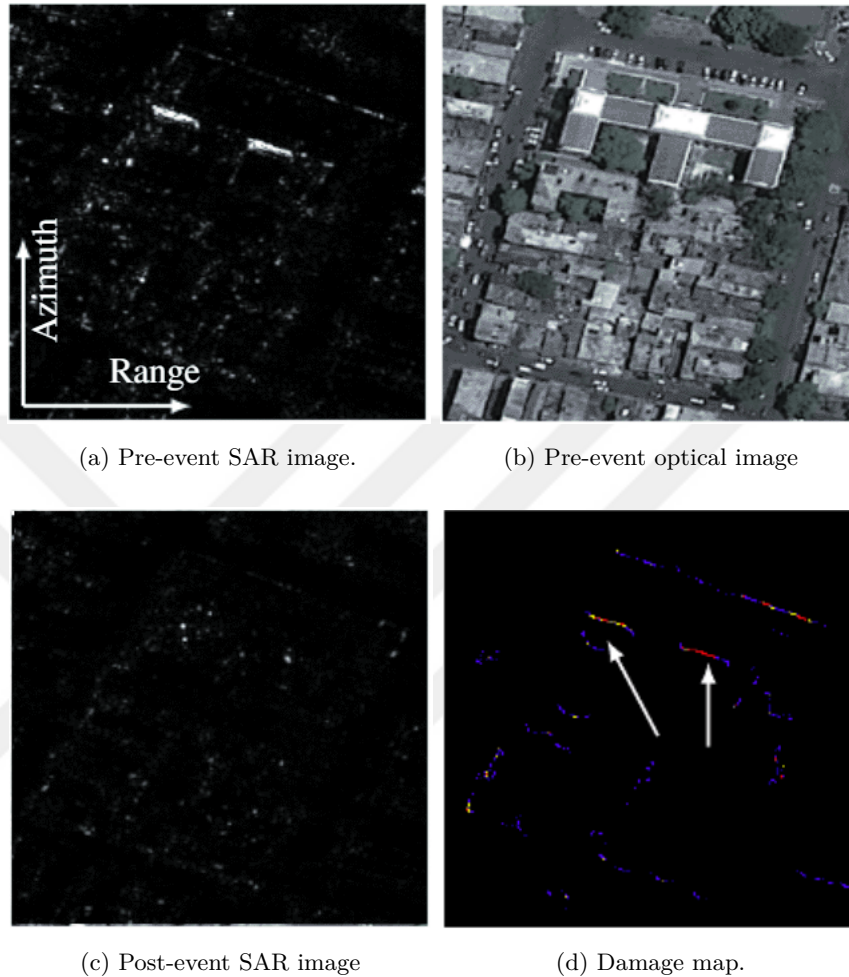


Figure 1.7: Haitian Supreme Court site. Red indicates >90 percent damage, yellow >75 percent Optical image © GeoEye2009. COSMO-SkyMed product © Agenzia Spaziale Itali-ana 2009-2010. All rights reserved

- Mining: Monitoring of subsidence because of extraction activities which includes coal mining
- Oceanography: SAR is used to analyze ocean surface capabilities, winds, wave spectrum, the thickness of ice in the sea, and different coastal activities.
- Mining: Monitoring of subsidence because of extraction activities, which includes coal mining
- Ecology: hazard monitoring, topographic classification to forest, climate monitoring for the detection of oil spills, environmental study such as

vegetation characterization, and in detection of squatters, landscape structure and organization.

- Hydrology: SAR is used to check snow water equivalence, estimating soil moisture, and surface water content that can be obtained before, during, and after the flood event; the flood area and effect can be mapped and the fluid movement can be delineated.
- Military: In Military, SAR is mainly used for surveillance, discovery, tactical evaluation, detecting stationary and moving targets, change detection, and target recognition.
- Archaeology: To take images of vintage buildings.
- Maritime surveillance: ice detection for ships that face the issue of ice in ports, and some seaways pass through freezing zones, ship detection and oil detection (shown in Figure 1.8).

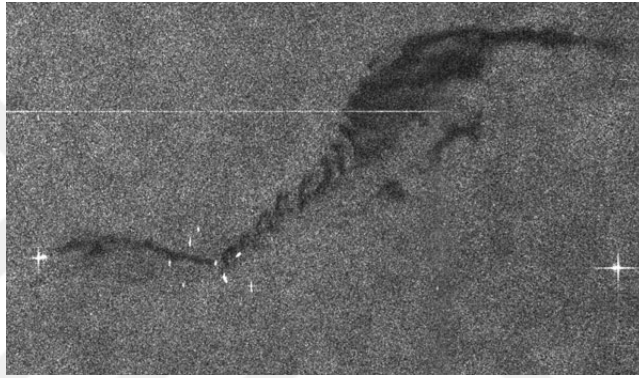


Figure 1.8: Oil spill observed off the Belgian coast near Zeebrugge on 08/10/2015 after a collision between two vessels (modified Copernicus Sentinel data [2015]) (OilSpil, 2018)

SAR imaging is likewise extensively used within the mapping of unobserved planets because of its thick atmospheric properties. Growing of applications throughout a big variety of regions may even make contributions to the technological development of a good deal of aerospace SAR structures.

1.1.4 Geometry of SAR system

In a SAR signal processor, a specific set of processes is applied to raw signal (raw SAR data) acquired from sensors to construct a high quality SAR image. In a raw SAR data, the point targets are spread out in range since the real beam moves through the target point in the along-track dimension. Therefore, it is not considered as an image because of the long frequency coded pulse (Samuel et al., 2004). The Figure 1.9 shows SAR operation geometry where h is the altitude of aircraft, V is the velocity, L_{SA} is the length of synthetic aperture distance and R is the target range (Samuel et al., 2004).

The radar energy pulses are transmitted by a self-illuminated Radar to illuminate the target (L_{SA}) and then collected by the receiver of the radar in time ($t_2 - t_1$). In radar, the distance of the objects in the scene is determined by measuring the time difference between the transmitted pulse and the received reflected energy from the scene. The range of the reflecting target object from the SAR platform is called slant range (R) shown in the equation below as the illumination length of the azimuth antenna beam on the Earth surface.

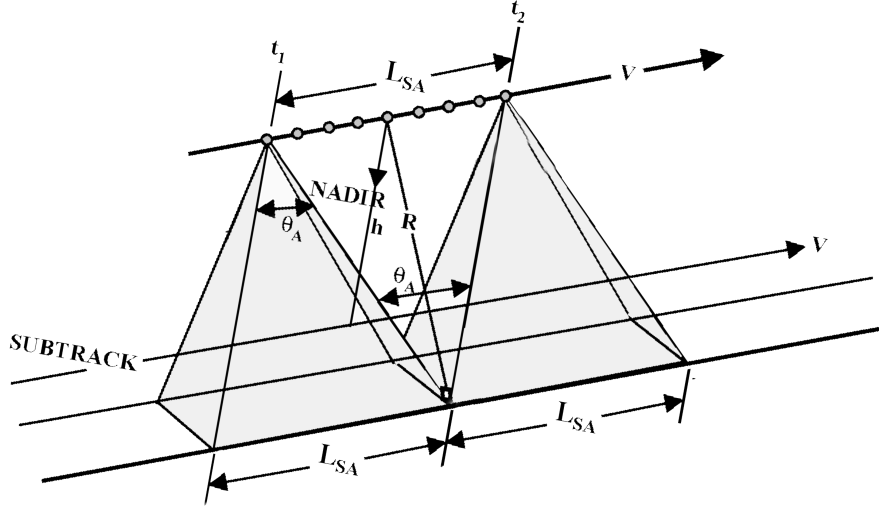


Figure 1.9: SAR Operation Geometry (Samuel et al., 2004)

Range resolution (σR), shown in Equation 1.1, is ability of a radar system to distinguish two objects separated by a minimum distance. The pulse bandwidth (b) and the speed of light (c) determines the σR .

$$\sigma R = \frac{c}{2b} \quad (1.1)$$

θ_A is shown in Figure 1.9 that is the angle of beam with respect to vertical real SAR antenna aperture azimuth beamwidth. The formula of θ_A is given in Equation 1.2 where λ is the wavelength and D_{AT} is the along-track antenna length that is earth target resolution element. The length of the emitted pulse determines the image resolution; shorter pulses result in higher resolution.

$$\theta_A = \frac{\lambda}{D_{AT}} \quad (1.2)$$

Synthetic aperture length L_{SA} shown in Equation 1.3 is a function of the beam-width of the real-aperture.

$$L_{SA} = \theta_A R = \frac{\lambda R}{D_{AT}} \quad (1.3)$$

Radars send a pulse of electromagnetic energy and receive back-scattered energy according to the reflection surface. Back-scattered energy is received by the platform

where it once again must pass through a horizontal or vertical filter. If pulse is sent horizontal and received horizontally, then its polarization is HH, or if receiving is only vertically, then its polarization is HV. If sending is vertically and receiving is only vertically, then it is called VV or receiving is horizontally then it is VH. These are single-polarization imaging modes. If HH and HV or VH and VV are combined they are called cross-polarized and if HH and VV are combined then they are called dual-polarized. If we combine all of them as (HH + HV + VH + VV) it is called quad-polarization.

Other terms about SAR operation geometry to define the properties of real SAR images are orbit and incidence angle. Orbit is the path of a satellite as it rotates around the Earth. The angle between the incident radar beam and the surface normal that radar beam intercepts is called an incidence angle. It represents the relationship between the radar beam and Earth surface slope, which is thought to be a complement of the depression angle. If the incidence angle increases, reflection decreases and back-scattering is low. This one of the most important parameters to determine the level of speckle noise, so the test images used in this thesis has different values of incidence angle (see Appendix A for details).

1.1.5 Basics of SAR Imaging

A SAR image is a quantitative representation of brightness, color and intensity values encoded, namely reflectivity. It differs substantially from an optical image. A SAR image is a rectangular domain in R^2 and array of pixels formed as different grey levels where a pixel is related in a small part of Earth's surface and the related surface size depends on the SAR features as altitude and synthetic aperture distance.

In reality, a map of apparent radar back-scattering values coded as different grey levels (called as reflectivity in radar community or intensity in image processing community), which not only depends on the target reflectivity at microwave wavelengths, but also depends on the viewing geometry (Lee and Pottier, 2009; Richards, 2009). Different surface features such as urban areas, forest, calm water, or rough sea exhibit different scattering characteristics and the brightness level of each pixel of the related image is created by the power of the reflected signal, namely reflectivity. (Ferretti et al., 2007).

A general SAR image consists of grey levels of pixels depends on the back-scattering as shown in the Figure 1.10. If back-scattering is very strong as seen at the right bottom of Figure 1.10, the related pixels are bright. As seen in the Figure 1.10, urban areas contain bright pixels due to strong reflectivity of corners of the buildings or other man-made structures with high reflectivity. If back-scattering is very low as in calm water then angle of reflection and angle of incidence becomes equal as seen at the left top of the enlarged part of image in Figure 1.10, the related pixels are black. Other back-scattering levels determines the grey level of pixels.

Each pixel reflectivity in a SAR image is created as a result of the criteria below:

- Smooth surfaces such as calm water zones is shown as black pixels as a result of low back-scattering.
- Surface changes that are closer to the wavelength of the radar cause strong back-scattering so they appear brighter in the SAR image.

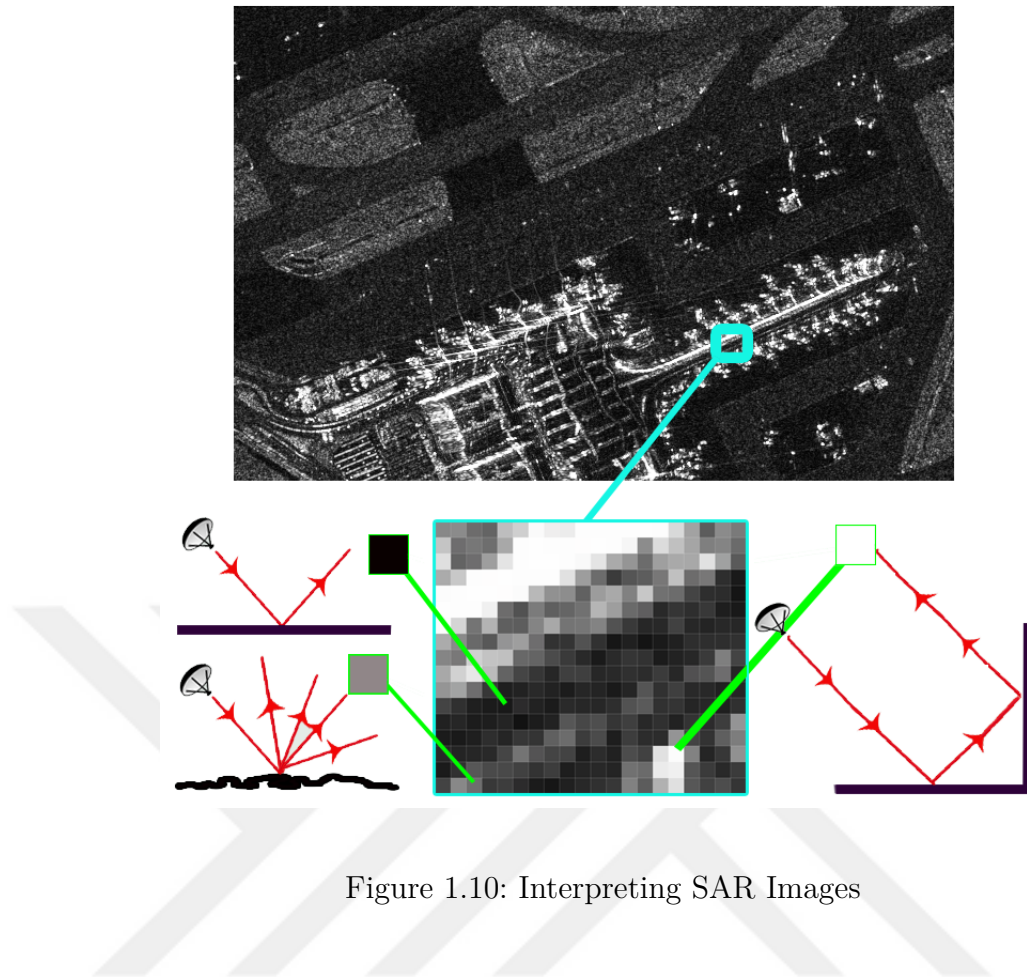


Figure 1.10: Interpreting SAR Images

- When a rough surface is wet, it is shown in lighter pixel value, but wind blown rough water can be brightly mixed back when the back-scattering is close to the wavelength of the radar.
- Peaks such as a mountain top and other surface variations in large-scale is shown brightly on the side facing the sensor and darker on the side facing away from the sensor.
- A strong response from the corner reflector may appear to be a bright cross with a rendered SAR image.
- Man-made objects such as buildings and bridges act as corner reflectors in a SAR image and appear as bright spots in the constructed SAR image.

CHAPTER 2

LITERATURE SURVEY ON DESPECKLING

2.1 Speckle Noise

Images contain noise that is an unwanted signal because of the sensor attributes of cameras, the circuitry of a scanner, weather conditions or sunlight illumination etc. Noise causes degradation in image components such as quality of color (Farooque and Rohankar, 2013; Stroebel and Zakia, 1995). Noise can not be eliminated completely, for example changes of the image signal can occur because of memory cell failure is inescapable because of raw signal transmission by electronically from one place to another

In Equation 2.1 general form of additive Gaussian noise is given.

$$g = f + n_{additive} \quad (2.1)$$

where g is the noisy observation, f is the noise free image, n is the noise (Farooque and Rohankar, 2013).

There are various noise types. Before designing a sensor system, determining the type of noise is necessary to get better results. Noise type can be inferred using test images. If such test images cannot be generated, a commonly used alternative is to trim a relatively large homogeneous region of an image and to analyze its histogram.

If sharp and sudden disturbances cause degradation to pixels over the image by the colors of black or white or both of them, it is called salt and pepper noise (Gonzalez and Woods, 2002). The main reasons of this type of noise are a memory cell problem, sensor failure, synchronization problems in converting images into image digital form, or transmission issues. The terms impulse, shot, random, independent or spike noise are also used for this type of noise (Mythili and Kavitha, 2011). Randomly black, white or both black and white dots exit in the image as a result of this type of noise (Boncelet, 2009) .

If the noise is caused by undesired random ripples in the signal because of poor illumination and or high temperature or electronic circuit transmission, it is Gaussian noise (Barbu, 2013). It is visualized as in a form of random values added to an image. Gaussian noise has a probability density function (PDF) of the normal distribution.

If noise has a granular form due to diffuse scattering's result, it is called as speckle noise (Lee et al., 2009) which is difficult to remove. In Figure 2.1 effect of different type of noises are shown. As seen in Figure 2.1, speckle noise causes too much changes in the original image compared to other noise types (see Figure 2.1.d). Thus, image quality metrics of a speckle noise reduced image is generally low (see Appendix B) as it is a difficult type of noise to remove.

Although, SAR imaging is useful that allows obtaining images even in wide variety of

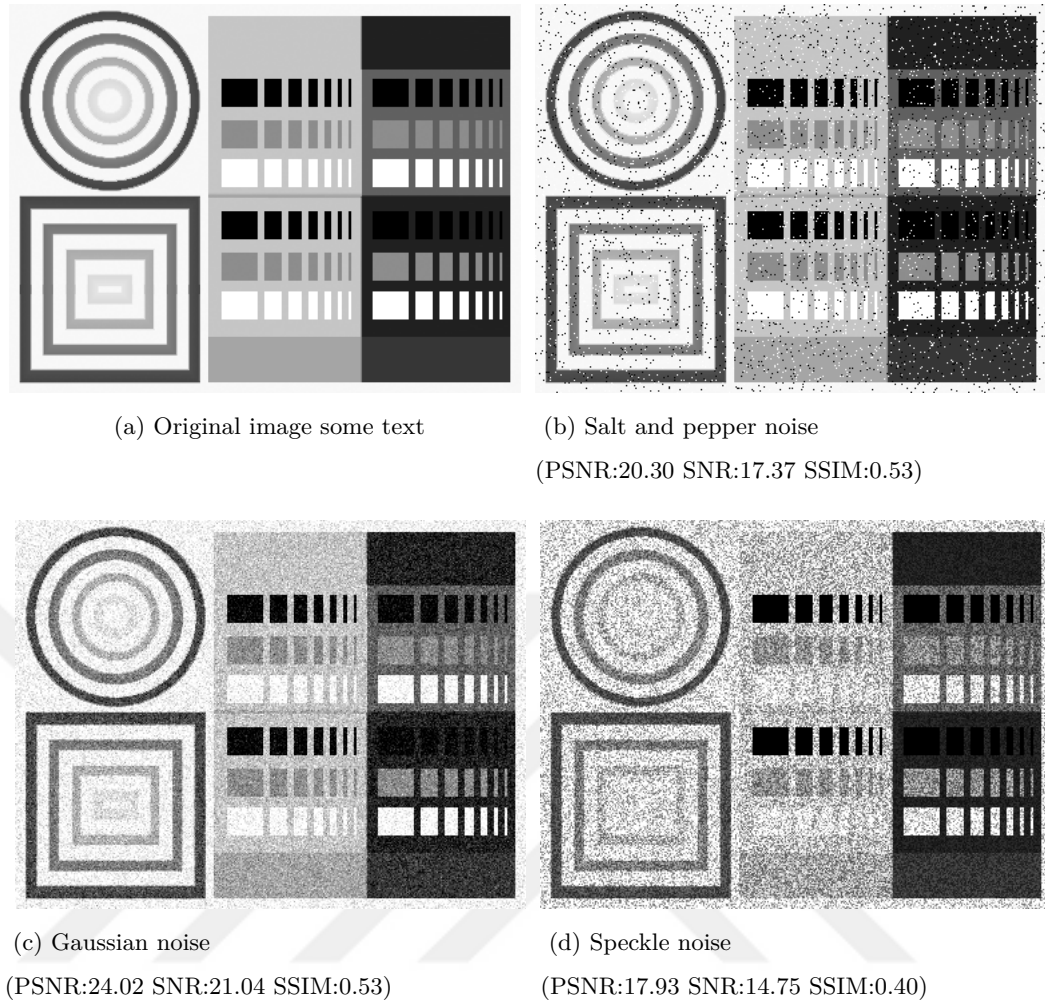


Figure 2.1: Affect of noise types in the same image and their image quality metrics

weather conditions (Kuttiyannan et al., 2008), SAR images contain high amount of speckle noise. A considerable amount of studies have been published in the literature to define SAR noise type and recover image from it. The speckle noise model is most appropriate and accurate noise model for SAR imaging that has been proven so far (Huang et al., 1996). The human eye has difficulties to perceive the speckle in most of the SAR images as shown in Figure 2.2.a. But, a computer program that will analyze a SAR image can easily perceive the speckles shown as in Figure 2.2.b.

Speckle is a signal dependent noise as resembling of small grains or particles inherent in SAR imaging systems since moisture and surface roughness increase radar reflection (Argenti et al., 2013). The energy returned from the flat surfaces to the radar receiver will be very low and will appear in the dark color of the radar image and as the surface roughness increases, the return energy will increase. Speckle noise is formed due to the unexpected random assumption of the signal from this multiple scatters in an image cell and has the characteristics of multiplicative noise (Richards, 2009). This noise inherently exists due to imaging physics that causes a reduction in the SAR image quality and makes them difficult to decode and interpret the fine detail properties of images (Moreira et al., 2013; Zhuang et al., 2013; Argenti et al., 2013). As principles of a generating SAR image is illustrated in Figure 1.10, a

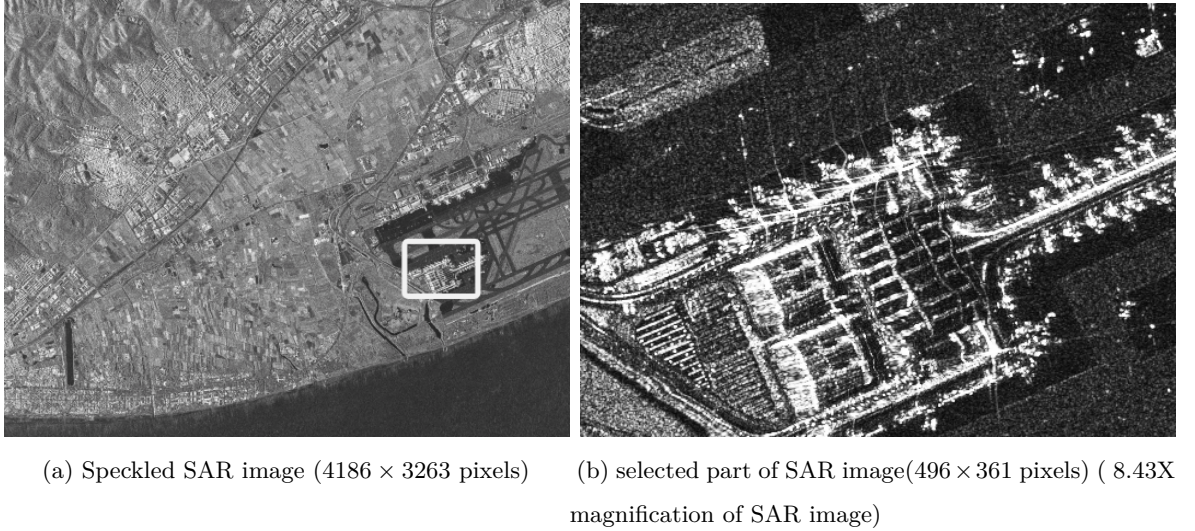


Figure 2.2: SAR image and the zoomed patch (Spain, Barcelona - ORI, SE (Sariimagesamplegallery, 2018))

natural and inescapable speckle noise is created. Speckle noise follows gamma distribution (Bioucas-dias and Figueiredo, 2010) which is shown in Figure 2.3. It can be caused by the physical structure of the system, by the properties of the imaging device, or due to environmental factors. Here, statistical independence of the signal and the noise is assumed. The presence of this noise degrades the advantages of SAR imaging, both by weakening the ability to detect targets on earth and by making it difficult to recognize spatial patterns.

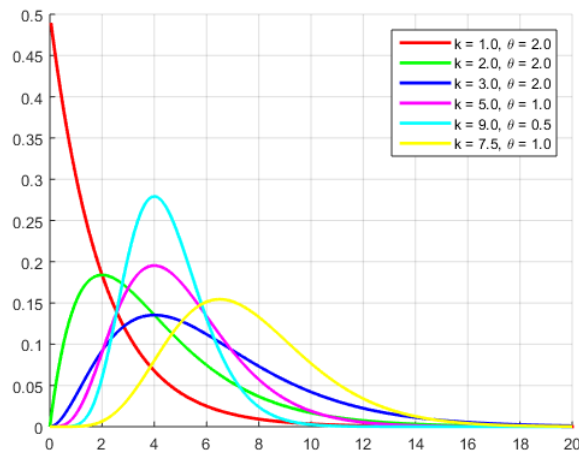


Figure 2.3: Gamma Distribution

Equation 2.2 shows that the following function is a pdf for any $k > 0$. In Equation 2.2, g is reflectivity values, f has a pdf of Gamma distribution with shape parameter k . The θ^k of a single pixel and sample mean are equal to the local area

variance and local area mean. In any part of the image, speckle noise is directly proportion to the g .

$$f(g; k, \theta) = \frac{g^{k-1} e^{-\frac{g}{\theta}}}{\theta^k \Gamma(k)} \quad \text{for } g > 0 \text{ and } k, \theta > 0. \quad (2.2)$$

Speckle noise in SAR images include both additive noise and multiplicative noise where multiplicative one is more dominant than additive one. Various SAR despeckling methods considers speckle patterns as multiplicative noise while ignoring additive noise. But in this thesis, we pay attention to both of them. The general form of speckle noise in SAR images is given as Equation 2.3:

$$g = f n_{\text{multiplicative}} + n_{\text{additive}} \quad (2.3)$$

where g is the noisy observation, f is the noise-free image, $n_{\text{multiplicative}}$ is the multiplicative noise due to coherent interference, and n_{additive} is the additive noise (sensor noise, etc.). (Farooque and Rohankar, 2013)

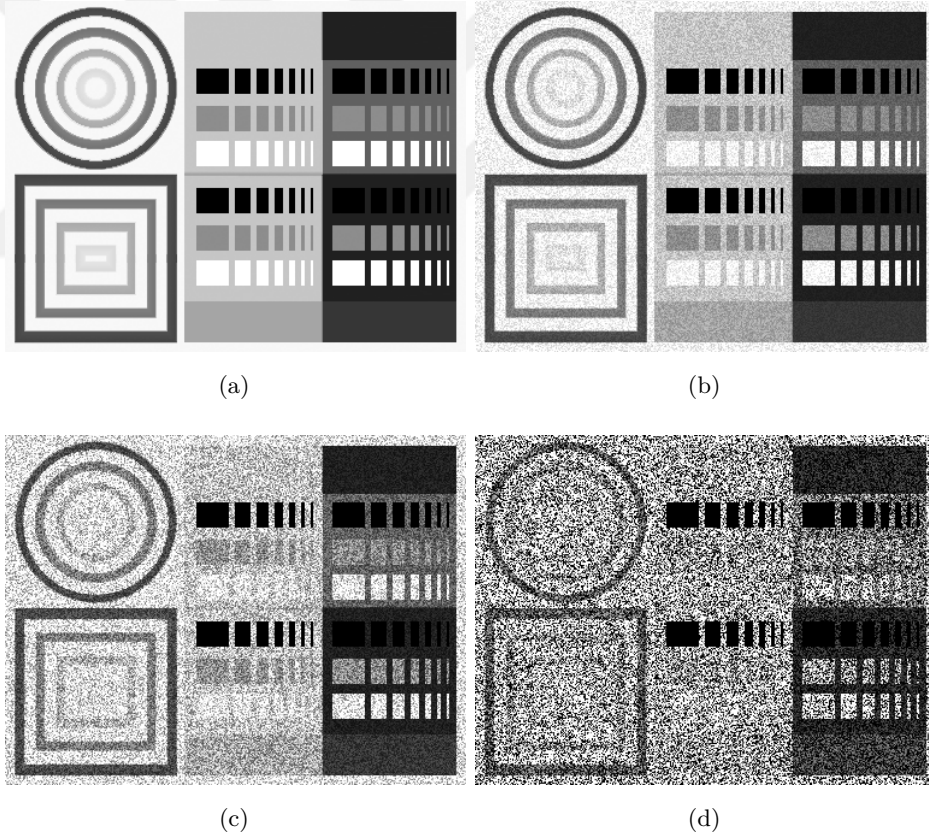


Figure 2.4: The implementation of different level speckle noise on a synthetic image. (a) Original image (b) Low Speckle (SNR:33.75 PSNR:36.70 SSIM:0.91) (c) Middle Speckle (SNR:14.76 PSNR:17.94 SSIM:0.40) (d) High Speckle (SNR:5.67 PSNR:9.00 SSIM:0.09)

Speckle noise level is important for despeckling performance and there exist a considerable amount of work that are characterizing the speckle noise (Goodman, 1976), (Lee, 1985), (Lopes et al., 1990). The Figure 2.4 illustrates the application of different speckle noise levels onto a synthetic image. As shown in the Figure 2.4.d, increasing the amount of speckle degrades the image quality and detecting the shapes becomes more difficult. Thus, despeckling becomes a mandatory process to improve the quality of SAR images.

2.2 Speckle Reduction Methods

Speckle noise can be reduced by multi-look techniques or using speckle filtering (also known as speckle reduction or despeckling). Multi-look is a technique that combines multiple single look images that are obtained from the same location, sums, and then averages them to look count (Gagnon and Jouan, 1997). Multi-looking also increases pixel spacing, because you typically average a number of samples (e.g. 4 samples at 10 m spacing become 1 sample at 20 m). Therefore, multi-look approaches cause imaging resolution to become lower, which is not desired. So multi-looking is not necessarily needed (Gagnon and Jouan, 1997).

The main purpose of the despeckling methods are imperative to get rid of unwanted signals, or at least to decrease the amount of speckle noise without damaging the original content of the image. The ideal despeckling method should smooth homogeneous regions while preserving image details such as edges, point scatterers, and textures. During speckle reduction, artifacts shouldn't be added in resulting image (Liu et al., 2008). Because of this principle, many of despeckling methods have been developed over the years to reduce the speckle level of images captured by SAR systems. Therefore, there is a growing interest in developing high-performance noise reduction methods. In this thesis, speckle reduction methods are grouped into three main categories; (1) common methods, (2) traditional speckle reduction methods, and (3) state-of-the-art speckle reduction methods.

2.2.1 Common Methods

Mean, Median, Gaussian, Geometric, Gamma MAP, Local Sigma and Bayes-Gauss filters (Gonzalez and Woods, 2002; Lopes et al., 1990; Sarkka, 2013; Crimmins, 1985; Barbu, 2013) are common methods. The main purpose of these filters is to reduce noise as much as possible while enhancing the quality of the image by maintaining the point scatterers and edges. However, these noise reduction methods do not reduce speckle noise and consequently do not meet the requirements of applications such as texture analysis, classification and target detection (Shi and Fung, 1994). Some studies comparing the performance of these filters in speckle noise reduction are also reported in the literature (Mansourpour et al., 2006; Wicaksono et al., 2016; Kupidura, 2016). These methods generally are used to reduce salt and pepper noise. Most commonly used ones are listed below.

2.2.1.1 Mean Filter

One of the simplest filter is the Mean filter which uses a square window which replaces the centre value of the sliding window with the mean value of its neighbor pixel values together with itself. According to the given filter window, the Mean filter calculates the sum of all related pixel values and the sum of them is divided by the size of the filter window to eliminate the noise (Gonzalez and Woods, 2002). There are four types of mean filter that are arithmetic, geometric, harmonic, and contraharmonic mean filters (Gonzalez and Woods, 2002). The most used and also the simplest one is an arithmetic mean filter (Gonzalez and Woods, 2002).

$$\hat{f}(x, y) = \frac{1}{mn} \sum_{(s,t) \in S_{xy}} g(s, t) \quad (2.4)$$

In Equation 2.4 Mean filter formula is given where the area to be denoised is represented by S_{xy} , (x, y) is the center point of sub window that size is $m \times n$, $g(x, y)$ is the noisy image, f is the denoised image. This filter constructs the denoised image f , by computing the average pixel value for each pixel at (x, y) using the noisy neighbour pixels in region S_{xy} . Each pixel of image is filtered spatially in a window that surrounds those pixels by using the reflectivity values in a rectangular window (Boncelet, 2009). It can be easily implemented and used to remove simple noise types such as Gaussian noise and salt and pepper noise. It can not remove speckle noise mostly but reduces a small amount of it. While despeckling, it gives blurring effect on the images and as a result it degrades the details. This makes the method the least used for despeckling purpose.

2.2.1.2 Gaussian Filter (Gaussian Blur, Gaussian Smoothing)

The Gaussian filter blurs images to eliminate noise by using a 2D convolution operator that multiplies the pixels on the image by the core matrix. The main assumption is that the image values that the noise can take are in a form of Gaussian distributed. One of the reasons for using a Gaussian smoothing filter is to protect the spatial frequency components on the picture. A Gaussian function is used to blur the image and thus reduce noise. The filter can cope with statistical noise and uses the probability density function (PDF) (Barbu, 2013) that the formula is given in Equation 2.5.

$$P(x) = \frac{1}{\sigma\sqrt{2\pi}} e^{-\frac{(x-\mu)^2}{2\sigma^2}} \quad (2.5)$$

where x represents reflectivity, μ represents the mean of x , and σ represents the standard deviation of x . Square of the standard deviation (σ^2) is called as the variance of x .

2.2.1.3 Median Filter

One of the best known nonlinear filter is the median filter (Baxes, 1994; Haralick and Shapiro, 1992; Yin et al., 1996). It is used to remove unwanted, almost instantaneous noises from an image. Thus, median filter is used as a smoother in image processing

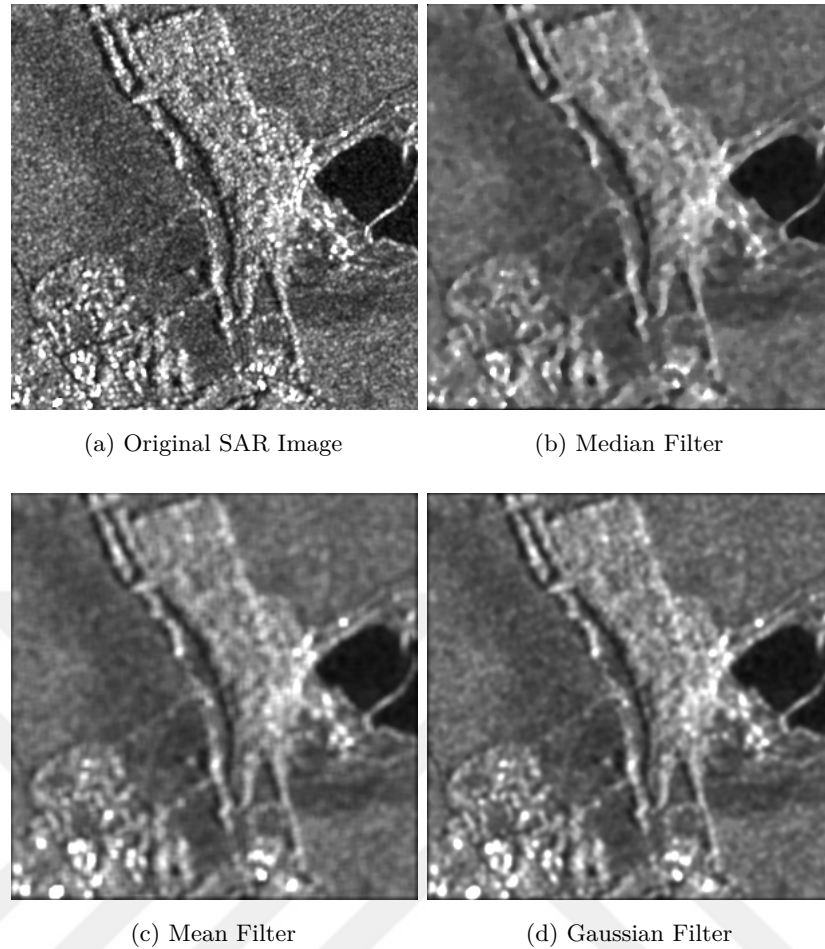


Figure 2.5: Application of common filters to the original SAR image

community and signal processing community. Under certain conditions, it reliably filters the noise while preserving edges. The median filter uses a $m \times n$ -size structure that can be called a window or box that has an odd number of entries. Its basic principle is to replace the gray level of each pixel by calculating the median of the pixel values in the given kernel neighborhood. Although it is easy to implement, it tends to remove image details when the speckle noise percentage is more than 0.4.

When the mean filter, median filter or Gaussian filter are applied to the speckled image, a big amount of speckle still exists. Increasing the smoothing level blurs the reflectivity of both the noisy and noiseless pixels and decreases high frequency details such as point scatterers. Figure 2.5 shows the application of common filters on an original SAR image.

2.2.2 Traditional Speckle Reduction Filters

An adaptive filter is a digital linear filter that has automatically controlled by self-adjusting characteristics by variable parameters and can detect system variation in time according to an optimization algorithm. The Lee (Lee et al., 1994), the

Kuan (Kuan et al., 1985), the Frost (Frost et al., 1982), the modified Lee, modified Frost filters (Lopes et al., 1990), Wiener Filter (Zhong and Cherkassky, 2000) are one of the best known adaptive filters. In 2008, the Improved Sigma filter (Lee et al., 2009) was proposed following the principles of Lee sigma filters to improve the performance of it. More recently, Maximum A Posteriori (MAP) probability (Lopes et al., 1990) based wavelet despeckling methods have been proposed.

These filters have been used mostly for speckle reduction and compared with a new generation despeckling methods they are assigned into the Traditional Speckle Reduction Filters group. These filters use a filtered signal that is obtained by the weighted average of the samples in a given window and calculate a new pixel value that is smoothed by passing mathematical operations over all pixels on the image. During this process, the despeckled pixel value is estimated by optimizing the smallest mean error frame (MMSE) criterion which minimizes the mean square error (MSE). These filters are adapted to the local texture information and filter the speckle. When the mandatory conditions are provided for each filter, they can smooth speckle patterns in homogeneous areas while details in heterogeneous areas are preserved. They perform equally well for low noise levels and slightly outperform for a higher level of speckle noise (Gagnon and Jouan, 1997). Each despeckling filter is designed based on different algorithms and parameters. These filters represent unique trade-offs between denoising, smoothing, computational complexity, and visual representation. Most commonly used traditional speckle reduction filters are listed below.

2.2.2.1 Wiener Filter

Wiener Filter estimates the original noisy image linearly based on a stochastic framework (Zhong and Cherkassky, 2000). Indeed, what Wiener filter is doing is the same as Least Mean Square filtering. The Wiener filter is a filtering method that provides optimal recovery if a signal is affected by additive white Gaussian noise. The Wiener filtering method is often used to successfully recreate the deformed images even if they are corrupted or blurred as despeckling in SAR interferometry.

This filter is based on the computation of local image variance if the variance is large, the image is smoothed in a lower amount and if it is small; the image is smoothed more. This filter is the most optimal solution according to the other methods, but it may produce bad results when the system is not stable.

It has the following mathematical formula in Equation 2.6 where, $H(g, v)$ is degradation function, $H(g, v)$ is conjugated complex, $G(g, v)$ is degraded image, $S_n(g, v)$ is power spectra of noise and $S_f(g, v)$ is power spectra of the original image.

$$f(g, v) = \left[\frac{H(g, v)^*}{H(g, v)^2 + \frac{S_n(g, v)}{S_f(g, v)}} \right] G(g, v) \quad (2.6)$$

This approach outperforms many linear filtering methods, but it requires more computation time (Huang et al., 1996). Wiener filter generally doesn't reduce speckle well because it assumes (a) additive noise, (b) stationary linearity, (c) known spectral characteristics, and (d) being physically realizable in a causal system (Bonclet, 2009)

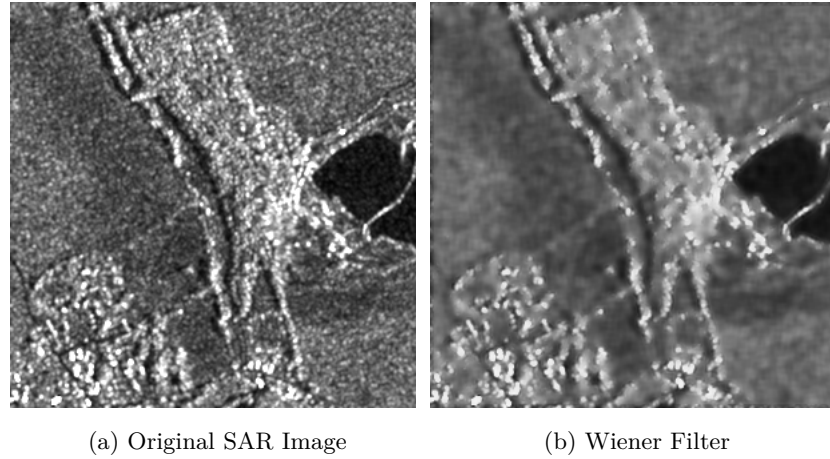


Figure 2.6: Application of Wiener filter to the original SAR image

2.2.2.2 Lee Filters

Lee filters are adaptive filters that use local statistics. In Lee Filters, the filtered signal is calculated by the weighted average of the pixels, in a related window kernel of the target pixel center. During this process, the noise-reduced pixel value is estimated by optimizing the MMSE criterion. Lee adapted the filter coefficients by using a moving window data but this causes a contrast between the quality of despeckling and the capability of keeping image details. Local statistics are used to differentiate between homogeneous regions and edges.

First Lee filter called Lee sigma filter (Lee, 1981; Lee, 1983; Lee, 1985) was developed in 1983 when computational resources are scarce. Homogeneous regions are determined based on the two-sigma probability where memory and computation resources are used efficiently. Lee filter is not a proper choice today since it has limited despeckling performance in general. Mathematical model of Lee filter is given in 2.7

$$\hat{F}(i, j) = G_m + W * (C_p - G_m) \quad (2.7)$$

where \hat{F} is the filtered pixel value, G_m is the mean reflectivity in the filter window, C_p is the center pixel, and W defines the filter window.

In order to overcome the disadvantages of the Lee filter and to provide a better performance, Enhanced Lee an improved sigma filter has been developed (Lee et al., 2009; Lopes et al., 1990). The Lee filter reduces speckle well in homogeneous parts of speckled image but has no alternatives on preserving edges or feature structures in related window because of averaging the pixel according to its neighbour pixels in a fixed square window. Enhanced Lee filter can not do this effectively but at least it performs better than Lee filter. It separates the image into three main parts as homogeneous, heterogeneous and isolated point targets then applies the developed formula specific to each part and obtains the result of filtering as shown in Equation 2.8. So, the Enhanced Lee filter performs well both in the homogeneous and

heterogeneous areas.

$$\hat{F} = \begin{cases} G_m & \text{for } V_i \leq V_g \\ R_f & \text{for } V_g < V_i < V_{max} \\ G_c & \text{for } V_i \leq V_{max} \end{cases} \quad (2.8)$$

Figure 2.7 shows the application of the Lee filters on an original SAR image.

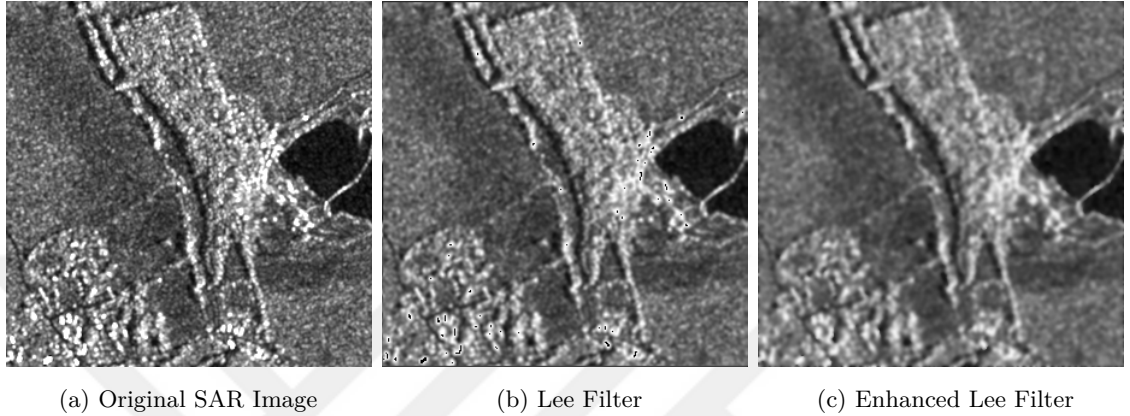


Figure 2.7: Application of Lee filters to the original SAR image

2.2.2.3 Frost Filters

Frost et al. (Frost et al., 1982) developed an adaptive despeckling method for SAR images with the multiplicative noise assumption. They stated that filtering methods developed for images that produced by optical methods are insufficient to reduce noise on SAR images because of image acquisition by SAR is different from an optical image acquisition. The method provided a smaller functional form of MSE for smoothing than many other methods at that time.

The pixel that will be despeckled is replaced with new a value based on the distance from the filter center by using a weighted average of the pixel reflectivity values in a given window kernel using the local variance to minimize the MSE. Frost uses the local statistics as an exponentially restrained roundly symmetric filter that makes it adaptive. Thus, it provides a minimum MSE while preserving the edges and point scatterers while smoothing the homogeneous areas.

The enhanced Frost filter uses a similar structure as the enhanced Lee filter (Lopes et al., 1990).

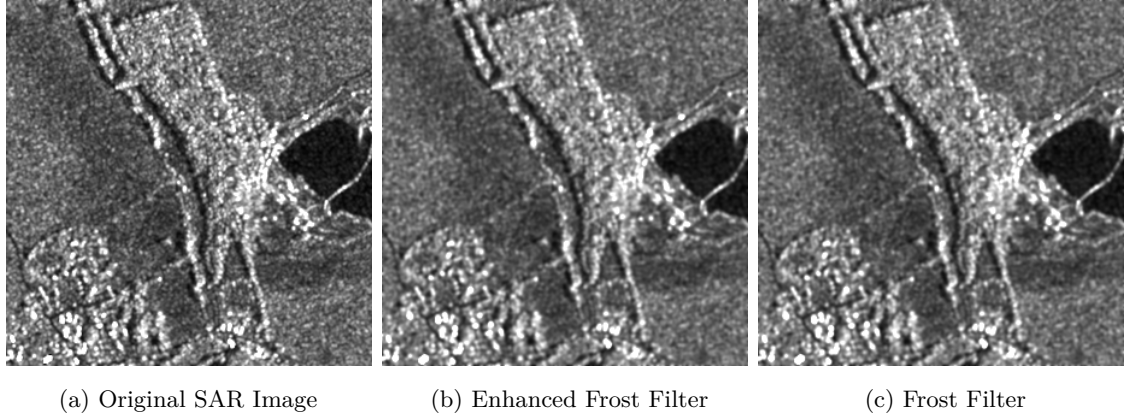


Figure 2.8: Application of Frost filters to the original SAR image

2.2.2.4 Kuan Filters

The Kuan is an adaptive noise filter (Kuan et al., 1985) that uses an MSE to calculate the true value of the center pixel of the square filter window by using local statistics. Kuan converts multiplicative speckle pattern into a signal-dependent additive noise and apply MMSE where local mean and local variation in the neighborhood ($m \times n$) of a pixel need to be estimated. It has similar algorithm to the Lee filter, but window weight changed slightly by simplifying the assumptions in the calculations by using a different weighting function. The filter obtains the signal by calculating from the local statics as mean and variance. It assumes speckle noise as Gaussian distributed where the noise standard deviation is assumed to be constant for all parts of the speckled image. Equation 2.9 shows the resulting reflectivity value \hat{f} for the smoothed pixel (Pranali A. Hatwar, 2014) where G_c is a central pixel of filter window, G_m is the mean intensity with filter window and J_{Kuan} is in Equation 2.10.

$$\hat{f} = G_c * J_{Kuan} + G_m * (1 - J_{Kuan}) \quad (2.9)$$

$$J_{Kuan}(f) = \frac{1 - \frac{(V_g)^2}{(V_i)^2(f)}}{1 - (V_g)^2} \quad (2.10)$$

The Enhanced Kuan filter separates the image into homogeneous, heterogeneous, and isolated point targets as Enhanced Lee filter did.

2.2.2.5 Gamma Map Filter

Being similar to the Kuan filter and proposed by Lopes (Lopes et al., 1990), the Gamma Map filter assumes that the speckle noise is Gamma distributed. It uses a Bayesian approach where it tries to maximize the a posteriori probability (MAP) $P(S/Z)$. Filters' equations are derived by solving the MAP equation.

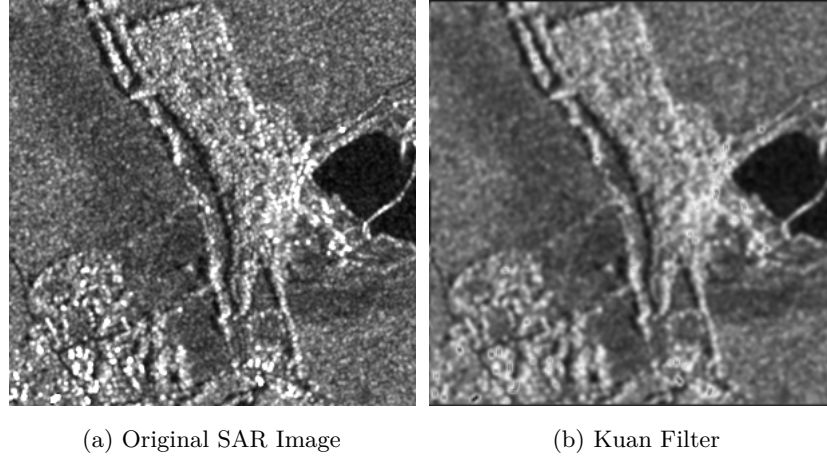


Figure 2.9: Application of Kuan filter to the original SAR image

The filter is assumed as a non-stationary multiplicative speckle noise model (Mascarenhas, 1997). However, use of tiny windows introduces a bias. Speckle reduction depends on the distributions used to describe the signal and $P(Z/S)$. The true filtered value of the center pixel of square filter window is created using the local statistics. Under certain conditions, it can reduce speckle better than minimizing the loss of texture than other traditional speckle reduction methods.

2.2.3 State-of-the-art Speckle Reduction Methods

Traditional despeckling methods have low resource requirements but they are not effective on despeckling (smoothing homogeneous regions while preserving edges, texture, and point scatters). To overcome these problems, state-of-the-art despeckling methods are developed. These methods are grouped as wavelet based, diffusion based, sparsity based (dictionary, variational), non-local means based, and others.

2.2.3.1 Non-Local (NL) Based Methods

Non-Local methods use self-similarities in the image that can be found as similar patches to reduce noise. To find similar patches, there must be a metric to measure their distance. To measure similarity of patches, different operators have been proposed (Tasdizen, 2009; Foi and Boracchi, 2016) but generally a weighted Euclidean distance shown as in Equation 2.11 where k is the weighting kernel, d is distance and g is the noisy image is used.

$$d = \|k[g(x_1, r_1, t_1) - g(x_2, r_2, t_2)]^2\| \quad (2.11)$$

After detecting related patches, they are properly merged for producing the despeckled image $\hat{f}(\cdot)$ that is created by summation of despeckled similar patches in

condition as $d < T_{fixed}$ (T_{fixed} is a fixed threshold) as shown in Equation 2.12

$$\hat{f}(\cdot) = \sum (g(\cdot)e^{-d}) \quad (2.12)$$

SAR images with multiplicative noise are very different from the natural images. In SAR images, the Euclidean distance as a classical similar measure under the assumption of Gaussian noise is not optimal anymore. Therefore, NL fails as similar patches can't be found. For high level of speckle noise similar patches may not be found (see in Figure 2.4.c Figure 2.4.d). If moderate level of speckle noise exists (Figure 2.4.b) then it acts as an effective despeckling filter. But SAR images generally contain a high level of speckle noise.

Non-Local Means(NLM) (Buades et al., 2005) and NLM based filter (Lu et al., 2010), Non-Local framework for SAR denoising (NL-SAR) (Deledalle et al., 2015), Block-matching 3-D algorithm (BM3D) (Dabov et al., 2007), The Probabilistic Patch Based (PPB) (Deledalle et al., 2009) and SAR-BM3D (Parrilli et al., 2012) are NL based filters. PPB and SAR-BM3D are most used NL methods in the literature.

2.2.3.2 Probabilistic Patch-Based (PPB) Filter

Probabilistic Patch-Based (PPB) (Deledalle et al., 2009) is a general patch-based spatial NL filter. It aims to select homogeneous pixels by self similarity and average the noise among homogeneous pixels. This filter performs well on images that contain both additive and multiplicative noise. The sample despeckling result is given below:

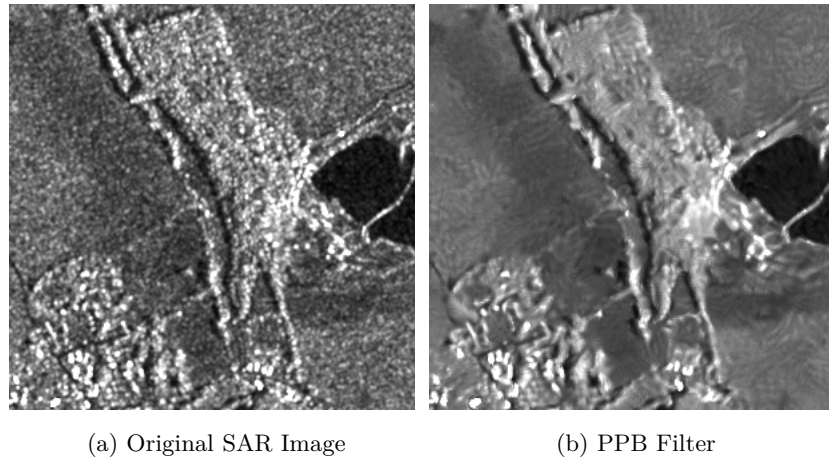


Figure 2.10: Application of PPB filter to the original SAR image

2.2.3.3 Block-Matching-3D and SAR-BM3D Filtering

The NL approach is based on the self-similarities that most images exhibit clearly where an image patches are repeated almost identically over. Differing from spatial filtering, Block-Matching-3D (BM3D) method is based on detecting these similarities and imitates a true statistical despeckling along such patches which uses more than a neighborhood of the pixel. The BM3D groups the most similar patches in an image based on a minimum Euclidean distance criteria. Then, these grouped patches despeckled and returned to their location with suitable weights in order to estimate the speckle free image.

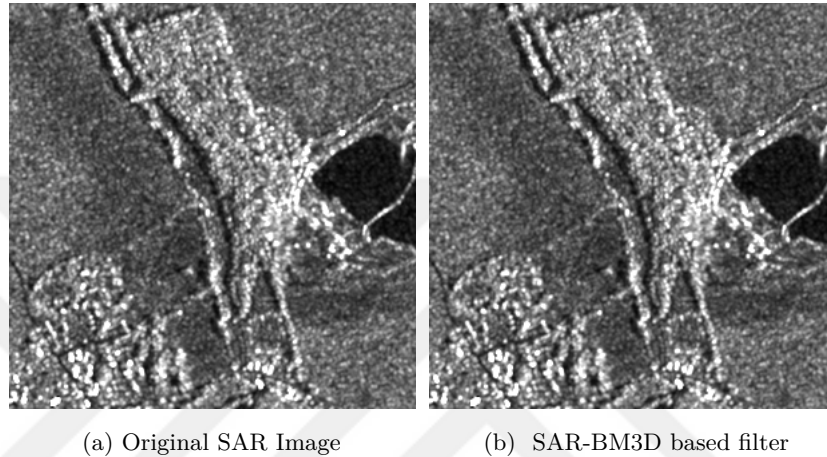


Figure 2.11: Application of SAR-BM3D based filter to the original SAR image

SAR-BM3D (Parrilli et al., 2012) algorithm is the adopted version of BM3D for SAR images. It uses same structure as BM3D but modifies its main steps based on SAR features. SAR-BM3D, merges NL and Wavelet Denoising Technique (WDT), modifies them to the statistical properties of the SAR. Probabilistic distribution of speckle is the reference to aggregate the similar patches, and these patches is merged with Wavelet Transform (WT) in a 3D domain. SAR-BM3D has better despeckling results to preserve relevant details while smoothing is applied in synthetic and low-resolution images. It is an effective despeckling filter for synthetic images but is slow and works for limited SNR values and performance decreases in high resolution real-world SAR images as seen in Figure 2.11 (see details in experiments chapter). A significant disadvantage of this method is its long execution times.

2.2.3.4 Transform Domain Techniques

In Transform Domain Techniques (TDT), a number of transform coefficients concentrate on the signal energy. The most used TDT in SAR despeckling are wavelet (Argenti and Alparone, 2002), contourlet (Do and Vetterli, 2005), curvelet (Li et al., 2011) shearlet (Hou et al., 2012). The difference between these methods is a creation of the transform domain from different shapes and directions. The most used one is Wavelet Based Methods in SAR despeckling.

2.2.3.5 Wavelet Based Methods

Various Wavelet transform (WT) based despeckling methods are proposed in (Parrilli et al., 2012; Argenti and Alparone, 2002; Foucher et al., 2001; Solbo and Eltoft, 2004; Argenti et al., 2006; Bianchi et al., 2008; Gao et al., 2008). WT converts multiplicative speckle noise into additive noise as shown in Equation 2.13. Then it removes the speckle noise in the wavelet domain. Wavelet analysis has a wavelet prototype function (Kent et al., 2004) called mother wavelet $\psi(\frac{t-\tau}{s})$ as shown in Equation 2.14. $\frac{1}{\sqrt{s}}$ is a normalized factor used to ensure energy across different scale remains the same, s is reflects of scale width, τ is the translation species its translated position in time axis.

$$z(s) = x(s)n(s) = x(s) + x(s)[n(s)-1] = x(s) + v(s) \quad (2.13)$$

$$\psi(\tau, s) = \frac{1}{\sqrt{s}}\psi\left(\frac{t-\tau}{s}\right) \quad (2.14)$$

Despeckling quality is determined by wavelet coefficients that is in a large magnitude for signal and image features. WT is more efficient than most of spatial despeckling filters by using noise models in the wavelet domain due to its useful properties such as time-frequency localization, multi-resolution, sparsity, and auto-correlation.

2.2.3.6 Diffusion Based Methods

Perona and Malik (Perona and Malik, 1987; Perona and Malik, 1988; Perona and Malik, 1990) developed Perona and Malik Anisotropic Diffusion (PMAD) to overcome the problems involved in traditional methods. In PMAD, different levels of filtering are applied along the edges of the image and in the direction of the curvature. Nonlinear diffusion method is utilized for avoiding the blurring and edge localization problems. Here, conduction coefficient is selected as a function of the pixel reflectivity that allows a diffusion process for simultaneous removal of noise and preservation of edges. Diffusion process is inhomogeneous which leads to a lower level of diffusion in the locations with a larger likelihood of being edges.

PMAD equation is given in Equation 2.15:

$$\begin{cases} \partial f_t(x, y)/\partial t = \text{div}[c_t(|\nabla f|) \cdot \nabla f_t(x, y)] \\ f_{t=0} = f_0 \end{cases} \quad (2.15)$$

where $|\nabla f|^2$ is the measure of likelihood, f_0 is noisy SAR image, div is divergence operator, $c(|\nabla|)$ is the diffusion function or coefficient where smoothing across the boundaries is inhibited, $\nabla f_t(x, y)$ is magnitude of image gradient where it has higher value at edges or boundaries due to discontinuity in pixel reflectivities. PMAD uses two diffusivity function variants as in Equation 2.16 where $\lambda > 0$ is an edge

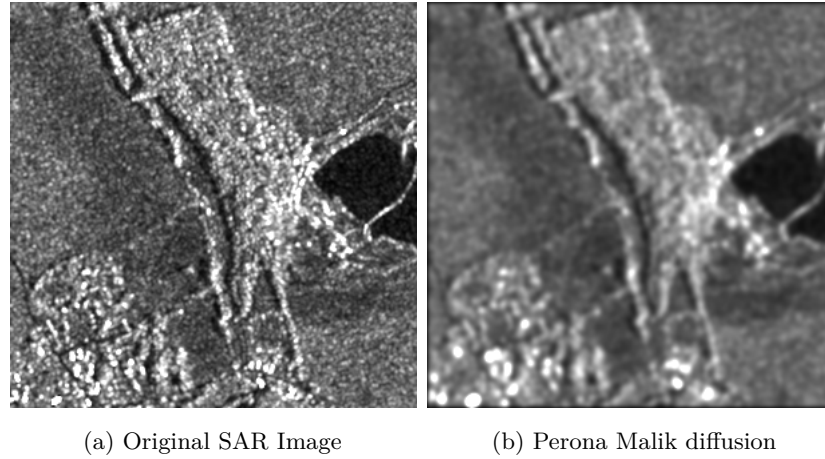


Figure 2.12: Application of anisotropic diffusion filters to the original SAR image

magnitude parameter that controls the diffusion process.

$$c(s^2) = \frac{1}{1 + \frac{s^2}{\lambda^2}} \quad (1) \quad (2.16)$$

$$c(s^2) = -e^{-\frac{s^2}{\lambda^2}} \quad (2)$$

Results of (li You et al., 1996) show that the PMAD is unstable with respect to initial image (i.e. perturbations in it) and also the energy functional leading to the Perona–Malik contains infinite number of global minimum.

Yu and Acton (Yu and Acton, 2002) applied the anisotropic diffusion method to the Lee filter and created a new model called Lee Diffusion and Frost Diffusion to show they can be cast as PDEs and and then edge-sensitive anisotropic diffusion is modelled leading to Speckle Reducing Anisotropic Diffusion (SRAD).

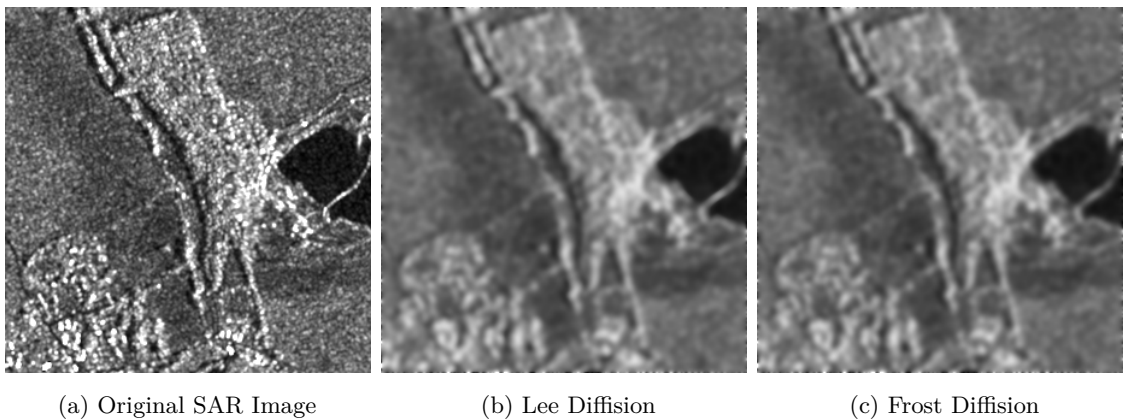
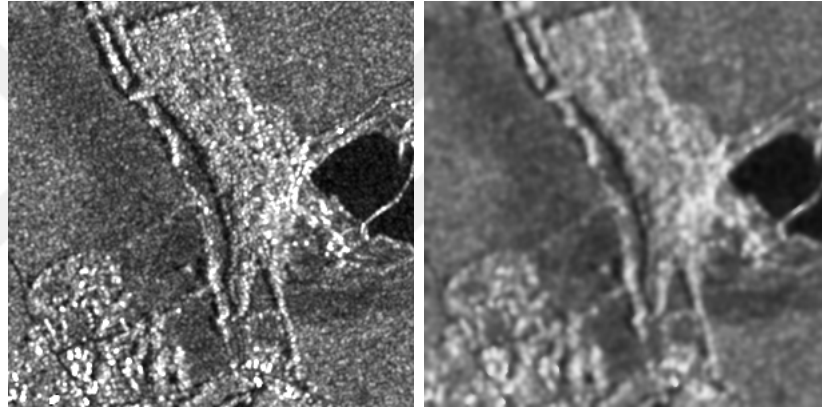


Figure 2.13: Application of anisotropic diffusion filters to the original SAR image

SRAD is a non-linear technique for multiplicative noise reduction and image enhancement using PDE. SRAD makes intra-region smoothing in homogeneous regions and preserves the edges. Its difference from PMAD is due to $c(q)$ that is the coefficient of variation. $c(q)$ achieves a balance between smoothing in homogeneous regions while preserving edges. It achieves this balance by using thresholds to alter the performance between average-like filtering in homogeneous regions and identity filtering at edges.

$$\begin{cases} \frac{\partial f_t(x,y)}{\partial t} = \text{div}[c_t(q)\nabla f_t(x,y)] \\ f_{t=0} = f_0 \end{cases} \quad (2.17)$$

SRAD can preserve edges and can even enhance them; but this highly depends on the precision of correct edge detection by the selection of correct threshold value; otherwise, the edges will not be enhanced and they can be even blurred. If edges detected as noise, they will be smoothed. SRAD is solved in an iterative way with larger number of iterations so it is computationally expensive.



(a) Original SAR Image

(b) SRAD Filter

Figure 2.14: Application of SRAD filter to the original SAR image

Dictionary Learning Based Methods

Dictionary Learning (DL) based despeckling concept tries to obtain a patches of dictionary (D) that provides the equivalent image contents in a different features (Ma et al., 1501). A patch (x) is simply a small part of the image and obtained overlapping image patches. The minimization problem of DL method is below that aims to get best dictionary D and a sparse vector y with coefficients for the linear combinations.

$$\min_{D,y} = \frac{1}{2}\|x - Dy\|_2^2 + \lambda\|y\|_0 \quad (2.18)$$

where the first term is a data fidelity term that aims to be small as possible. In order to obtain a small value for the data fidelity term, y has to be sparse such that we only use a few of the available atoms in the dictionary (Foucher, 2008). Each

image patch can be sparsely represented as a linear combination of particles taken from the obtained dictionary.

To use this method, high-quality image database and small patches of a noisy version of these high-quality images are used in training step, also known as dictionary construction step. Some researchers propose to learn the dictionary from examples instead of the deployment of a pre-determined set of basis functions. Thus, a dictionary with sparsity and redundancy characteristics is learned, as a set of parameters, which is a prior-learning approach. The idea of learning a dictionary using a set of training patches to reduce speckle noise has been studied in a sequence of works (Soganlui and Cetin, 2014; Routray et al., 2016; Deka and Bora, 2013; Elad and Aharon, 2006; Huang et al., 2012; Hao et al., 2012). Due to low statistical information in small patches, dictionary learning does not perform well for such small patches, so using it for patches of arbitrary size is a major problem. Another problem is the level of speckle that deforms patches, which causes DL to fail. So, DL works at a limited level of speckle noise.

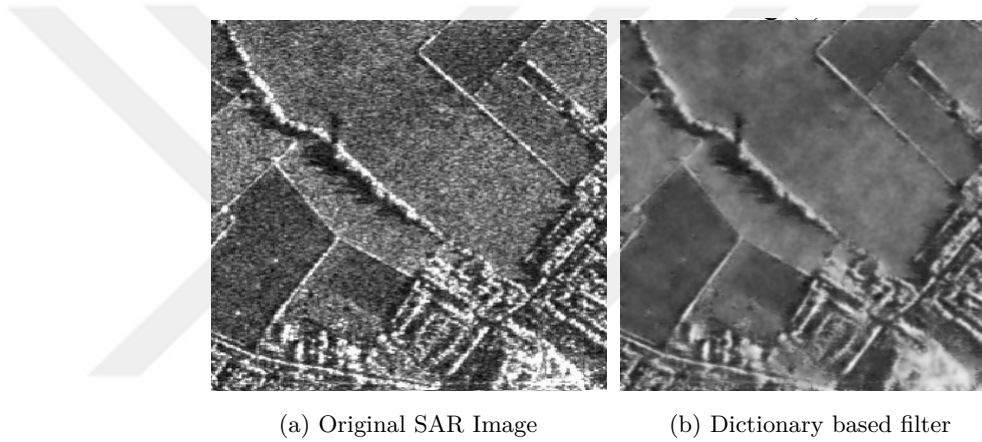


Figure 2.15: Effect of denoising for a real SAR image of Dictionary Learning Method

2.2.3.7 Sparsity-driven Methods

Sparsity-based approaches minimize a cost function as shown as in Equation 2.19 where G_i is an image, F_i is sparse coefficients in vector form, and ϕ is the sparsity inducing regularization term.

$$\min_{F_i} = \|DF_i - G_i\|_2^2 \text{ s.t. } \phi(G_i) \quad (2.19)$$

The choice of ϕ is the first important step of sparsity based approaches because the computation of the sparse linear combination coefficients depends on selecting ϕ which can be convex or non-convex. Sparsity-based approaches are useful for despeckling purpose because despeckled image is well represented by using generally a wavelet or 2D-DCT dictionary, but the speckle isn't. This means they keep the relevant information while discarding the irrelevant one. So, while calculating the sparse representation from the noisy signal, only clean signal is captured where noise is eli-

minated. And also to enforce the representation vector to be sparse, all the other low-energy noisy components will be eventually thresholded.

2.2.3.8 Variational Models Principle

The Total Variation (TV) that is introduced by Camille Jordan has been highly successful in a wide variety of despeckling problems. TV based despeckling methods are more efficient in preserving image textures and edges during despeckling. Variational methods are used to reduce noise from an image using an optimization approach, i.e. minimization of a cost function. The vector of p -point signal c is $f = [f(0), \dots, f(p-1)]^T$ where the ℓ_1 norm Equation 2.20 and ℓ_2 norm Equation 2.21 of the vector v is defined as below.

$$\|v\|_1 = \sum_p |v(p)| \quad (2.20)$$

$$\|v\|_2 = \sqrt{\sum_p |v(p)|^2} \quad (2.21)$$

An optimization problem is finding the largest or smallest value of a function which gives the best solution from all feasible solutions. The basic formulation of a variational optimization problem shown in Equation 2.22 in order to estimate input signal $F(n)$ that is a sparse, from the output signal data $G(n)$

$$\min_F = \frac{1}{2} \|G - HF\|_2^2 + \lambda \|F\|_1 \quad (2.22)$$

A variational speckle reduction filter is obtained by using a regularization term and data fidelity terms. The choice of the optimization method of such models includes the solution of nonlinear PDEs derived from the conditions of obligatory optimality criteria. Variable and PDE-based models make it particularly easy to apply geometric modulation in solutions obtained as noise-reduced images. Variational methods are used in conjunction with the following different methods such as image denoising like sharpening and super resolution, image segmentation, change estimation (Chen et al., 2014), sparse 3D reconstruction and monitoring (Xu et al., 2012; Behrooz et al., 2012).

Variational methods are stable that work at all speckle levels. So various methods are proposed to minimize the related optimization energy functions constructed with a regularization (smoothing) term and a data fitting term. The first successful TV despeckling model that referenced is Rudin-Osher-Fatemi (ROF) (Rudin et al., 1992) method that uses a noise reduction approach that preserves the edges by applying the ℓ_1 - norm penalty to the derivatives of the reflecting values. Inspired by the ROF model, Aubert and Aujol (AA) (Aubert and Aujol, 2008) developed an energy functional by applying a MAP-approximation. As a follow up, (Huang et al., 2009) proposed a new despeckling method based on TV via referencing the AA method. Because of the non-convexity of the cost function presented in the AA method, finding a global solution is challenging. However, Aubert and Aujol (Aubert

and Aujol, 2008) showed that the cost function of AA becomes convex in certain conditions. To overcome this problem, Bioucas-Dias and Figueiredo (Bioucas-dias and Figueiredo, 2010) apply the MAP estimation method called BF method by applying a logarithmic transformation to obtain a convex cost function for speckle noise reduction.

In a later study, an effective speckle noise reduction method with a single parameter is proposed which makes it possible to make the TV regularizer term as ℓ_0 -norm, fractional norm, and ℓ_1 -norm (Ozcan et al., 2016), namely sparsity driven despeckling (SDD). In a recent study, quadratic approximation in (Ozcan et al., 2016) is improved with quadratic-linear (QL) approximation for ℓ_1 -norm-case which leads to better despeckling with lower execution times (Nar, 2018a), namely SDD with QL (SDD-QL). Accuracy parameter of TV regularization term in SDD-QL is changed adaptively in iterations which leads to same despeckling result, with up to an order of magnitude faster execution times, which is called as Fast SDD-QL (Nar and Atasoy, 2018).

2.2.4 Sparsity-Driven Methods

2.2.4.1 Rudin, Osher and Fatemi

Rudin, Osher and Fatemi (ROF) model uses the TV modifier instead of the Tikhonov regularizer in order to provide edge protection for noise reduction. ROF is a well-known example of PDE-based edge preserving noise reduction method.

In the ROF model, a noise reduction approach that preserves the edges by applying the ℓ_1 - norm penalty to the derivatives of the reflectance values in the image is obtained. As it is first proposed by (Rudin et al., 1992), ROF model assumes that the additive noise is in form of Gaussian distribution where noise reduction is achieved by minimization of below variational cost function:

$$J_{ROF}(F) = \sum_p (F_p - G_p)^2 + \lambda_s |(\nabla F)_p| \quad (2.23)$$

where G is the observed image with speckle noise, F is the speckle reduced image, p is the pixel index number in the image, λ_s is the smoothing level for multiplicative noise, and ∇ is a gradient operator. In the cost function, the first terms is the data fidelity term, which ensures F to be similar to G , due to Gaussian distribution. The second term is a TV regularization term, which implies a penalty on the changes in image gradients. Because of the TV regularization term implies a ℓ_1 -norm penalty, homogeneous regions are smoothed while features such as edges and point scatterers are preserved. The ℓ_1 norm of the minimizer λ_s is bounded, and the bound is independent of λ_s . However, ROF model is not suitable for SAR images since speckle noise in SAR images is multiplicative in nature.

The ROF minimization problem is given in Equation 2.23 for a noisy image $G : \Omega \rightarrow \mathbb{R}$, where Ω is bounded open subset of \mathbb{R}^2 , we need to obtain a clean image F (Osher et al., 2003). Two Lagrange multipliers is used a constrained optimization approach where $\int |G - F|^2 = \sigma^2$ is the estimated global variance of the additive noise. The average of the minimizer λ is the same as the average of the original image F . Inspired by ROF model, various TV based speckle reduction methods are

proposed for SAR images which employs so called variational methods (Aubert and Aujol, 2008; Durand et al., 2010; Bioucas-dias and Figueiredo, 2010; Liu and Zhu, 2013; Özcan et al., 2014).

2.2.4.2 Aubert and Aujol

The Aubert and Aujol (AA)(Aubert and Aujol, 2008) method uses a Bayesian MAP estimated model to reduce speckle which consists of a prior distribution of the multiplicative noise based data fidelity term and a TV regularization term. They use the optimization of a non-convex model and assumes that speckle noise as in the multiplicative form of Gamma distributed which reduce speckles in SAR images using non-convex variational cost function as given as below:

$$J_{AA}(\hat{F}) = \int_{\Omega} (\log F + \frac{G}{F}) + \int_{\Omega} |F| \quad (2.24)$$

where λ is positive regularization term, $\int |F|$ is the TV of G and \hat{F} is the despeckled image. To choose an optimal parameter λ for the AA is challenging.

AA model uses $g = f n_{multiplicative}$ noise model to propose a variational model where $f > 0$ and $f, g, n_{multiplicative}$ are instances of some random variables F, G and N . $P(F|G)$ is calculated by Bayes rule $P(F|G) = \frac{P(G|F)P(F)}{P(G)}$ and after minimizing the log-likelihood, AA they denote the set of the pixels of the image by S and s the samples of the noise on each pixel $s \in S$ and minimized the Equation below:

$$-\log(P(G|F)) - \log(P(F)) = -\log(P(G(s)|F(s))) - \log(P(F(s))) \quad (2.25)$$

The works of (Osher et al., 2003; Rudin et al., 1992) leads AA to choose $\omega(u) = J(u)$ and propose the image restoration model below:

$$\inf_{f \in S(\Omega)} J(f) + \lambda \int_{\Omega} (\log F + \frac{G}{F}) \quad (2.26)$$

To numerically compute the Equation 2.26, AA, we use $-div \frac{\nabla f}{|\nabla f|}$ to drive to a steady state below:

$$\begin{aligned} \frac{\partial f}{\partial t} &= div \frac{\nabla f}{|\nabla f|} + \lambda \frac{G - F}{F^2} \\ F(x, 0) &= \frac{1}{\Omega} \int_{\Omega} F \end{aligned} \quad (2.27)$$

AA uses explicit scheme as in equation below that creates numerical instability unless the time step in simulation is small enough, so the time step that greater than zero must be as minimum as possible. If the iteration of F_n increases, β must be adjusted to a small fixed parameter.

$$\frac{f_{n+1} - f_n}{\partial t} = div \frac{\nabla f_n}{\sqrt{|\nabla f|^2 + \beta^2}} + \lambda h'(f_n) \quad (2.28)$$

The despeckling quality is limited due to the local solutions obtained during minimization in AA. They developed an explicit numerical scheme for the minimization

that converge to a local minimum as a solution. The quality of despeckled image may be low due to the obtained local minimum solution. The step size effect is dominant so it is recommended by authors using 0.1 for step size to get stable results.

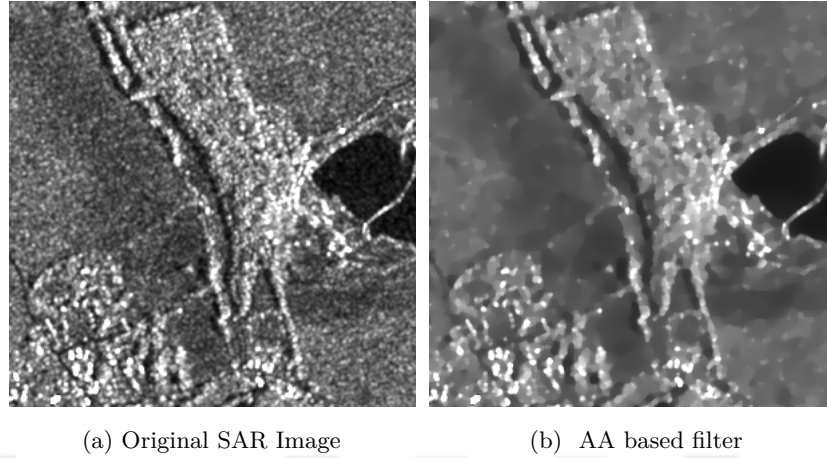


Figure 2.16: Application of AA based filter to the original SAR image

2.2.4.3 Sparsity-Driven Despeckling

In a later study, an effective despeckling noise reduction method with a single parameter is proposed that makes it possible to make the TV regularizer term as ℓ_0 -norm, fractional norm, and ℓ_1 -norm (Ozcan et al., 2016), namely sparsity driven despeckling (SDD). SDD prevents the deterioration of the edges and point scatters in the image, while ensuring a successful softening of the homogeneous regions. Therefore, for each pixel in the image, a better noise reduction is achieved using the appropriate fractional norm. The use of a non-local average filter also protects the textural regions on the image. SDD is formulated as in Equation 2.29.

$$J_{SDD}(F) = \sum_p (F_p - \hat{G}_p)^2 + \lambda \Lambda_p(|(\partial F)_p|, f) \quad (2.29)$$

where \hat{G} is the observed speckled image, F is the speckle-reduced image, p is the index number of pixel in the image, λ is the smoothing level, f is the norm value to be applied within TV regularization, and $\Lambda_p(|(\partial F)_p|, f)$ is exponentiation operator defined as:

$$\Lambda_p(|(\partial F)_p|, f) = \begin{cases} 0 & \text{for } x = 0, f = 0 \\ x^f & \text{otherwise} \end{cases} \quad (2.30)$$

for obtaining ℓ_0 - norm when f is 0. In the cost function, the first term is defined as a data fidelity term, which ensures F to be similar to G . The second term is a TV regularization term, which implies a penalty on the changes in image gradients. In this formulation, ℓ_0 - norm is obtained when f is 0, ℓ_1 - norm is obtained when f is 1, and fractional norm is obtained when f is between 0 and 1, where they all induce a sparse solution

SDD (Ozcan et al., 2016) is improved with quadratic-linear (QL) approximation for ℓ_1 -norm case which leads to better despeckling with lower execution times (Nar,

2018b), namely SDD with QL (SDD-QL). In SDD method, speckle reduction in the SAR images is defined as the minimization of the following variational cost function with respect to f using an adaptive data fidelity term:

$$J_{SDD-QL}(F) = \sum_p (F_p - \hat{G}_p)^2 + \lambda |(\nabla F)_p| \quad (2.31)$$

where F is speckle noise reduced image, G is image with speckle noise, first term is a data fidelity term dictated by additive noise with Gaussian distribution, λ is a small positive constant weighting the contribution of additive noise, second term is TV regularization term to enforce smoothness, ∇ is the gradient operator, and λ_s is positive value which determines the smoothing level, p is the pixel index number. In the cost function, the data fidelity term ensures f having reflectivity values close to g in ℓ_2 - *norm* manner and ℓ_1 - *norm* manner penalty on image gradients is applied by TV regularization term.

In (Nar and Atasoy, 2018) an efficient mechanism to increase the speed of SDD-QL and SDD method up to an order of magnitude while obtaining the same or better despeckling result is proposed, namely Fast SDD-QL. Fast SDD-QL method can be order of magnitude faster comparing to SDD-QL method and much faster than SDD method especially when accurate despeckling is required, i.e. by using small ϵ value such as 10^{-5} . Although, Fast SDD-QL method brings significant speed ups comparing to SDD method and SDD-QL method, despeckling result is same with SDD-QL method and better than SDD method. Additionally, Fast SDD-QL method can be used for generating nonlinear scale space without no extra computation.

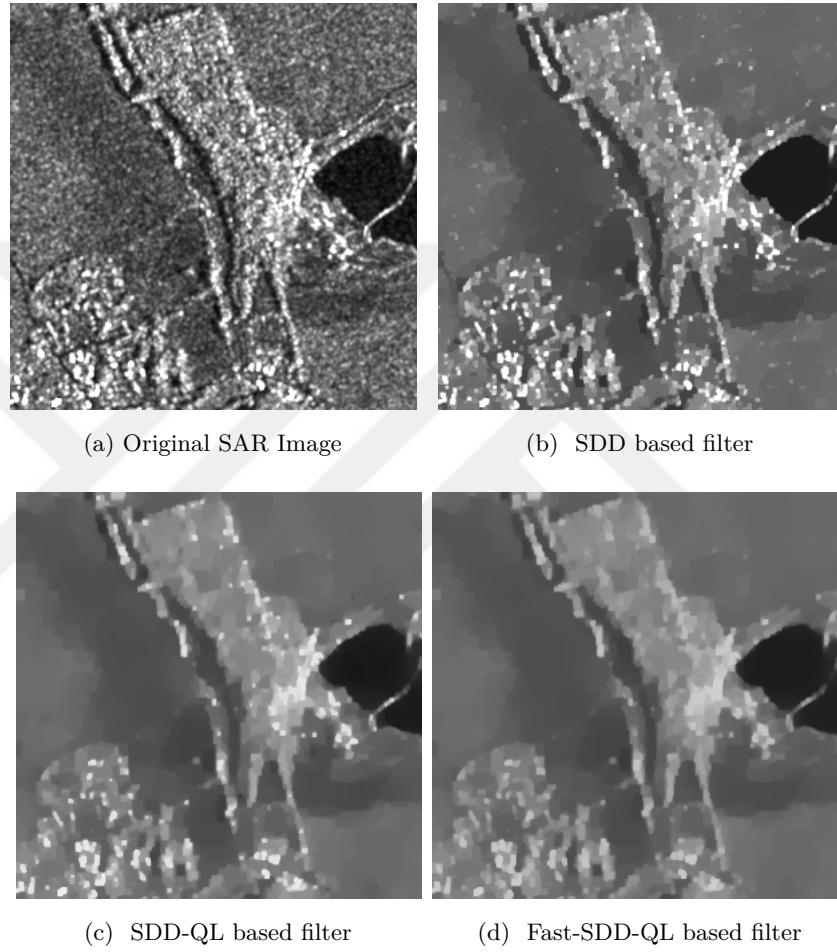


Figure 2.17: Application of SDD, SDD-QL and Fast SDD-QL based filters to the original SAR image

CHAPTER 3

MULTIPLICATIVE ADDITIVE DESPECKLING (MAD)

Speckle reduction in a SAR image can be cast as an optimization problem where despeckled image is the solution obtained by minimizing a cost function for a given noisy image. In general, such a cost function reaches its minimum value when cost function terms provides maximum utility with respect to parameters. Among the family of the cost functions, variational cost functions have desirable characteristics for preserving the details while filtering the noise. In general, variational cost functions contain a data fidelity term and a regularization (i.e. smoothness) term in addition to problem specific terms. Data fidelity term tries to enforce a solution (i.e. despeckled image) close to the given noisy image while smoothness term tries to enforce smoothness on the solution such that image details (i.e. edges and point scatterers) are preserved. Therefore, there is a trade-off between fidelity to data and smoothness of the solution which is generally controlled by a parameter (i.e. $\lambda \geq 0$).

Multiplicative Additive Despeckling (MAD) is expressed as a minimization of a variational cost function given in Equation 3.1, as an optimization problem.

$$\hat{F} = \operatorname{argmin} J_{MAD}(F) \quad (3.1)$$

Above optimization model aims to determine the best possible choice of a vector that represents the speckle reduced SAR image. The variable F represents the choice made; the objective value $J_{MAD}(F)$ represents the cost of choosing F for utility. At last, cost function $J_{MAD}(F)$ is minimized with respect to F . In this section, we present a fast and efficient method for SAR image despeckling based on minimization of a variational cost function given in Equation 3.1.

3.1 Proposed Cost Function

The cost function $J_{MAD}(F)$ is defined as given in Equation 3.2 which is minimized with respect to F . This cost function can be modeled for the additive noise as proposed in ROF model (Rudin et al., 1992) or can be modeled for multiplicative noise as proposed in AA model (Aubert and Aujol, 2008). However, general speckle noise model assumes that SAR images contains both multiplicative and additive noise where additive noise has minor contribution. Therefore, in this thesis, ROF model and AA model are combined to deal with general speckle model as given in Equation 2.3 which contains an additive noise term in addition to a multiplicative noise term.

Proposed MAD method suggests the below variational cost function (Equation 3.2) with a multiplicative and an additive data fidelity terms to reduce speckle noise.

$$J_{MAD}(F) = \sum_p \left(\log F_p + \frac{G_p}{F_p} \right) + \lambda_a (F_p - G_p)^2 + \lambda_s |(\nabla F)_p| \quad (3.2)$$

where F is speckle noise reduced image, G is image with speckle noise, first term is a data fidelity term dictated by multiplicative noise with Gamma distribution, second term is a data fidelity term dictated by additive noise with Gaussian distribution, λ_a is a small positive constant weighting the contribution of additive noise, third term is TV regularization term to enforce smoothness, ∇ is the gradient operator, and λ_s is positive value which determines the smoothing level.

3.2 Minimization of the Cost Function

The first data fidelity term, that models the multiplicative noise, in Equation (3.2) is non-convex. However, as shown in (Aubert and Aujol, 2008), in certain conditions data fidelity term for the multiplicative noise becomes convex. In addition, the absolute operator in TV regularization term is non-differentiable. Thus, efficient optimization of MAD cost function, especially obtaining the global optimum, is challenging. In this thesis, the absolute value operator is approximated and convex relaxation methods are used for multiplicative fidelity term to obtain a differentiable cost function which leads to an effective numerical minimization scheme.

For the approximation of the multiplicative fidelity term, this term is expanded using the first-order Taylor expansion which leads to a convex term as in Equation 3.3 where \hat{F}_p represents a delegate constant simultaneously as the same value as F_p .

$$\begin{aligned} \log(F_p) + \frac{G_p}{F_p} &\approx m_p F_p + c_p \\ m_p &= \frac{1}{\hat{F}_p} - \frac{G_p}{\hat{F}_p^2} \\ c_p &= \log \hat{F}_p + \frac{2G_p}{\hat{F}_p} - 1 \end{aligned} \quad (3.3)$$

Despite the success of detail preservation of ℓ_1 -norm TV regularization, its efficient minimization is challenging since absolute function is not differentiable. Therefore, the absolute operator is quadratically approximated as below:

$$|z| \approx \frac{z^2}{|\hat{z}| + \varepsilon} \quad (3.4)$$

where \hat{z} is a surrogate constant for the value of z and ε is a constant small value with $\varepsilon > 0$.

To improve approximation accuracy, ε should be decreased as much as to 0. Therefore, above quadratic approximation can be applied to TV regularization term as given in Equation 3.5:

$$\begin{aligned} |(\partial F)_p| &= |(\partial F_x)_p| + |(\partial F_y)_p| \\ &\approx \frac{(\partial_x F)_p^2}{|(\partial_x \hat{F})_p| + \varepsilon} + \frac{(\partial_y F)_p^2}{|(\partial_y \hat{F})_p| + \varepsilon} \end{aligned} \quad (3.5)$$

Since \hat{F}_p is momentarily fixed and assumed to be constant, Equation 3.5 can be written as below.

$$|(\partial F)_p| \approx (W_x)_p (\partial_x F)_p^2 + (W_y)_p (\partial_y F)_p^2 \quad (3.6)$$

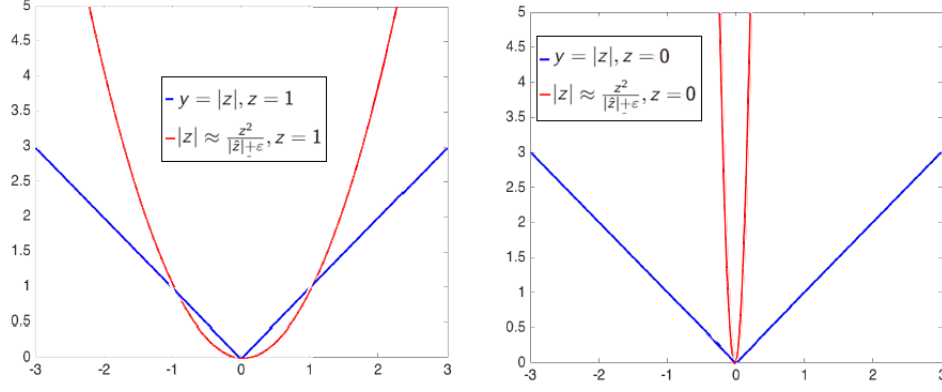


Figure 3.1: Absolute function and quadratic approximations of absolute function for different z values ($z = 0$ and $z = 1$)

where

$$(W_x)_p = (|(\partial_x \hat{F})_p| + \varepsilon)^{-1} \quad \text{and} \quad (W_y)_p = (|(\partial_y \hat{F})_p| + \varepsilon)^{-1} \quad (3.7)$$

Absolute function can also be approximated using below linear approximation:

$$|z| \approx \text{sgn}(\hat{z})z \quad (3.8)$$

where $\text{sgn}(\cdot)$ is the signum function, and $\text{sgn}(\hat{z})z$ is the linear approximation of $|z|$. Approximation given in Equation 3.8 can be applied to TV regularization term as given in Equation 3.10.

$$\begin{aligned} |(\partial F)_p| &= |(\partial F_x)_p| + |(\partial F_y)_p| \\ &\approx \text{sgn}((\partial_x \hat{F})_p)(\partial_x F)_p + \text{sgn}((\partial_y \hat{F})_p)(\partial_y F)_p \end{aligned} \quad (3.9)$$

Which can be written as:

$$|(\partial F)_p| \approx (S_x)_p(\partial_x F)_p + (S_y)_p(\partial_y F)_p \quad (3.10)$$

where

$$(S_x)_p \approx \text{sgn}((\partial_x \hat{F})_p) \quad \text{and} \quad (S_y)_p \approx \text{sgn}((\partial_y \hat{F})_p) \quad (3.11)$$

However, above approximation is numerically unstable. Therefore, as proposed in (Nar, 2018a), Equation 3.4 and Equation 3.8 is further improved by combining them as given in Equation 3.12 as below where $0 \leq \alpha < 1$.

$$|z| \approx (1 - \alpha)(|\hat{z}| + \varepsilon)^{-1}z^2 + \alpha \text{sgn}(\hat{z})z \quad (3.12)$$

Then $|(\nabla F)_p|$ can be expanded as $|(\partial F_x)_p| + |(\partial F_y)_p|$ and finally written as:

$$\begin{aligned} |(\nabla F)_p| &= (1 - \alpha)((W_x)_p(\partial_x F)_p^2 + (W_y)_p(\partial_y F)_p^2) \\ &\quad + \alpha((S_x)_p(\partial_x F)_p + (S_y)_p(\partial_y F)_p) \end{aligned} \quad (3.13)$$

Quadratic and linear approximations are combined to form Equation 3.12 which is accurate around \hat{z} (see Figure 3.2). As z decreases and converges to 0, contribution of linear term becomes smaller. When z becomes 0, linear term vanishes and only quadratic term remains. In this quadratic form, not only absolute function is smoothed but also staircase artifacts are also eliminated which is a common problem of ℓ_1 -norm TV smoothing.

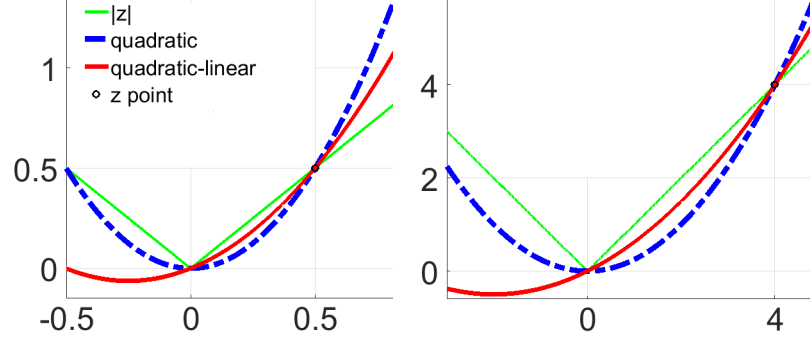


Figure 3.2: MAD ($\alpha = 0.5$) ℓ_1 -norm approximations at 0.5 and 4.0

Using the approximations in Equation 3.3 and Equation 3.12, cost function given in Equation 3.2 is rewritten as in Equation 3.14. Due to the applied approximations, the Equation 3.12 only affects \hat{F} and is solved in an iterative way, with an iteration index n . A new regularization term with coefficient λ_p is added in order to balance the trade-off between approximation accuracy and computational efficiency.

Then, using the MAD approximation in Equation 3.13, below approximated cost function in Equation 3.2 is obtained:

$$\begin{aligned} \hat{J}_{MAD}^{(n)}(F) = & \sum_p (m_p F_p + c_p) + \lambda_a (F_p - G_p)^2 \\ & + \lambda_s [(1 - \alpha)((W_x)_p (\partial_x F)_p^2 + (W_y)_p (\partial_y F)_p^2) \\ & + \alpha((S_x)_p (\partial_x F)_p + (S_y)_p (\partial_y F)_p)] \\ & + \lambda_P (F_p - \hat{F}_p)^2 \end{aligned} \quad (3.14)$$

where n represents the iteration index, \hat{F}_p is a surrogate constant for F_p , $(F_p - \hat{F}_p)^2$ is a slow-step regularization (SSR) term for keeping F_p close to \hat{F}_p since employed approximation is accurate in the neighborhood of \hat{F}_p , γ is a positive weight of SSR term, $(W_x)_p = (|\partial_x \hat{F}_p| + \varepsilon)^{-1}$, $(W_y)_p = (|\partial_y \hat{F}_p| + \varepsilon)^{-1}$, $(S_x)_p = \text{sgn}((\partial_x \hat{F}_p)_p)$, $(S_y)_p = \text{sgn}((\partial_y \hat{F}_p)_p)$, and α is a parameter ($0 \leq \alpha < 1$) for controlling the approximation of the absolute function. Here, ε is approximation accuracy parameter ($\varepsilon > 0$) where accuracy of approximation gets better as ε gets smaller. Note that, $|\nabla F|_p$ in Equation 3.2 is taken as sum of $|\partial_x F|_p + |\partial_y F|_p$ and then approximated where its final form is given in Equation 3.14. Superscript n in $J^{(n)}(f)$ represents the iteration index since employed approximations on the proposed cost function require minimization to be done in an iterative manner.

Finally, methods of linear algebra can be utilized to minimize the cost function by

transforming the Equation 3.14 into a matrix-vector form as below:

$$\begin{aligned}
\hat{J}(V_f) &= (V_m^\top V_f + \vec{1}^\top V_c) + \lambda_a (V_f - V_g)^\top (V_f - V_g) \\
&+ \lambda_s [(1 - \alpha)(V_f^\top \mathbf{C}_x^\top \mathbf{W}_x \mathbf{C}_x V_f + V_f^\top \mathbf{C}_y^\top \mathbf{W}_y \mathbf{C}_y V_f) \\
&+ \alpha(S_x^\top \mathbf{C}_x V_f + S_y^\top \mathbf{C}_y V_f)] \\
&+ \lambda_P (V_f - V_{\hat{f}})^\top (V_f - V_{\hat{f}})
\end{aligned} \tag{3.15}$$

where V_f , $V_{\hat{f}}$, V_g , V_m , V_c , S_x , and S_y symbols are vector forms of F , \hat{F} , G , m_p , c_p , $(S_x)_p$, and $(S_y)_p$. As a constant vector, $\vec{1}$ is formed with all ones. Also, \mathbf{C}_x and \mathbf{C}_y are discrete gradient operators (as Toeplitz matrices, with zero derivatives at the right and bottom of the matrices), and \mathbf{W}_x and \mathbf{W}_y are diagonal matrices for representing the operations on $(W_x)_p$ and $(W_y)_p$. Note that, vectors have size of $k \times 1$ and matrices have size of $k \times k$ where k represents the pixel count in the SAR image. Although, $k \times k$ is a huge matrix size even for a moderate size image (i.e. $k = 10^6$ for an image with size of 1000×1000), all the matrices are sparse so memory and computational requirements for operating on these matrices become tractable.

Minimization of Equation 3.15 leads to a unique global minimum since it is strictly convex. Therefore, to minimize it, derivative of the Equation 3.15 is taken with respect to V_f as shown in Equation 3.16.

$$\begin{aligned}
\frac{\partial \hat{J}^n(V_f)}{\partial V_f} &= V_m + 2\lambda_a (V_f - V_g) \\
&+ 2\lambda_s [(1 - \alpha)(\mathbf{C}_x^\top \mathbf{W}_x \mathbf{C}_x V_f + \mathbf{C}_y^\top \mathbf{W}_y \mathbf{C}_y V_f) \\
&+ \alpha(\mathbf{C}_x^\top S_x + \mathbf{C}_y^\top S_y)] \\
&+ 2\lambda_P (V_f - V_{\hat{f}})
\end{aligned} \tag{3.16}$$

The Equation 3.16 is equalized to zero and then below linear system is obtained after some algebraic manipulations.

$$\begin{aligned}
\mathbf{A}V_f^{(n+1)} &= b \\
\mathbf{A} &= (\lambda_a + \lambda_p)\mathbf{I} + \lambda_s(1 - \alpha)\mathbf{L} \\
b &= \lambda_a V_g + \lambda_p V_{\hat{f}} - 0.5V_m - \lambda_s(\alpha/2)(\mathbf{C}_x^\top S_x + \mathbf{C}_y^\top S_y)
\end{aligned} \tag{3.17}$$

where $\mathbf{L} = \mathbf{C}_x^\top \mathbf{W}_x \mathbf{C}_x + \mathbf{C}_y^\top \mathbf{W}_y \mathbf{C}_y$ with \mathbf{I} is being the identity matrix. In case iteration index is not explicitly stated, n is the iteration index for the \mathbf{A} , \mathbf{L} , \mathbf{W}_x , \mathbf{W}_y , b , V_f , $V_{\hat{f}}$, S_x , and S_y . Here, \mathbf{A} is a positive definite (PD) and 5-point Laplacian matrix which is also sparse. Equation 3.15 is strictly convex since \mathbf{A} is a PD matrix; thus, its minimization leads to the global optimum solution.

Applied approximations and obtained iterative minimization approach can be implemented easily in any programming language based on the given pseudo-code in the Algorithm 1. In the MAD method, linear system as given as $\mathbf{A}V_f^{(n+1)} = b$ is the most computational line, all other lines are computationally cheap. However, this linear system is efficiently solved using preconditioned conjugate gradient (PCG) method since \mathbf{A} is PD and sparse where incomplete Cholesky preconditioner (ICP) is used. For the PCG method, convergence tolerance and maximum iteration are set to 10^{-2} and 10^2 , respectively. Note that, \mathbf{A} , \mathbf{L} , \mathbf{C}_x , \mathbf{C}_y , \mathbf{W}_x , \mathbf{W}_y in the Algorithm 1 are

sparse with regular structures so that they can be stored efficiently (i.e. as arrays) and operations on them can be done efficiently.

In MAD method, homogeneous regions become smoother while edges are being preserved especially in the last iterations. Essentially in MAD, in the first iterations smoothing is happening similar to ℓ_2 -norm manner while in the last iterations smoothing is happening in ℓ_1 -norm manner. This behavior can be controlled by changing ε such that $\varepsilon = 1$ will lead to a smoothing similar to using ℓ_2 -norm TV term while small values of ε will lead to a smoothing using ℓ_1 -norm TV term. Instead of using a fixed ε value, we adaptively change the ε such that ε is 1 in first iteration and converges to desired value as iteration proceeds as suggested in (Nar, 2018b). In ℓ_1 -norm TV filtering, condition number (CN) of \mathbf{A} gets higher as ε gets smaller. Higher CN means ill-posed linear system which requires more PCG iterations. Therefore, as proposed in (Nar, 2018b), adaptively changing ε from 1 to a lower value as iteration proceeds saves a considerable amount of computation, especially when small ε value is used. Proposed approach in (Nar, 2018b) is also easy to implement and requires no extra computation since it does only simple scalar computations (3 lines in Algorithm 1 that contains $\varepsilon_{desired}$ and $\varepsilon_{decrement}$) to calculate adaptive ε .

Algorithm 1 *Multiplicative Additive Despeckling*

Input: $g, \lambda_s, \lambda_p, \lambda_a, \alpha, \varepsilon_{desired}, n_{max}$

- 1: $V_f \leftarrow V_g \leftarrow g$ ▷ assign image data g to vectors V_g and V_f (initial solution)
 - 2: $\varepsilon_{desired} = \min(\varepsilon_{desired}, 0.1)$ ▷ $\varepsilon_{desired} \leq 0.1$
 - 3: $\varepsilon_{decrement} = \frac{1 - \varepsilon_{desired}}{n_{max}}$ ▷ initialization for the proposed adaptive ε
 - 4: **for** $n = 1 : n_{max}$ **do**
 - 5: $\varepsilon = 1 - n\varepsilon_{decrement}$ ▷ assignment for the proposed adaptive ε
 - 6: $V_{\hat{f}} \leftarrow V_f$ ▷ assign V_f to proxy constant $V_{\hat{f}}$
 - 7: $\mathbf{W}_x \leftarrow [\text{diag}(|\mathbf{C}_x V_{\hat{f}}| + \varepsilon)]^{-1}$ ▷ $\mathbf{C}_x V_{\hat{f}}$ is x -derivative of V_f
 - 8: $\mathbf{W}_y \leftarrow [\text{diag}(|\mathbf{C}_y V_{\hat{f}}| + \varepsilon)]^{-1}$ ▷ $\mathbf{C}_y V_{\hat{f}}$ is y -derivative of V_f
 - 9: $S_x \leftarrow \text{sgn}(\mathbf{C}_x V_{\hat{f}})$ ▷ signum of x -derivative of V_f
 - 10: $S_y \leftarrow \text{sgn}(\mathbf{C}_y V_{\hat{f}})$ ▷ signum of y -derivative of V_f
 - 11: $\mathbf{L} \leftarrow \mathbf{C}_x^T \mathbf{W}_x \mathbf{C}_x + \mathbf{C}_y^T \mathbf{W}_y \mathbf{C}_y$ ▷ construct matrix \mathbf{L}
 - 12: $\mathbf{A} \leftarrow (\lambda_p + \lambda_a)\mathbf{I} + \lambda_s(1 - \alpha)\mathbf{L}$ ▷ construct matrix \mathbf{A}
 - 13: $b \leftarrow \lambda_a V_g + \lambda_p V_{\hat{f}} - 0.5V_m - \lambda_s(\alpha/2)(\mathbf{C}_x^T S_x + \mathbf{C}_y^T S_y)$ ▷ construct vector b
 - 14: **solve** $\mathbf{A}V_f = b$ ▷ to find V_f for the next iteration
 - 15: **end for**
 - 16: $f \leftarrow V_f$ ▷ converts vector V_f to an image f
- Output:** f ▷ returns despeckled image f
-

Diagonal dominance of the \mathbf{A} matrix can be controlled through α . Diagonal dominance increases as α gets closer to 1 which also increases the computational efficiency of the linear system solver. As a trade-off, numerical accuracy is decreased since TV diffusion term is calculated locally which causes dithering artifacts in noise reduced image. When α becomes 1, \mathbf{A} becomes a diagonal matrix where linear system (Equation 3.17) is solved in extremely efficient manner in each MAD iteration. However, solver become explicit and numerically unstable which causes outer iteration (n_{max}) to increase significantly. And even if n_{max} is increased, obtained solution is not satisfactory due to numerical instability. For $\alpha < 1$, \mathbf{A} is PD and sparse so that it can be solved using PCG which is well known efficient iterative solver for such matrices. When α decreases and gets closer to 0, efficiency of linear system solver in each MAD iteration decreases since \mathbf{A} become less diagonally dominant. Yet, only few outer iterations (i.e. $n_{max} = 5$) is sufficient since TV diffusion becomes more global.

Experiments show that vicinity 0.5 is good value for α as it provides a well balanced trade-off for the accuracy, numerical stability, and computational efficiency. Thus, $\alpha = 0.5$ is used as a default value in this thesis.

3.3 Convexity analysis

In this section MAD method is analyzed analytically and experimentally to present its convergence properties. First of all, for analytical analysis, strict convexity of the approximated cost function is shown. To do so, strict convexity of the Equation 3.15 is shown using the optimality conditions since Equation 3.15 is in a matrix-vector form and differentiable (Nocedal and Wright, 2006).

To satisfy the first order optimality condition, derivative of the Equation 3.15 is equalized to zero and a closed-form solution is obtained as shown in Equation 3.17.

For satisfying the second order optimality condition, second derivative should be taken where we define \mathbf{H} (Hessian) as the second derivative of the cost function $\hat{J}(V_f)$ (which is given in the Equation 3.15). Basically, if $\mathbf{H} \in \mathbb{R}^{k \times k}$ is PD then corresponding cost function $\hat{J}(V_f)$ is strictly convex. For PD check, $\mathbf{H} \succ 0$ should be satisfied where $\mathbf{H} \succ 0$ means $x^T \mathbf{H} x > 0$ for every $x \in \mathbb{R}$ with $x \neq 0$.

Lets take the second derivative of the convex cost function $\hat{J}(V_f)$ in Equation 3.15:

$$\frac{\partial^2 \hat{J}^n(V_f)}{\partial V_f^2} = 2\lambda_a + 2\lambda_p + 2\lambda_s[(1 - \alpha)\mathbf{L} = \mathbf{H} \quad (3.18)$$

Here, x is a non-zero vector and $\lambda_a, \lambda_p, +\lambda_s, (1 - \alpha)$ are all positive scalars; so, we should only show that $x^T \mathbf{L} x > 0$ to guarantee that $x^T \mathbf{H} x > 0$ for all non-zero x vectors. $x^T \mathbf{L} x > 0$ can be expanded as below into two inequalities after x^T and x are distributed from left and right onto L :

$$\begin{aligned} x^T(\mathbf{C}_x^T \mathbf{W}_x \mathbf{C}_x)x > 0, \quad x^T(\mathbf{C}_y^T \mathbf{W}_y \mathbf{C}_y)x > 0 \\ V_x^T \mathbf{W}_x V_x > 0, \quad V_y^T \mathbf{W}_y V_y > 0 \end{aligned} \quad (3.19)$$

where $V_x = \mathbf{C}_x x$ and $V_y = \mathbf{C}_y x$. Here, V_x and V_y are non-zero vectors since x is a non-zero vector and \mathbf{C}_x and \mathbf{C}_y are Toeplitz matrices with non-zero diagonal elements. Both inequalities are satisfied since \mathbf{W}_x and \mathbf{W}_y are all diagonal matrices with positive entries. Thus, it is shown that cost function $J^{(n)}(V_f)$ given in Equation 3.15 is strictly convex by the first order and second order optimality tests.

Finally, as an experimental convergence analysis, convergence of the original cost function and approximated cost function are analyzed. As seen in Figure 3.3, difference of cost values for Equation 3.15 and Equation 3.2 decreases steadily. Therefore, difference between Equation 3.2 and Equation 3.15 becomes negligible in the final iteration where minimum is obtained (see Figure 3.3). This shows that as iteration proceeds, they converge to the same solution within a small error bound which indicates that employed convex relaxation and approximations are successful. Therefore, we can conclude that original cost function and approximated cost function converges to the same global minimum (with a minimal numerical difference that can be ignored).

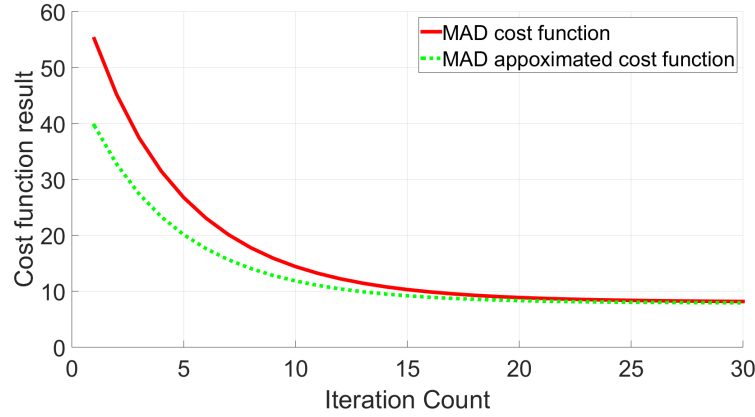


Figure 3.3: Difference between the original cost function in Equation 3.2 and the smoothly approximated cost function in Equation 3.15 ($\lambda_s = 1$).

3.4 Computational Complexity Analysis

This section presents computational complexity analysis of the proposed method to show its computational efficiency. First, computational complexity of every pseudo-code line inside the for loop in the Algorithm 1 is analyzed as shown in Table 3.1 and then overall computational complexity is determined as shown in Table 3.2

Line	code in Algorithm 1	Complexity
5	$\varepsilon \leftarrow 1 - n\varepsilon_{decrement}$	$o(1)$
6	$V_{\hat{f}} \leftarrow V_f$	$o(k)$
7	$\mathbf{W}_x \leftarrow [\text{diag}(\mathbf{C}_x V_{\hat{f}} + \varepsilon)]^{-1}$	$o(k)$
8	$\mathbf{W}_y \leftarrow [\text{diag}(\mathbf{C}_y V_{\hat{f}} + \varepsilon)]^{-1}$	$o(k)$
9	$S_x \leftarrow \text{sgn}(\mathbf{C}_x V_{\hat{f}})$	$o(k)$
10	$S_y \leftarrow \text{sgn}(\mathbf{C}_y V_{\hat{f}})$	$o(k)$
11	$\mathbf{L} \leftarrow \mathbf{C}_x^\top \mathbf{W}_x \mathbf{C}_x + \mathbf{C}_y^\top \mathbf{W}_y \mathbf{C}_y$	$o(k)$
12	$\mathbf{A} \leftarrow (\lambda_p + \lambda_a)\mathbf{I} + \lambda_s(1 - \alpha)\mathbf{L}$	$o(k)$
13	$b \leftarrow \lambda_a V_g + \lambda_p V_{\hat{f}} - 0.5V_m - \lambda_s(\alpha/2)(\mathbf{C}_x^\top S_x + \mathbf{C}_y^\top S_y)$	$o(k)$
14	solve $\mathbf{A}V_f = b$	$O(n_{pcg_{max}}k)$

Table 3.1: Computational complexity of the loop in MAD method

In the Equation 3.17, \mathbf{C}_x , \mathbf{C}_y , \mathbf{W}_x , \mathbf{W}_y , and \mathbf{L} are sparse matrices with size $k \times k$. Computational complexity in sparse matrices depends on sparsity ratio and pattern, i.e. if it has a regular structure or not. So the result of computational complexity in lines 6-13 in Algorithm 1 is $O(k)$. We used Incomplete Cholesky preconditioner (ICP) to solve $\mathbf{A}V_f = b$ and computational complexity is $n_{pcg_{max}}k$. In PCG, inverse of

the preconditioner matrices obtained using ICP are evaluated in linear time, using forward and backward Gaussian elimination. The dominant term in lines 5-14 is $n_{pcg_{max}}k$. These lines are in a for-loop with n_{max} iterations; therefore, computational complexity of the for-loop in the Algorithm 1 becomes $o(n_{max}n_{pcg_{max}}k)$.

Line	code in Algorithm 1	Complexity
1	$V_f \leftarrow V_g \leftarrow g$	$o(k)$
2	$\varepsilon_{desired} = \min(\varepsilon_{desired}, 0.1)$	$o(1)$
3	$\varepsilon_{decrement} = \frac{1-\varepsilon_{desired}}{n_{max}}$	$o(1)$
4 - 15	Table 3.1	$o(n_{max}n_{pcg_{max}}k)$
16	$f \leftarrow V_f$	$o(k)$

Table 3.2: Computational complexity of MAD

As shown in the Table 3.2, final computational complexity of the MAD method is $O(n_{max}n_{pcg_{max}}k)$ which is obtained by analysis of the Algorithm 1. Computational complexity of the Algorithm 1 shows that proposed method has linear execution time with respect to image size (k). Here, n_{max} and $n_{pcg_{max}}$ are generally fixed values and determined based on the image characteristics that MAD method will be executed on. Thus, it can be said that n_{max} and $n_{pcg_{max}}$ are almost a constant factor in the computational complexity.

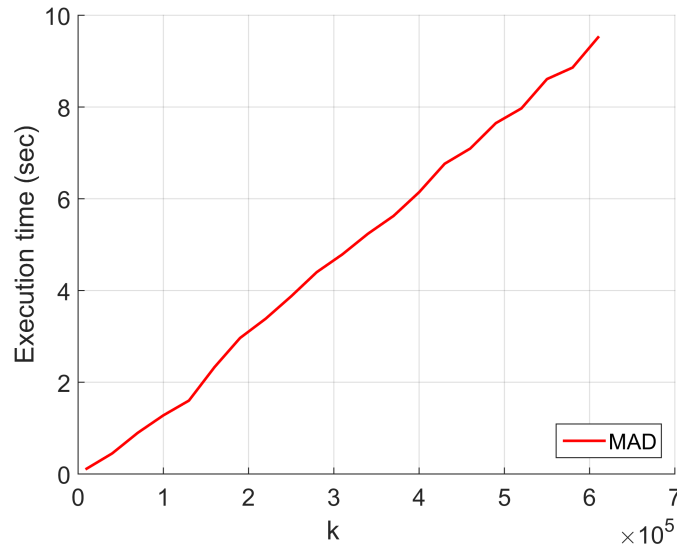


Figure 3.4: MAD Execution Time with respect to Image Size $k = (n \times n)$

As seen in Figure 3.4, actual execution time of MAD method is linear with respect to image size (k).

CHAPTER 4

EXPERIMENTAL ANALYSIS OF THE MULTIPLICATIVE
ADDITIVE DESPECKLING METHOD

In this chapter, MAD method is tested in order to measure its qualitative and quantitative performance by using synthetic images and real-world SAR images on a collection of data sets. Note that, MAD method is implemented using MATLAB R2015a and all the experiments are executed using an Intel i5-3210M 2.5GHz CPU and Windows operating system.

In first section, parameters of the MAD method are tested to show their effect on despeckling result. In second section, despeckling results are obtained using MAD method and compared with a state-of-the-art variational speckle noise reduction method, namely AA method. In third section, a systematic comparison with the five well-known despeckling methods in the literature is done: AA, SRAD, SAR-BM3D, Enhanced Lee, and Fast SDD-QL.

Test results are analyzed by visually and measurement using traditional performance measures such as structural-similarity-index (SSIM) as given in Appendix B, signal to-noise-ratio (SNR) as given in Appendix B, and peak signal-to-noise-ratio (PSNR) as given in Appendix B.

4.1 MAD Parameters Test on Synthetic Image

Proposed MAD method has four basic parameters: λ_s , ϵ , λ_a and λ_p . ϵ controls the approximation accuracy of the TV smoothing term. λ_a controls the contribution of additive data term. λ_s controls the smoothing level and λ_p controls the contribution slow-step regularization term.

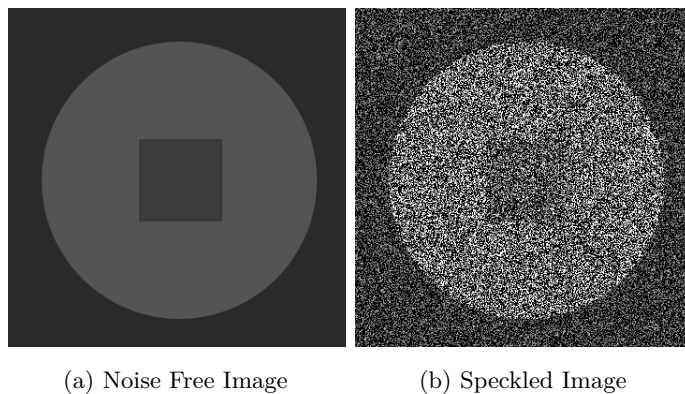


Figure 4.1: Synthetic Image (Aubert and Aujol, 2008)

To show the effects of MAD dominant parameters on despeckling quality, Figure 4.2 and Figure 4.3 are obtained by using different values of parameters with a synthetic image shown in Figure 4.1.

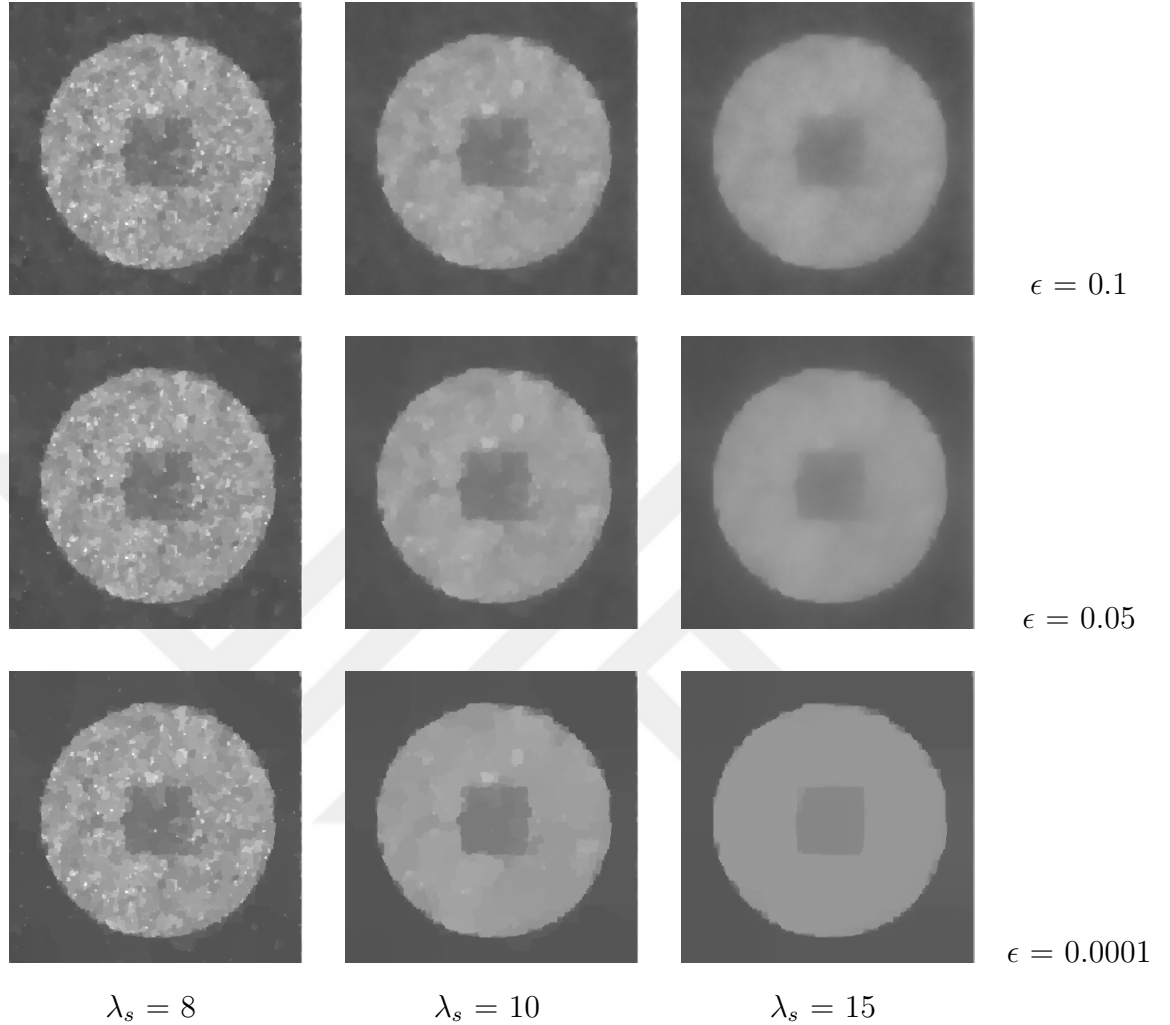


Figure 4.2: Speckle reduction results of MAD method using different λ_s and ϵ ($\lambda_a = 1$, $\lambda_p = 0.5$, $\alpha = 0.3$, $n_{max} = 50$ and image size = 364×367)

In Figure 4.2 λ_s and ϵ are changed and other parameters fixed. If λ_s increases and ϵ decreases regions become smoother and more flattened. As λ_s increases, smoothing level increases. As ϵ decreases, absolute operator becomes better approximated and sparsity is increased which leads to more flattened regions.

Using small ϵ represents small errors and increases the computation time. If λ_s decreases, the computation time increases in order to adapt a small converge. It is useful to use smaller ϵ in the high speckled images for best despeckling result and one should choose values of λ_s and ϵ based on the image noise level and desired flatness level in smoothed image.

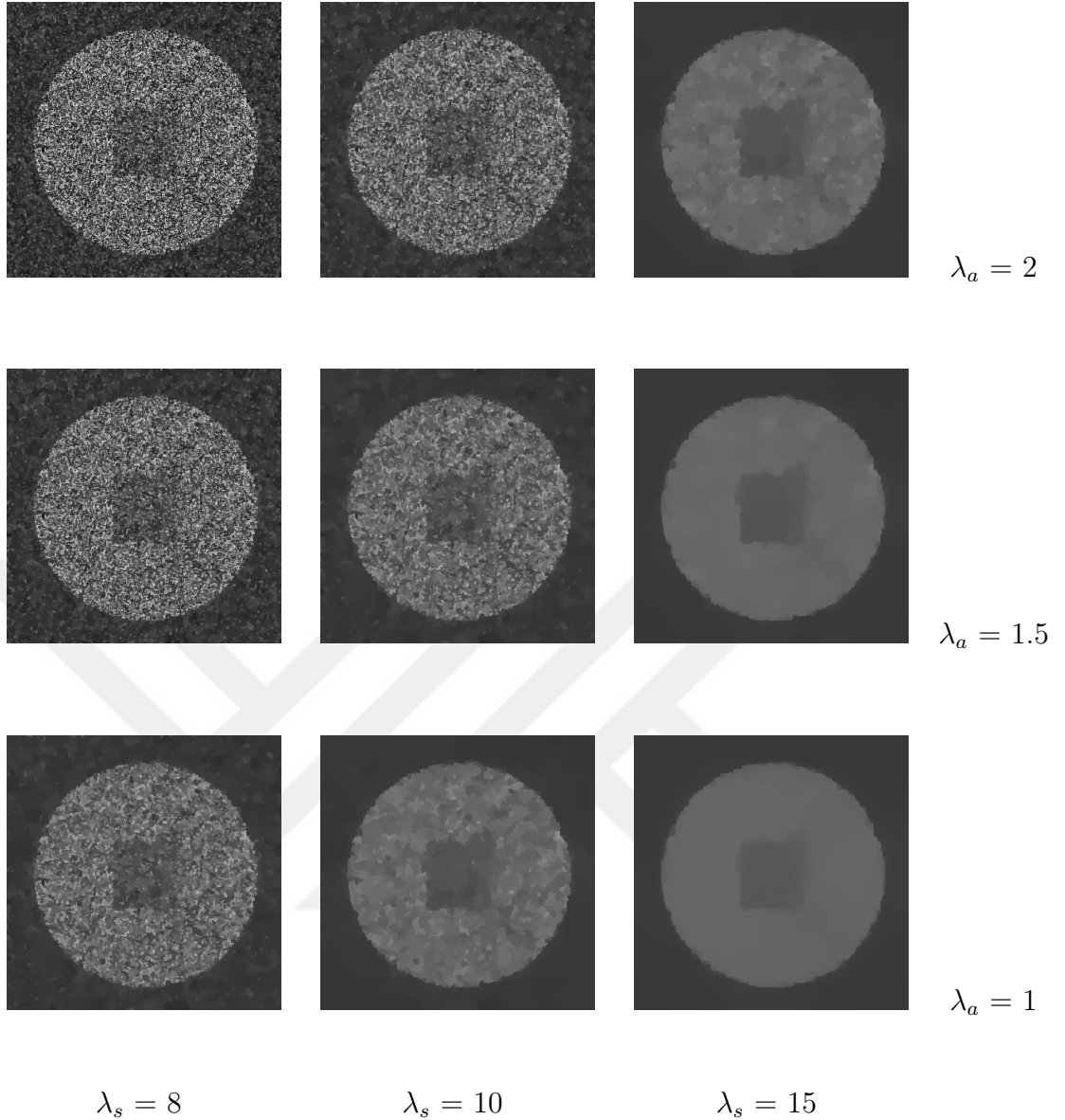


Figure 4.3: Speckle reduction results of MAD method using different λ_s and λ_a ($\epsilon = 10^{-5}$, $\lambda_p = 1$, $\alpha = 0.3$, $n_{max} = 50$ and image size = 362×361)

In Figure 4.3 λ_s and λ_a are changed and other parameters fixed to illustrate its impact on the despeckling λ_s and λ_a . If λ_s increases, smoothing increases. If λ_a increases fidelity to data increases (for additive noise, using Gaussian distribution) thus smoothing decreases.

In Figure 4.3 and 4.2 have same λ_a , λ_s and ϵ but λ_p is different. As seen in figures increasing of λ_p cause more smoothing.

Decreasing λ_a and increasing n_{max} and λ_p increases the computation time of speckling.

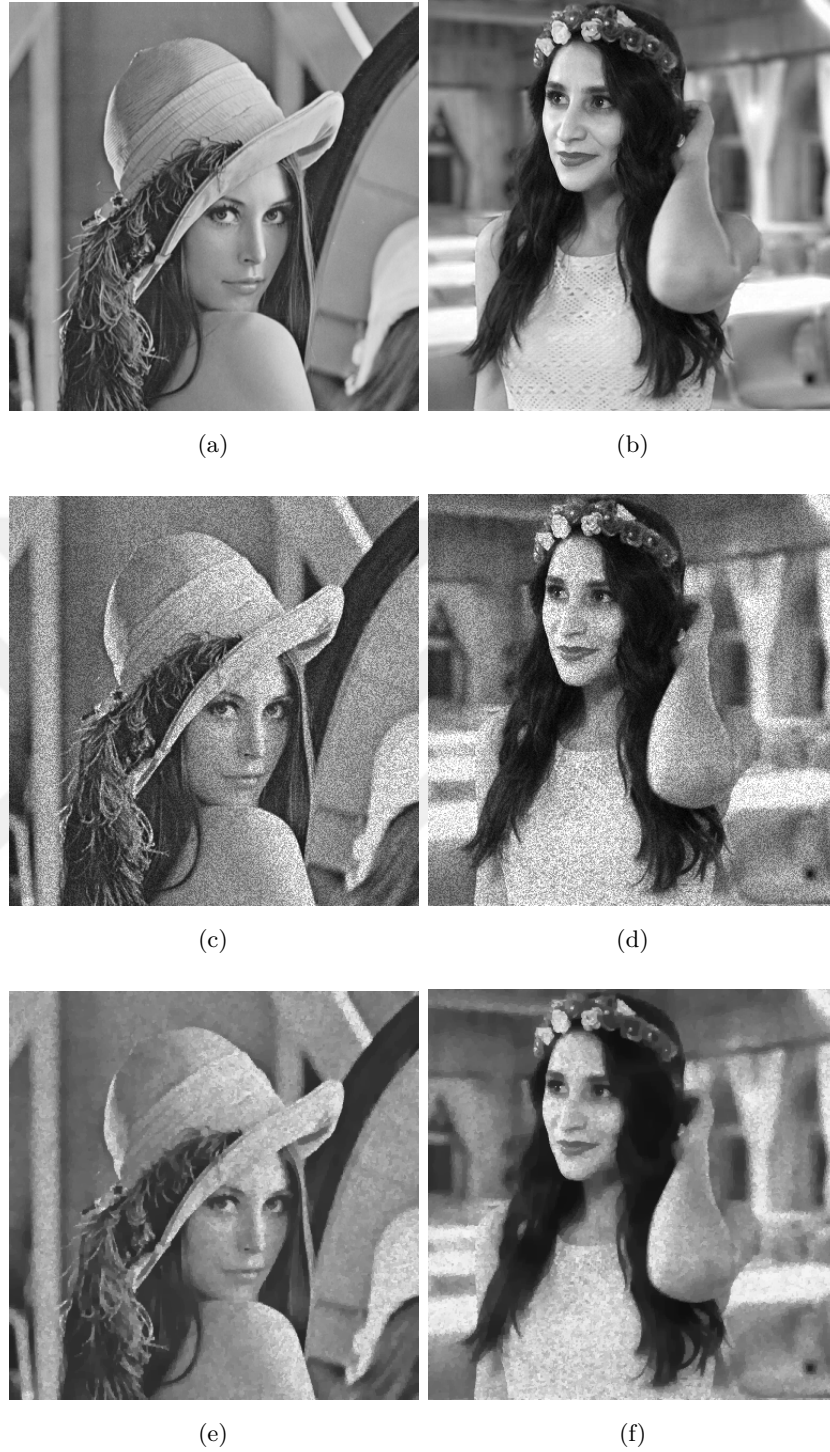


Figure 4.4: MAD based image denoising using different images with same parameters
(a) Original Lena image (b) Original Elif image (c) Noisy Lena image (d) Noisy Elif image (e) MAD denoised Lena image (f) MAD denoised Elif image

To show MAD visual effect on despeckling, set of test images and results related to MAD despeckling with same parameters are shown in Figure 4.4. These tests are performed on Lena image Figure 4.4.a and Elif image Figure 4.4.b with synthetically generated speckle noise.

Lena image contains rich set of structures so it has been widely used by image processing community. Elif image contains the image of my sister to introduce more variety into the tests. Speckled images in Figure 4.4.c (SNR:18.38 PSNR:23.93 SSIM:0.32) and Figure 4.4.d (SNR:18.78, PSNR:23.82, SSIM:0.32) are obtained by adding speckle noise with the same speckle noise generation parameters.

Figure 4.4.e (SNR:25.88 db, PSNR:31.50 db, and SSIM:0.46 db) and Figure 4.4.f (SNR:26.35 db, PSNR:31.45 db, and SSIM:0.53 db) are the MAD based despeckling results for the images in Figure 4.4.c and Figure 4.4.d with same MAD parameters ($\lambda_s = 60$, $\lambda_a = 0.9$, $\lambda_p = 1$, $\epsilon = 10^{-4}$, $\alpha = 0.3$).

Figure 4.4.e and Figure 4.4.f shows values of different metrics between noisy and speckle noise reduced Lena image (SNR:7.56 PSNR:7.62 SSIM:0.20) and Elif image (SNR:7.49 PSNR:7.57 SSIM:0.13). These tests show that, MAD method has stable and similar results with same parameters independent from which image is used if images have similar speckle noise levels. This gives an advantage in computational efficiency of determining the despeckling parameters in small sized images and applying them to the rest of the images or determining the SAR systems best despeckling parameters from training data and applying them to the test data.

4.2 Comparison of MAD and AA Method

AA is a one of the most used state-of-the-art speckle reduction methods. MAD is derived from AA and ROF to overcome AA and ROF disadvantages with an improved numerical approach to increase speckle reduction performance, so we test MAD and AA that has better performance compared to ROF for multiplicative noise.

Experimental studies on synthetic Lena (383×383 pixels), Elif (384×385 pixels) and testImage (383×291 pixels) images as shown in Figure 4.5 were performed using MAD and AA methods.



Figure 4.5: Synthetic Images used for Comparison MAD and AA

Speckle noise is obtained by adding speckle at different variance values (0.0005, 0.03, and 0.5) which creates low, mid and high level of speckle noise. Third column of Table 4.1 shows the quality metrics (SNR, PSNR, and SSIM) of speckling levels for the images.

The best metrics calculated by finding the highest SNR values by changing the each methods parameters in an iterative way and used $SNR_{(J_m^{(n+1)})} < SNR_{(J_m^{(n)})}$ (J_m : Method, n : iteration index) as the stop condition. Thus, best result is obtained for each method which allows comparison of the methods in a fair way.

Table 4.1 gives information about MAD and AA despeckling methods for the same speckle level where images are created using this technique for each row. MAD provides best despeckling results as seen in Table 4.1.

		Noise Levels (db)		
		Speckled Image	MAD	AA
Image Name				
Lena	SNR	26.03	30.77	29.33
	PSNR	31.63	36.38	34.95
	SSIM	0.68	0.88	0.83
	SNR	18.38	26.12	24.26
	PSNR	23.93	31.76	29.90
	SSIM	0.39	0.78	0.67
	SNR	7.85	19.88	16.92
	PSNR	13.03	25.56	22.88
	SSIM	0.09	0.62	0.38
Elif	SNR	26.29	31.59	29.90
	PSNR	31.34	36.66	34.96
	SSIM	0.70	0.90	0.85
	SNR	18.79	27.04	25.09
	PSNR	23.84	32.14	30.21
	SSIM	0.41	0.81	0.73
	SNR	8.09	20.93	15.60
	PSNR	13.01	26.06	21.21
	SSIM	0.09	0.68	0.43
testImage	SNR	27.32	33.73	30.82
	PSNR	30.30	36.73	33.83
	SSIM	0.75	0.97	0.91
	SNR	19.67	26.20	23.40
	PSNR	22.73	29.29	26.54
	SSIM	0.53	0.87	0.74
	SNR	8.43	16.91	12.22
	PSNR	11.78	20.14	16.11
	SSIM	0.19	0.53	0.33

Table 4.1: Comparison MAD with AA

4.3 Comparison of MAD and Other Methods

In order to test the performance of the MAD method, we compared MAD method with the AA, fast SDD-QL, SRAD, and SAR-BM3D methods which are most popular despeckling methods in the literature where they are described in Section 2.2. AA and fast SDD-QL despeckling methods are variational methods. SRAD is an PDE based anisotropic diffusion method. SAR-BM3D method is NL based despeckling method that provide high performance in noise reduction in regions where similar texture exists in the image.

Ten different textured small images as seen in Figure 4.6 are selected to calculate best parameters of images for different speckle noise level. The best metrics calculated by finding the highest SNR values by changing the each methods parameters in an iterative way and used $SNR_{(J_m^{(n+1)})} < SNR_{(J_m^{(n)})}$ (J_m : Method, n : iteration index) as the stop condition. Best parameters of despeckling methods are calculated for ten images and averaged them for a stable result. Thus, best result is obtained for each method which allows comparison of the methods in a fair way.

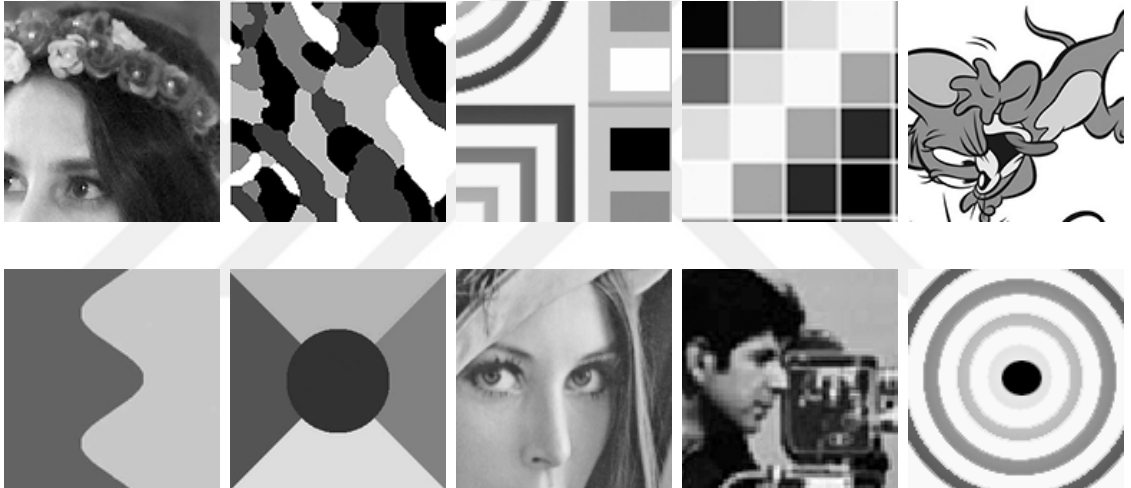


Figure 4.6: Synthetic Images used for Calculating Best Parameters of MAD and Other Methods on Different Speckle Levels

In Table 4.2, results for a synthetic Lena image(383×383 pixels) using the calculated best parameters for each speckle noise level is reported. Best SNR, PSNR, and SSIM values for each case is coloured in grey for the sake of readability. From the table it is shown that, for SNR 10db to 25db SAR-BM3D and for SNR 30db to 45db MAD is the best performing method. SAR-BM3D method benefits from the similarity of patches in the image, so in theory it performs well in textured areas. Although, SAR-BM3D performs good for synthetic and low-resolution images, it does not perform good as expected for the real-world SAR images as shown in Figures 4.8-4.19.

Figure 4.7 shows that variational models (MAD, AA, and fast SDD-QL) are more stable than other methods (SRAD, SAR-BM3D, Enhanced Lee).

		Noise Levels of Despeckling Methods (db)					
Noise Level (db)		MAD	AA	Fast SDD-QL	SRAD	SAR-BM3D	Enhanged Lee
SNR	45.619	45.91	45.88	45.62	25.73	33.90	30.10
PSNR	51.2276	51.52	51.49	51.23	31.55	39.51	35.72
SSIM	0.99215	0.99	0.99	0.99	0.97	0.94	0.91
SNR	40.9734	41.75	41.58	40.97	26.03	33.33	30.06
PSNR	46.5817	47.36	47.19	46.58	31.84	38.94	35.69
SSIM	0.97778	0.98	0.98	0.98	0.97	0.93	0.91
SNR	35.2087	37.24	36.58	36.81	24.74	34.23	29.95
PSNR	40.8165	42.85	42.19	42.42	30.60	39.84	35.58
SSIM	0.92564	0.96	0.95	0.96	0.94	0.94	0.91
SNR	30.4767	33.14	32.70	32.73	24.67	32.83	29.65
PSNR	36.0827	38.75	38.31	38.35	30.52	38.43	35.28
SSIM	0.8264	0.90	0.90	0.89	0.91	0.92	0.89
SNR	25.2227	30.24	28.74	29.72	24.34	31.90	28.71
PSNR	30.8201	35.86	34.37	35.35	30.18	37.50	34.33
SSIM	0.65088	0.87	0.81	0.87	0.87	0.91	0.84
SNR	20.5201	26.82	25.54	27.34	24.19	30.37	26.90
PSNR	26.09	32.44	31.17	32.96	30.00	35.94	32.52
SSIM	0.47157	0.76	0.71	0.80	0.82	0.90	0.76
SNR	15.5348	23.15	22.58	24.48	23.54	26.69	23.76
PSNR	21.0434	28.79	28.24	30.14	29.28	32.20	29.40
SSIM	0.29472	0.62	0.59	0.72	0.75	0.83	0.65
SNR	10.833	20.72	18.28	21.23	21.41	22.22	20.90
PSNR	16.2001	26.44	24.01	27.01	27.04	27.57	26.68
SSIM	0.15691	0.62	0.37	0.65	0.54	0.74	0.60

Table 4.2: Denosided Image Comparison MAD and Other Methods

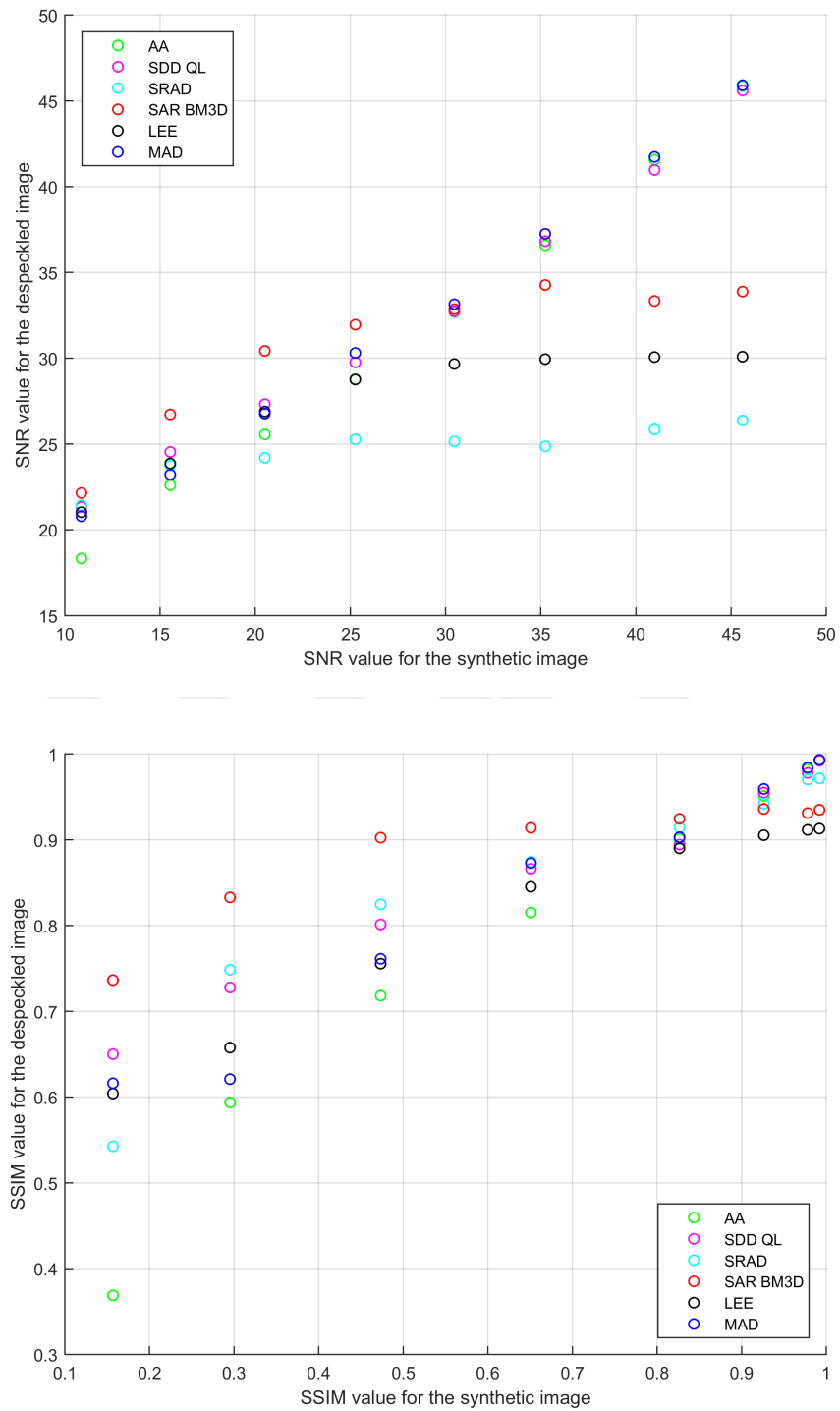


Figure 4.7: Despeckling results of synthetic Lena image using MAD and others

4.4 Experimental Results on Real Dataset

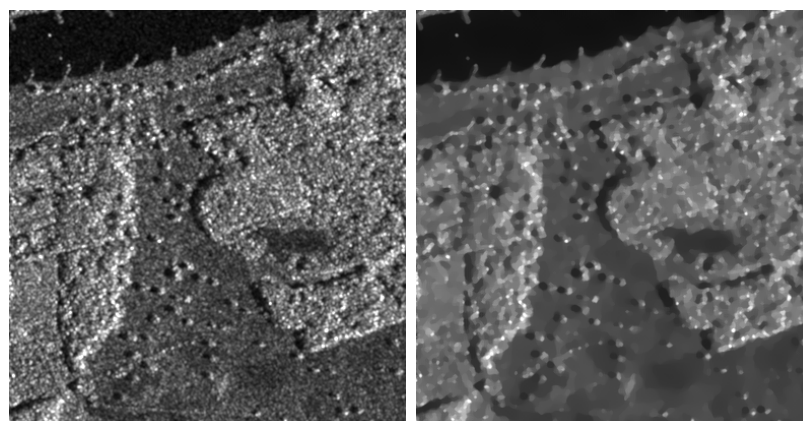
Images from TerraSAR-X satellite platform are used as real-world SAR test images. All of the images are taken from Airbus that has more than 30 years of experience in Earth Observation and Defence Systems (Sarimagesamplegallery, 2018). Airbus provides a wide range of free sample SAR image gallery database for researchers which are acquired from TerraSAR-X satellite. 10 images from different locations having different acquisition protocols (i.e. acquisition mode, polarization mode, resolution, angle of incidence and orbit) which are suitable for various SAR applications are chosen.

To test MAD method and other methods in urban areas, SAR images with different characteristics in Figure 4.10, Figure 4.18, and Figure 4.19 are selected (see for features of images Toronto SAR Image Table A.2, Singapore-2 SAR Image Table A.3, Barcelona SAR Image Table A.1).

For sea and terrestrial zones, SAR images with different characteristics in Figure 4.12 and Figure 4.17 are selected (see for features of images Singapore SAR Image Table A.4, Gulf of Mexico SAR Image Table A.5).

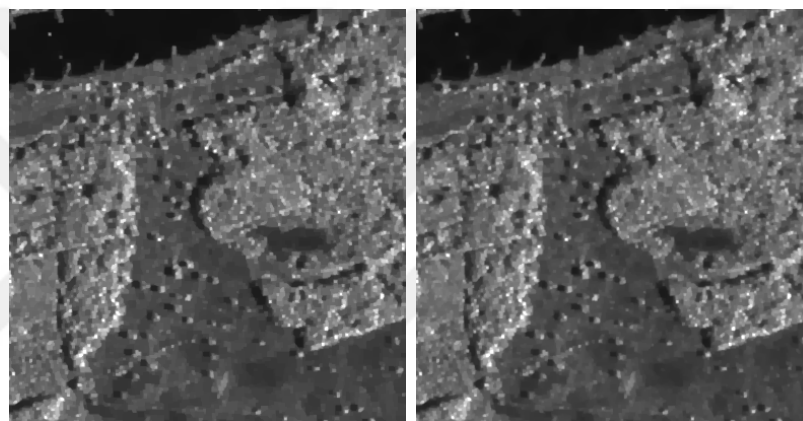
To test performance of the MAD method, it is compared with the AA, fast SDD-QL, SRAD, and SAR-BM3D methods which are popular despeckling methods in the literature as described in Section 2.2.

AA, MAD, and fast SDD-QL method results appear to be very similar to each other for some images since difference is small to observe as shown in Table 4.2 (MAD, AA, and fast SDD-QL have an invisible difference of 1-3 db).



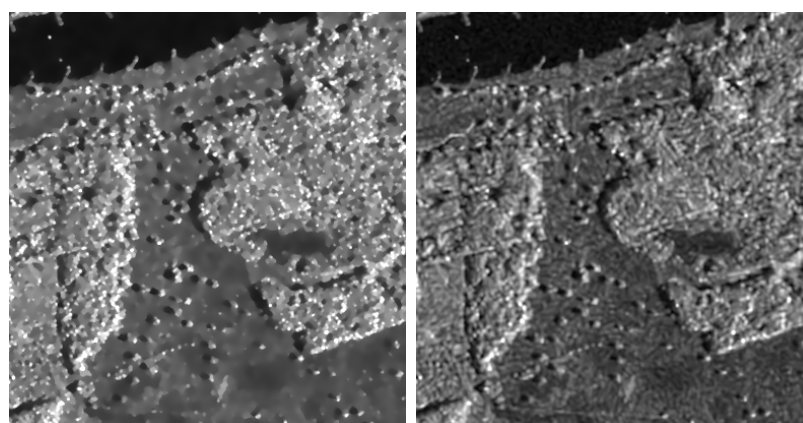
(a) Original SAR Image

(b) AA



(c) Fast SDD-QL

(d) MAD



(e) SRAD

(f) SAR-BM3D

Figure 4.8: MAD and other methods despeckling results on Dessau image (see Table A.8 for image Details)

MAD method and other methods perform well while SAR-BM3D does not perform satisfactorily as we explained the reason before (see Figure 4.8). In order to aid visual observation, a part of despeckled image with $\times 2$ zoom level is used as seen Figure 4.9.

Experiments show that, although SAR-BM3D performs quite good in synthetic images it does not perform well in real-world SAR images, especially if image resolution is high. In order to validate this observation, large set for parameters are tested and SAR-BM3D is only found suitable for limited set of SAR images. One other drawback of SAR-BM3D is its long execution times.

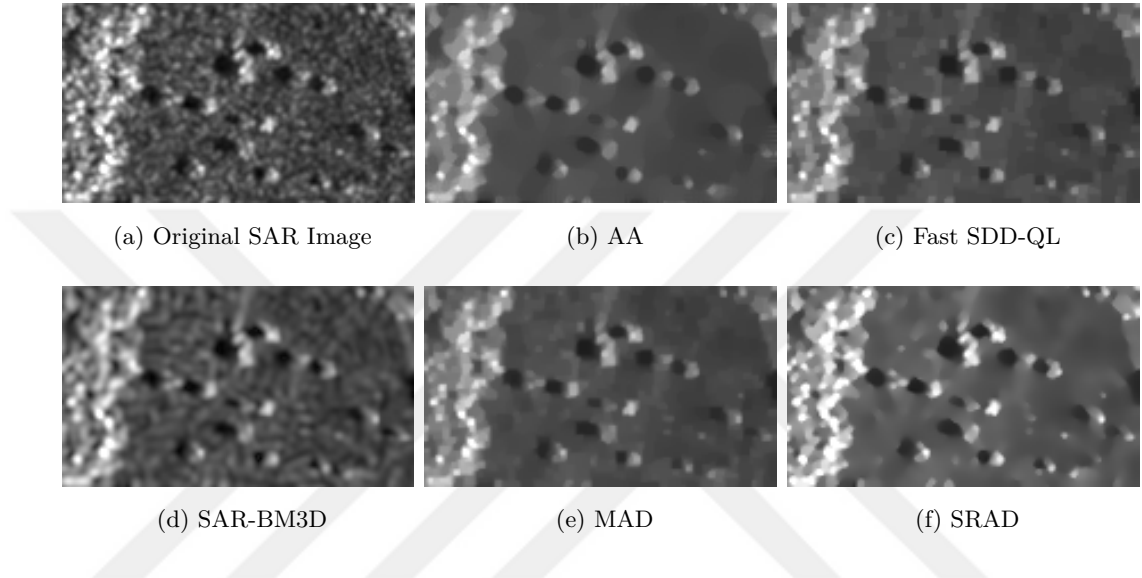


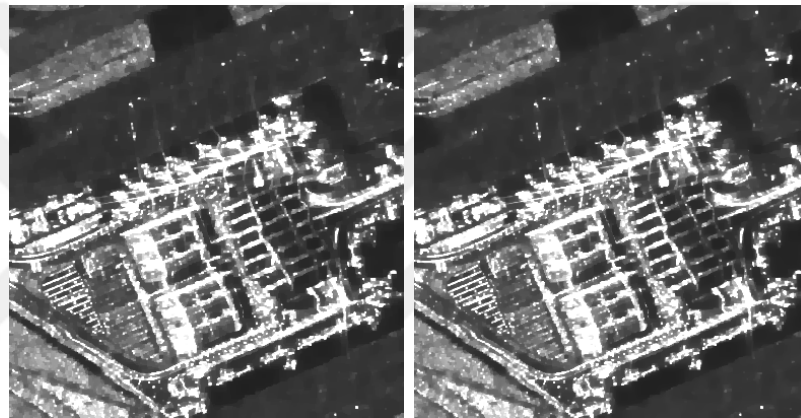
Figure 4.9: Despeckled part of Dessau Image (see Table A.8 for image Details)

In MAD method and fast SDD-QL method, edges and point scatterers are preserved while homogeneous regions are smoothed. However, AA method and SRAD method over-smooth the details. As seen in Figure 4.9, shadow of small hills which are in a form of round, square, or oval are smoothed if AA method and SRAD method are used. In other words, AA method and SRAD method can not preserve edges as much as MAD method can do.



(a) Original SAR Image

(b) AA



(c) Fast SDD-QL

(d) MAD



(e) SRAD

(f) SAR-BM3D

Figure 4.10: MAD and other methods despeckling results on Barcelona image (see Table A.1 for image Details)

In Figure 4.10, MAD method and other methods are compared where they all perform quite well. Therefore, observing the difference among them is quite difficult by eye. So, a part of despeckled image with $\times 3$ zoom level is used as seen in Figure 4.11.

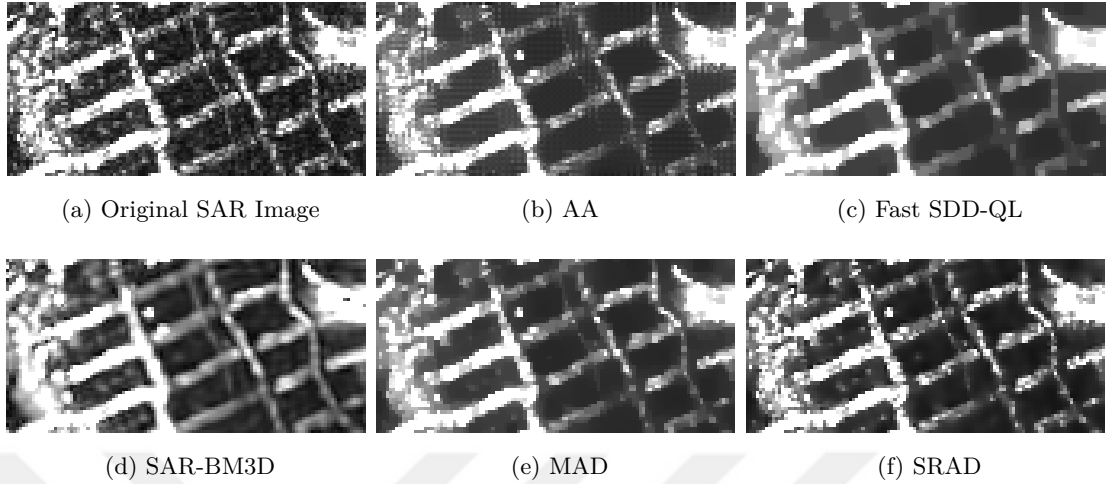


Figure 4.11: Despeckled part of Barcelona Image (see Table A.1 for image Details)

Speckle noise level in Figure 4.10 is in alignment with the speckle noise level intervals where SAR-BM3D is successful. Yet, SAR-BM3D despeckling result has various artifacts such as undesired smoothing on the point scatterers. In Figure 4.11.e, edges and point scatterers are preserved while homogeneous regions are smoothed by MAD method. In Figure 4.11.f edges and point scatterers are preserved but homogeneous regions are not smoothed sufficiently by SRAD method.

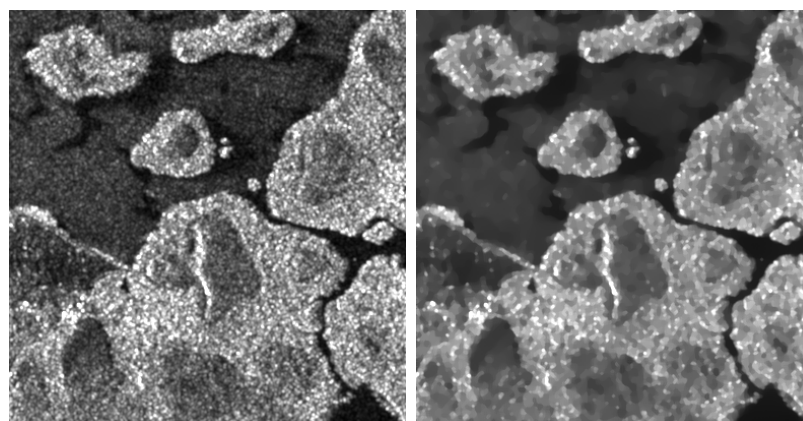
MAD uses an implicit scheme during numerical minimization whereas AA method and SRAD method use an explicit scheme. So, in some results, a dithering artifact become visible, especially for the AA method (see Figure 4.11.b). Conversely, use of implicit scheme in MAD method allows stable and artifact free results. Note that, fast SDD-QL also uses implicit scheme so its results also does not contain dithering artifacts that appear in the results of the AA method.

As seen in Figure 4.12.e, SRAD method also contains similar dithering artifacts like AA method (see Figure 4.11.b). In these examples, SAR-BM3D method also fails while MAD method and fast SDD-QL methods are effective.

Note that, Figure 4.13 and Figure 4.14 are patches taken from the same SAR image. SAR-BM3D method performs well for this image as seen in Figure 4.13. But SAR-BM3D method does not perform well for the image given in Figure 4.14 since it can not find similar patches in Figure 4.14. In short, for these images, SAR-BM3D method preserves edges and point scatterers and it makes small amount of smoothing but this smoothing is not enough to reduce speckle noise effectively.

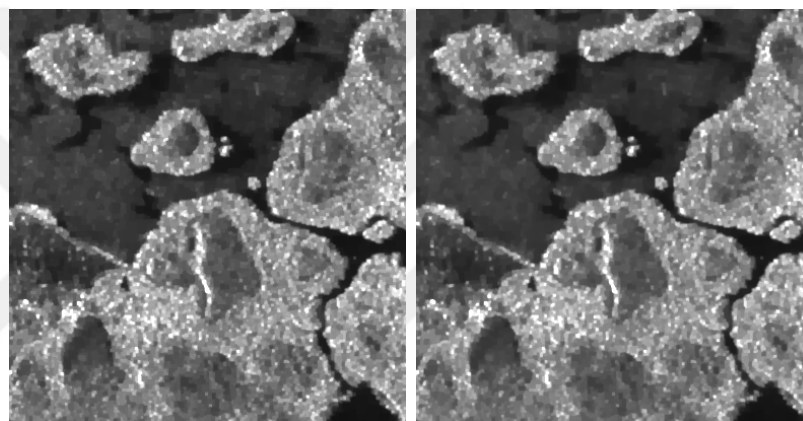
Excluding the SAR-BM3D method, MAD method and other remaining methods have similar despeckling performances as seen in Figure 4.13 and Figure 4.14. Also, MAD method has an effective performance on despeckling as seen in the figures. The Figure 4.15, Figure 4.16, Figure 4.17, Figure 4.18, and Figure 4.19 are used for determining the execution times of the MAD method and other methods.





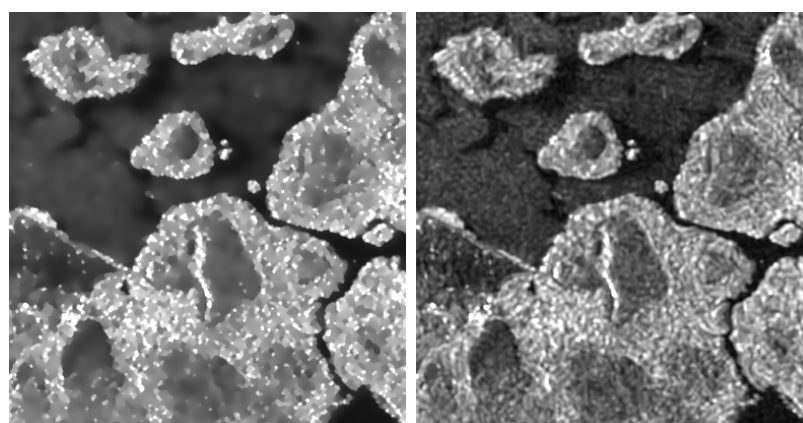
(a) Original SAR Image

(b) AA



(c) Fast SDD-QL

(d) MAD



(e) SRAD

(f) SAR-BM3D

Figure 4.12: MAD and other methods despeckling results on Singapore image (see Table A.4 for image Details)

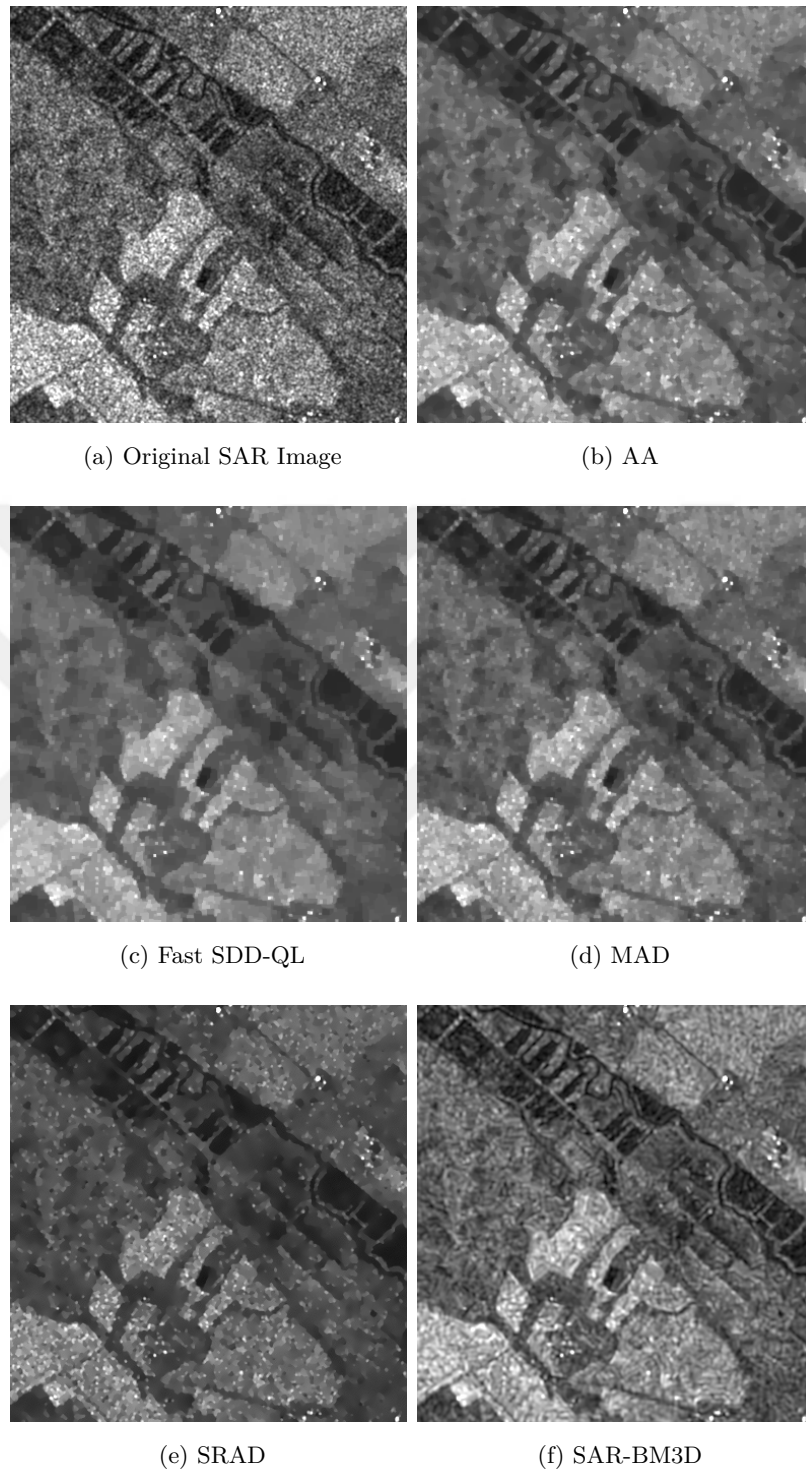


Figure 4.13: MAD and other methods despeckling results on Rügen image (see Table A.9 for image Details)

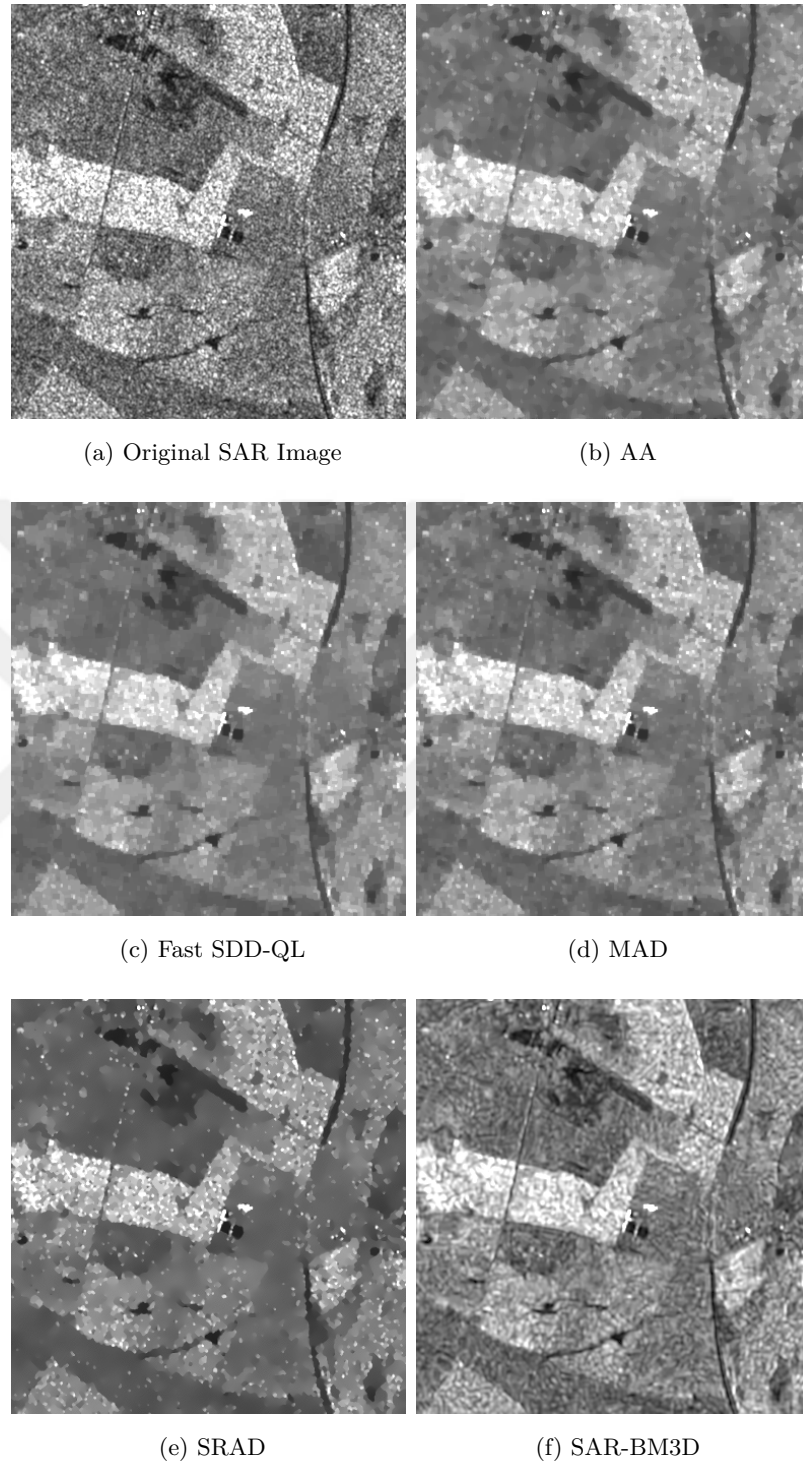
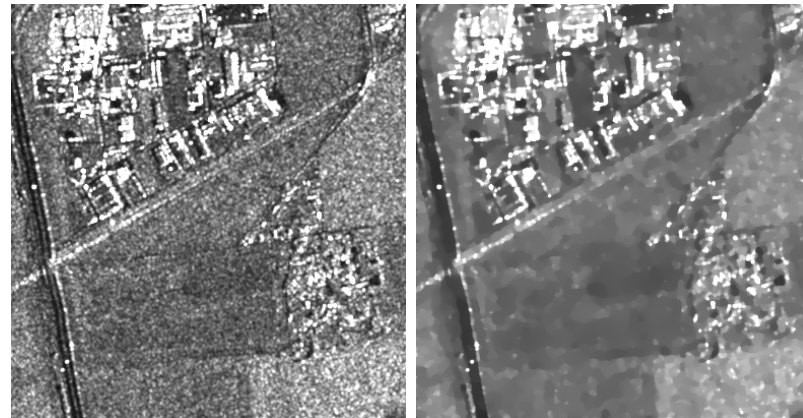
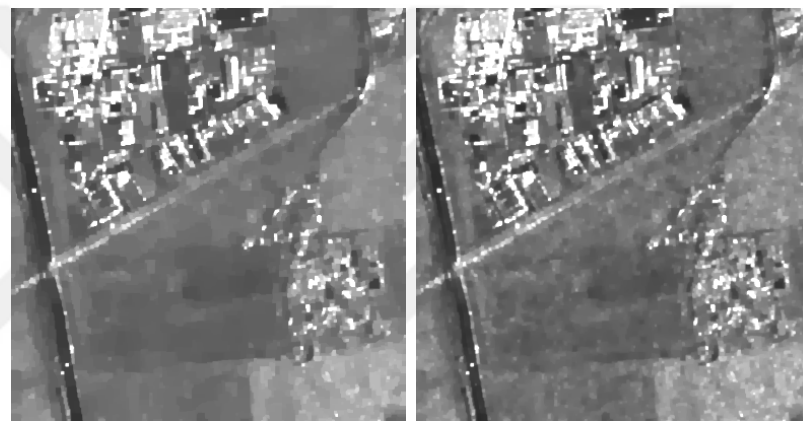


Figure 4.14: MAD and other methods despeckling results on island Rügen image (see Table A.10 for image Details)



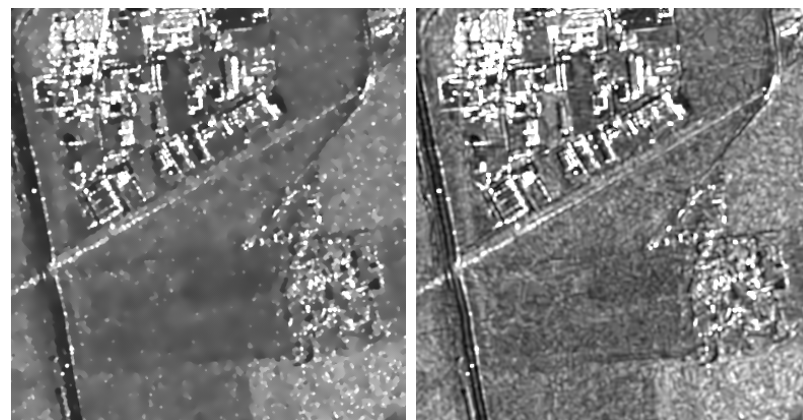
(a) Original SAR Image

(b) AA



(c) Fast SDD-QL

(d) MAD



(e) SRAD

(f) SAR-BM3D

Figure 4.15: MAD and other methods despeckling results on Germany image (see Table A.6 for image Details)

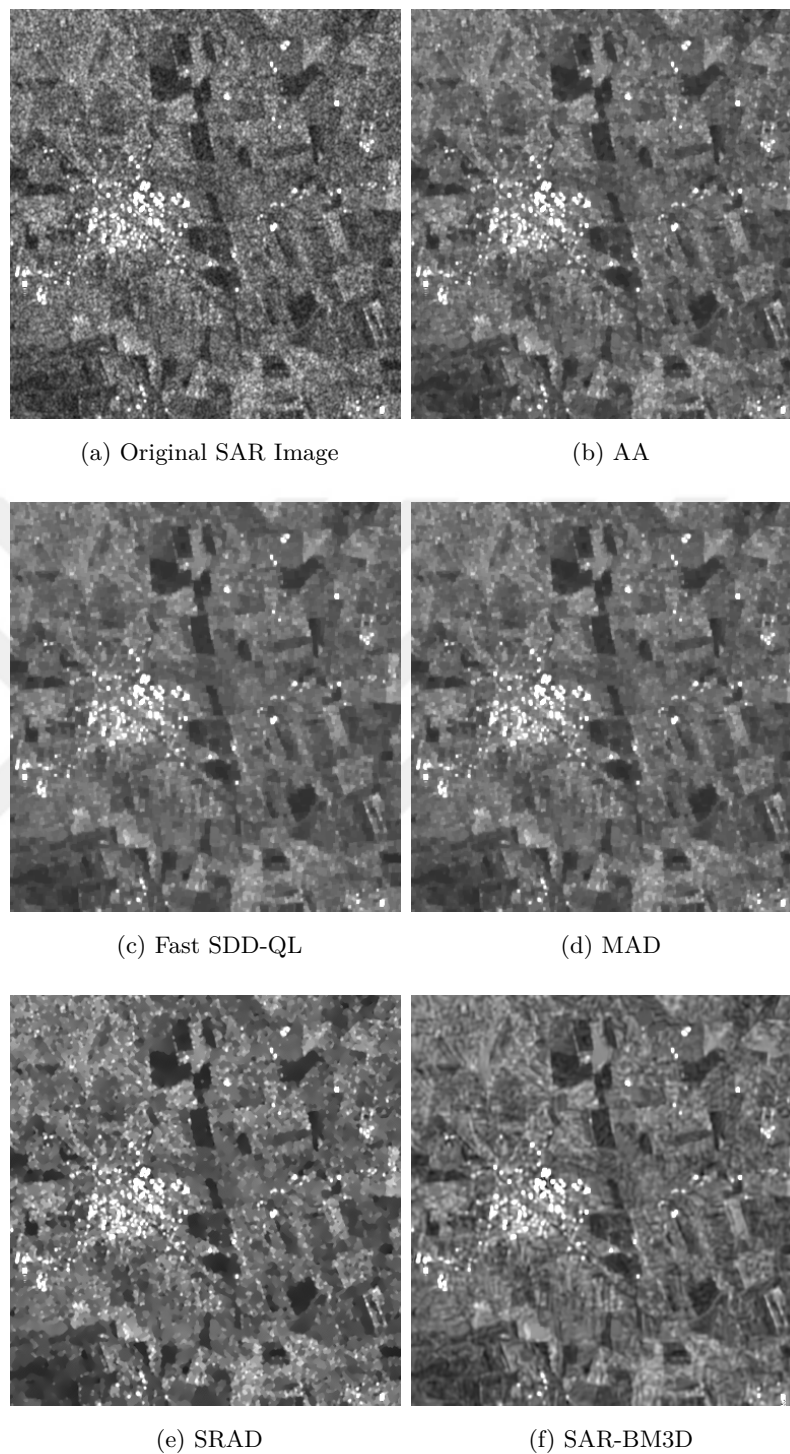
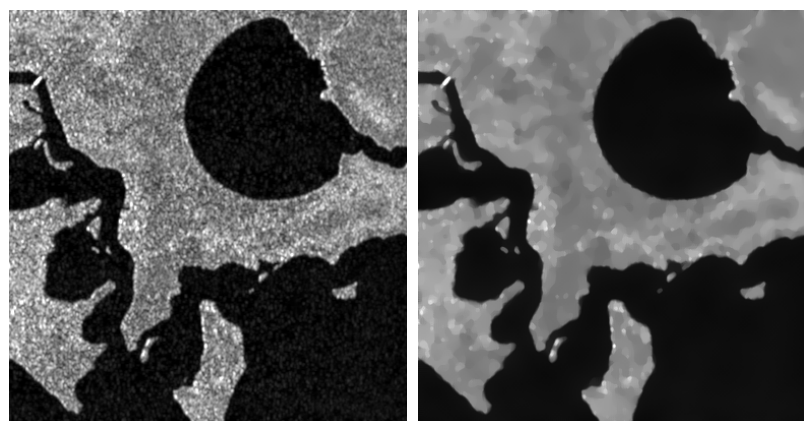
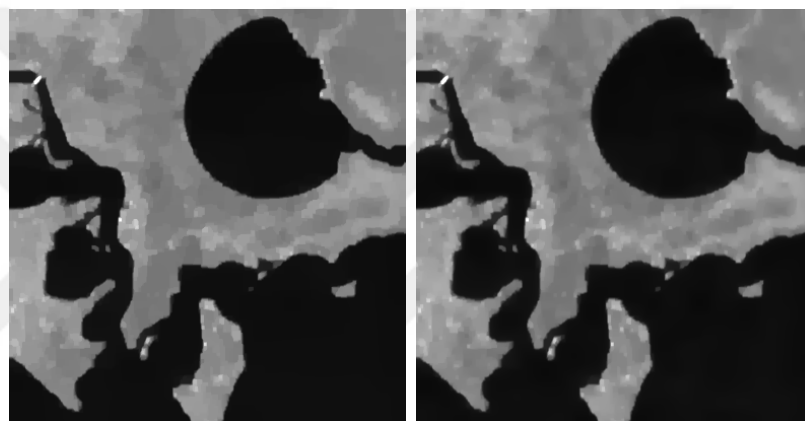


Figure 4.16: MAD and other methods despeckling results on North Sea image (see Table A.7 for image Details)



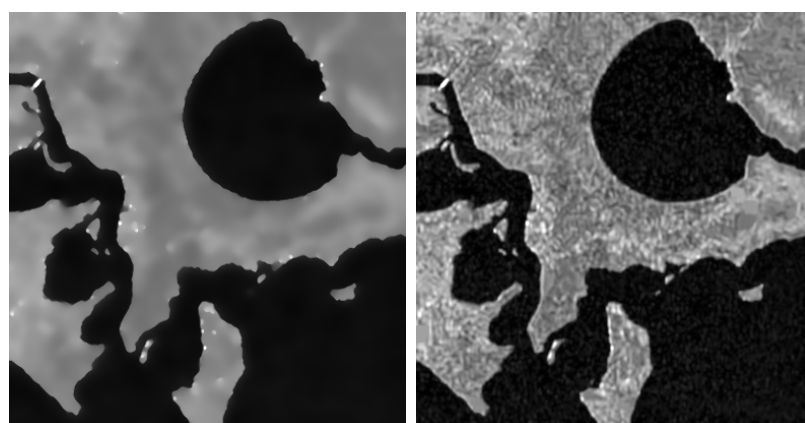
(a) Original SAR Image

(b) AA



(c) Fast SDD-QL

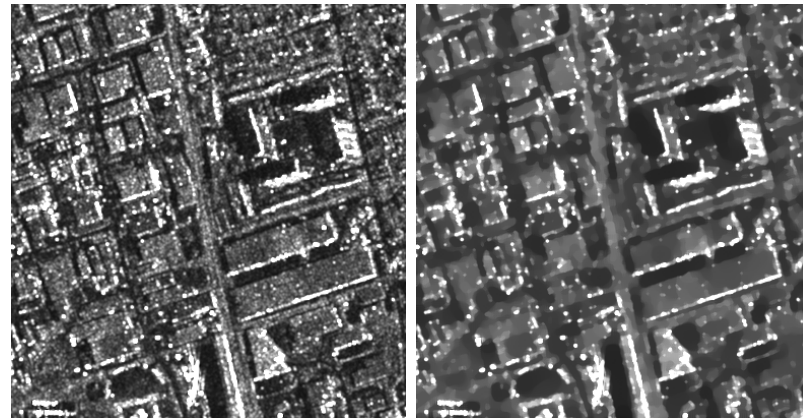
(d) MAD



(e) SRAD

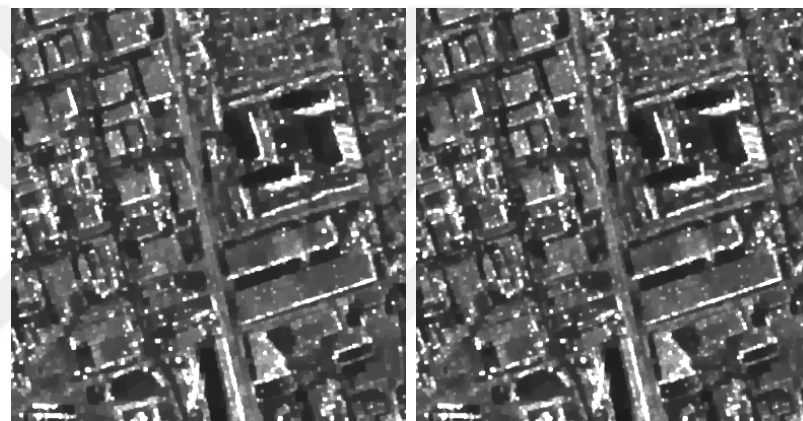
(f) SAR-BM3D

Figure 4.17: MAD and other methods despeckling results on Gulf of Mexico image (see Table A.5 for image Details)



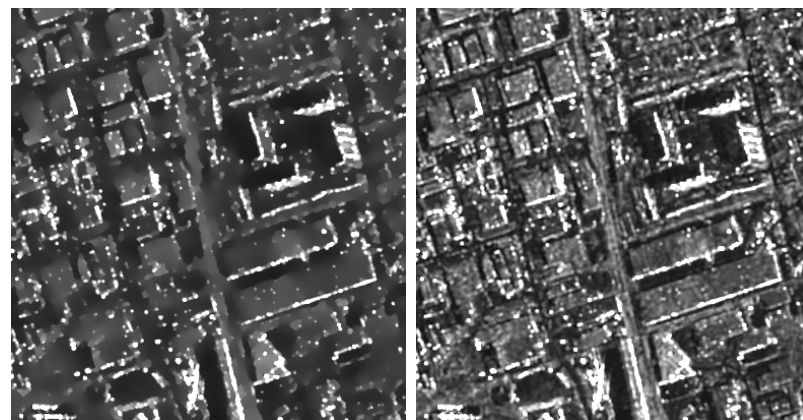
(a) Original SAR Image

(b) AA



(c) Fast SDD-QL

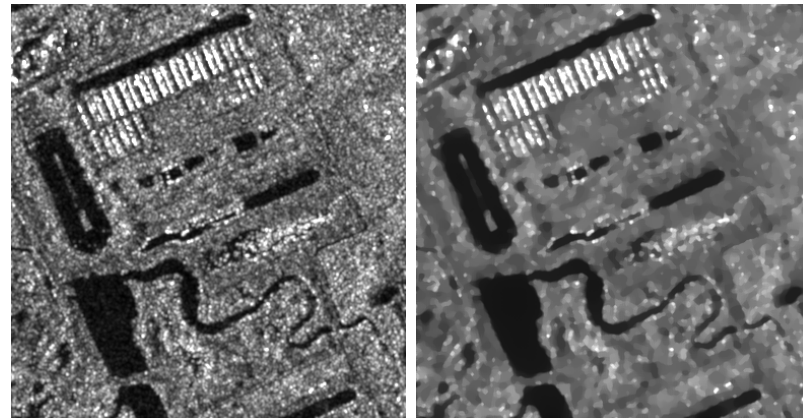
(d) MAD



(e) SRAD

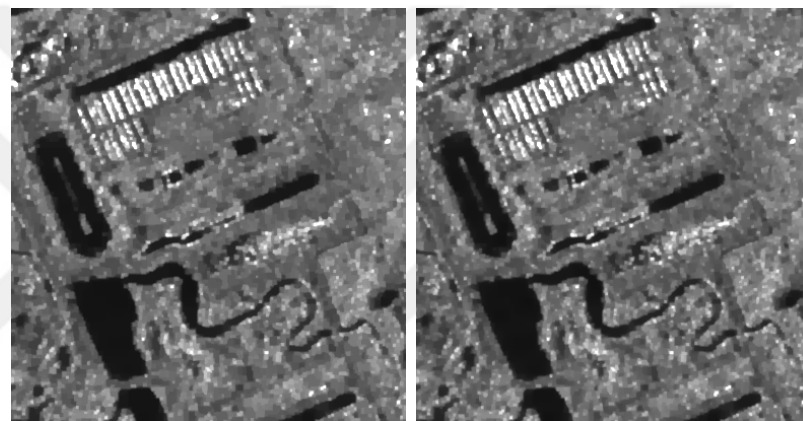
(f) SAR-BM3D

Figure 4.18: MAD and other methods despeckling results on Toronto image (see Table A.2 for image Details)



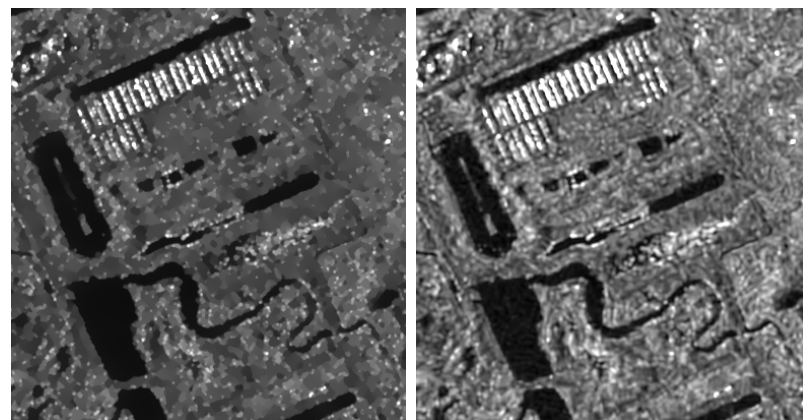
(a) Original SAR Image

(b) AA



(c) SDD-QL

(d) MAD



(e) SRAD

(f) SAR-BM3D

Figure 4.19: MAD and other methods despeckling results on Singapore-2 image (see Table A.3 for image Details)

4.5 Execution Time of MAD and Other Methods Despeckling

Figure 4.20 shows execution time comparison of MAD method and other methods using the ten real-world SAR images that are used in Section 4.4. This experiment is executed using an Intel i5-3210M 2.5GHz CPU running on Windows operating system.

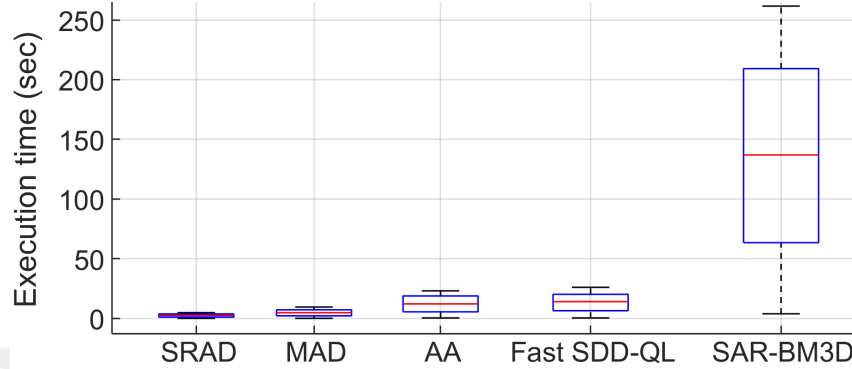


Figure 4.20: Execution times of MAD and other methods

As expected, despeckling time of NL based SAR-BM3D method is very long while other methods has an execution time in the interval no more than 25 seconds. Note that, MAD method is $\times 30$ faster than SAR-BM3D method and $\times 2$ faster than AA and fast SDD-QL methods.

Here, MAD method is the second faster one while SRAD method being the fastest. However, SRAD method does not provide promising despeckling result so its speed becomes irrelevant (see Section 4.4 and Table 4.2).

Relation between obtained despeckling and execution time of despeckling results show that proposed MAD method provides better despeckling performance compared to existing methods in a computationally efficient manner.

CHAPTER 5

SUMMARY AND CONCLUSION

In this thesis, a novel variational SAR image speckle noise reduction (despeckling) method is proposed, namely Multiplicative Additive Despeckling (MAD). Proposed speckle reduction method is constructed as an optimization problem and aims to reduce both multiplicative noise and additive noise simultaneously while preserving image details such as edges and point scatterers. Due to its success in denoising literature, a variational cost function with proper data fidelity terms and a total variation smoothness term is developed. However, proposed cost function is non-convex and also contains a non-differentiable term. Therefore, it has been effectively minimized using convex relaxation and convex optimization methods. Consequently, an efficient and stable numerical minimization scheme is obtained.

Analysis of the proposed MAD method and its parameters is feasible since it is based on minimization of a cost function with a well defined mathematical form that allows use of various techniques of linear algebra and numerical optimization. Thereby, analysis of the proposed cost function, its approximation, and obtained algorithm is presented with its computational and convergence aspects, both theoretically and empirically.

Speckle reduction performance of the proposed method is presented on real-world SAR images and synthetically generated SAR images where proposed method is also compared with other state-of-the-art SAR despeckling methods. Obtained results and comparison studies show that proposed MAD method provides better despeckling performance compared to existing methods in a computationally efficient manner.

In future studies we want to investigate below topics regarding to this thesis:

- Analysis of the MAD with respect to condition number versus time
- Parallel implementation on CPU using OpenMP and on GPU using CUDA
- Developing a scheme for tile based processing for scalability and distributed computing

Bibliography

- Argenti, F. and Alparone, L. (2002). Speckle removal from SAR images in the undecimated wavelet domain. *IEEE Transactions on Geoscience and Remote Sensing*, 40(11):2363–2374.
- Argenti, F., Bianchi, T., and Alparone, L. (2006). Multiresolution map despeckling of SAR images based on locally adaptive generalized gaussian pdf modeling. *IEEE Transactions on Image Processing*, 15(11):3385–3399.
- Argenti, F., Lapini, A., Bianchi, T., and Alparone, L. (2013). A tutorial on speckle reduction in synthetic aperture radar images. *IEEE Geoscience and Remote Sensing Magazine*, 1(3):6–35.
- Ascher, U., Ruuth, S., and Spiteri, R. (1997). Implicit-explicit runge-kutta methods for time-dependent partial differential equations. *Applied Numerical Mathematics*, 25:151–167.
- Aubert, G. and Aujol, J.-F. O. (2008). A variational approach to removing multiplicative noise. *SIAM Journal on Applied Mathematics*, 68(4):925–946.
- Baraff, D. and Witkin, A. (2001). Large Steps in Cloth Simulation. *Proceedings of Siggraph*, 98.
- Barbu, T. (2013). Variational image denoising approach with diffusion porous media flow. *Abstract and Applied Analysis*.
- Baxes, G. A. (1994). *Digital Image Processing: Principles and Applications*. Wiley; 1 Edition.
- Behrooz, A., min Zhou, H., Eftekhari, A., and Adibi, A. (2012). Total variation regularization for 3d reconstruction in fluorescence tomography: Experimental phantom studies. *Applied Optics*, 51:8216–27.
- Bianchi, T., Argenti, F., and Alparone, L. (2008). Segmentation-based map despeckling of SAR images in the undecimated wavelet domain. *IEEE Transactions on Geoscience and Remote Sensing*, 46(9):2728–2742.
- Bioucas-dias, J. M. and Figueiredo, M. A. T. (2010). Multiplicative noise removal using variable splitting and constrained optimization. *IEEE Transactions on Image Processing*, 19(7):1720–1730.
- Boncellet, C. G. (2009). Image noise models. *The Essential Guide To Image Processing*, pages 143–167.
- Brett, P. T. B. and Guida, R. (2012). Geometry-based SAR curvilinear feature selection for damage detection. In *Eusar 2012; 9th European Conference on Synthetic Aperture Radar*, pages 62–65.
- Buades, A., Coll, B., and Morel, J. M. (2005). A review of image denoising algorithms, with a new one. *Multiscale Modeling & Simulation*, 4(2):490–530.
- Chen, Y., Cremers, A. B., and Cao, Z. (2014). A variational change detection method for multitemporal SAR images. *Remote Sensing Letters*, 5.

- Crimmins, T. R. (1985). Geometric filter for speckle reduction. *Applied Optics*, 24:1438.
- Crockett, M. T. (2013). An introduction to synthetic aperture radar: A high-resolution alternative to optical imaging. *Utah Space Grant Consortium*.
- Dabov, K., Foi, A., Katkovnik, V., and Egiazarian, K. (2007). Image denoising by sparse 3-d transform-domain collaborative filtering. *IEEE Transactions on Image Processing*, 16(8):2080–2095.
- Deka, B. and Bora, P. K. (2013). Removal of correlated speckle noise using sparse and overcomplete representations. *Biomedical Signal Processing and Control*, 8:520 – 533.
- Deledalle, C. A., Denis, L., and Tupin, F. (2009). Iterative weighted maximum likelihood denoising with probabilistic patch-based weights. *IEEE Transactions on Image Processing*, 18(12):2661–2672.
- Deledalle, C.-A., Denis, L., Tupin, F., Reigber, A., and Jäger, M. (2015). Nl-sar: A unified nonlocal framework for resolution-preserving (pol)(in)SAR denoising. *IEEE Transactions on Geoscience and Remote Sensing*, 53(4):2021–2038.
- Desbrun, M., Schroder, P., and Barr, A. (1999). Interactive animation of structured deformable objects. In *Proceedings of The 1999 Conference on Graphics Interface '99*, pages 1–8.
- Do, M. N. and Vetterli, M. (2005). The contourlet transform: An efficient directional multiresolution image representation. *IEEE Transactions on Image Processing*, 14(12):2091–2106.
- Duff, I. S., Erisma, A. M., and Reid, J. K. (1989). *Direct Methods for Sparse Matrices*. Clarendon Press.
- Durand, S., Fadili, J., and Nikolova, M. (2010). Multiplicative noise removal using 11 fidelity on frame coefficients. *Journal of Mathematical Imaging and Vision*, 36(3):201–226.
- Elad, M. and Aharon, M. (2006). Image denoising via sparse and redundant representations over learned dictionaries. *IEEE Transactions on Image Processing*, 15(12):3736–3745.
- Erbay, A. Y. (2014). Farklı Öellikleriyle yeni nesil dünya gözlem uyduları ve kullanım alanları. Technical Report 2, 5. Uzaktan Algıama- Cbs Sempozyumu, Nik Sistem - Nik İnşaat Tic. Ltd.şti./ Istanbul. (Uzal-cbs 2014).
- Farooque, M. A. and Rohankar, J. S. (2013). Survey on various noises and techniques for denoising the color image. *International Journal of Application Or Innovation in Engineering and Management (Ijaiem)*, 2(3):815.
- Ferretti, A., Monti-guarnieri, A., Prati, C., Rocca, F., and Massonet, D. (2007). In-sar principles - guidelines for SAR interferometry processing and interpretation. *Esa Training Manual*, 19.
- FirstSAR (2018). First SAR image. <https://en.wikipedia.org/wiki/file:firstsarimage.jpg>". Accessed: 2018-12-04.

- Foi, A. and Boracchi, G. (2016). Foveated nonlocal self-similarity. *International Journal of Computer Vision*.
- Foucher, S. (2008). Sar image filtering via learned dictionaries and sparse representations. In *Igarss 2008 - 2008 IEEE International Geoscience and Remote Sensing Symposium*, volume 1, pages I-229–i-232.
- Foucher, S., Benie, G. B., and Boucher, J. . (2001). Multiscale map filtering of SAR images. *IEEE Transactions on Image Processing*, 10(1):49–60.
- Franceschetti, G. and Lanari, R. (1999). *Synthetic Aperture Radar Processing*. Crc Press.
- Frost, V. S., Stiles, J. A., Shanmugan, K. S., and Holtzman, J. C. (1982). A model for radar images and its application to adaptive digital filtering of multiplicative noise. *IEEE Transactions on Pattern Analysis and Machine Intelligence*, Pami-4(2):157–166.
- Gagnon, L. and Jouan, A. (1997). Speckle filtering of SAR images - a comparative study between complex-wavelet-based and standard filters. *Proceedings of Spie - The International Society for Optical Engineering*, 3169.
- Gao, Q., Zhao, Y., and Lu, Y. (2008). Despeckling SAR images using stationary wavelet transform combining with directional filter banks. *Applied Mathematics and Computation*, 205:517–524.
- Gokturk (2018). Gökürk-3. "[Http://aviationweek.com/blog/turkey-begin-launch-system-gokturk-3-negotiations](http://aviationweek.com/blog/turkey-begin-launch-system-gokturk-3-negotiations)". Accessed: 2018-09-21.
- Gonzalez, R. C. and Woods, R. E. (2002). *Digital Image Processing*, volume 2. Prentice Hall.
- Goodman, J. W. (1976). Some fundamental properties of speckle*. *J. Opt. Soc. Am.*, 66(11):1145–1150.
- Hao, Y., Feng, X., and Xu, J. (2012). Multiplicative noise removal via sparse and redundant representations over learned dictionaries and total variation. *Signal Processing*, 92(6):1536 – 1549.
- Haralick, R. M. and Shapiro, L. G. (1992). *Computer and Robot Vision*. Addison-wesley Longman Publishing Co., Inc., Boston, Ma, Usa, 1st edition.
- Hou, B., Zhang, X., Bu, X., and Feng, H. (2012). SAR image despeckling based on nonsubsampling shearlet transform. *IEEE Journal of Selected Topics in Applied Earth Observations and Remote Sensing*, 5(3):809–823.
- Huang, Y., Genderen, V., and L., J. (1996). Evaluation of several speckle filtering techniques for ers-1 & 2 imagery. *International Archives of Photogrammetry And Remote Sensing*.
- Huang, Y., Moisan, L., Ng, M., and Zeng, T. (2012). Multiplicative noise removal via a learned dictionary. *IEEE Trans Image Process*.
- Huang, Y.-M., Ng, M. K., and Wen, Y.-W. (2009). A new total variation method for multiplicative noise removal. *SIAM Journal on Imaging Sciences*, 2(1):Pp. 20–40.

- Implicit (2019). Implicit versus explicit. "[Http://hplgit.github.io/num-methods-for-pdes/doc/pub/vib/html/fig-vib/vib_theta_1_pp.png](http://hplgit.github.io/num-methods-for-pdes/doc/pub/vib/html/fig-vib/vib_theta_1_pp.png). Accessed: 2019.02.23.
- Kent, S., Uçan, O. N., and Ensari, T. (May 25-27,2004). Speckle reduction of synthetic aperture radar images using wavelet filtering. *in Astrium Eusar 2004 Proceedings, 5th European Conference on Synthetic Aperture Radar*.
- Kuan, D. T., Sawchuk, A. A., Strand, T. C., and Chavel, P. (1985). Adaptive noise smoothing filter for images with signal-dependent noise. *IEEE Transactions on Pattern Analysis and Machine Intelligence*, Pami-7(2):165–177.
- Kupidura, P. (2016). Comparison of filters dedicated to speckle suppression in SAR images. *Isprs - International Archives of The Photogrammetry, Remote Sensing and Spatial Information Sciences*, Xli-b7:269–276.
- Kuttiyannan, D. T., Manavalan, R., and Aroquiaraj, L. (2008). Removal of speckle noise from ultrasound medical image based on special filters: Comparative study. *Icgst Gvip*, 9.
- Lee, J. S. (1981). Speckle analysis and smoothing of synthetic aperture radar images. *Computer Graphics and Image Processing*, 17:24–32.
- Lee, J. S. (1983). A simple speckle smoothing algorithm for synthetic aperture radar images. *IEEE Transactions on Systems, Man, and Cybernetics*, Smc-13(1):85–89.
- Lee, J. S. (1985). Speckle suppression and analysis for synthetic aperture radar images. *Optical Engineering*, 25:25 – 25 – 8.
- Lee, J. S., hung Wen, J., Ainsworth, T. L., shan Chen, K., and Chen, A. J. (2009). Improved sigma filter for speckle filtering of SAR imagery. *IEEE Trans. Geosci. Remote Sens.*, 47:202 – 213.
- Lee, J. S., Jurkevich, L., Dewaele, P., Wambacq, P., and Oosterlinck, A. (1994). Speckle filtering of synthetic aperture radar images: A review. *Remote Sensing Reviews*, 8(4):313–340.
- Lee, J. S. and Pottier, E. (2009). *Polarimetric Radar Imaging*, volume 2. Crc Press.
- Lewis, H. (1998). Principle and applications of imaging radar, volume 2 of manual of remote sensing. *J.wiley and Sons*, Third Edition.
- Li, Y., Gong, H., Feng, D., and Zhang, Y. (2011). An adaptive method of speckle reduction and feature enhancement for SAR images based on curvelet transform and particle swarm optimization. *IEEE Transactions on Geoscience and Remote Sensing*, 49(8):3105–3116.
- li You, Y., Xu, W., Tannenbaum, A., and Kaveh, M. (1996). Behavioral analysis of anisotropic diffusion in image processing. *IEEE Transactions on Image Processing*, 5(11):1539–1553.
- Liu, C., Szeliski, R., Kang, S. B., Zitnick, C. L., and Freeman, W. T. (2008). Automatic estimation and removal of noise from a single image. *IEEE Transactions on Pattern Analysis and Machine Intelligence*, 30(2):299–314.

- Liu, C. and Zhu, S. (2013). A convex relaxation method for computing exact global solutions for multiplicative noise removal. *Journal of Computational and Applied Mathematics*, 238:144 – 155.
- Lopes, A. and Bruniquel, J. (1976). Multivariate optimal speckle reduction in SAR imagery. *International Journal of Remote Sensing*, 18.
- Lopes, A., Touzi, R., and Nezry, E. (1990). Adaptive speckle filters and scene heterogeneity. *IEEE Transactions on Geoscience and Remote Sensing*, 28(6):992–1000.
- Lu, B., Zhang, L., and Xing, F. (2010). SAR speckle reduction based on nonlocal means method. In *2010 Second International Conference on Computer Modeling and Simulation*, volume 2, pages 156–159.
- Ma, L., Ma, H., and Liu, L. (2015/01). Speckle noise reduction in sar image based on k-svd. In *2015 International Symposium on Computers Informatics*. Atlantis Press.
- Mansourpour, M., Rajabi, M. A., and Blais, R. (2006). Effects and performance of speckle noise reduction filters on active radar and SAR images. *Proc. Isprs*.
- Mascarenhas, N. (1997). An overview of speckle noise filtering in SAR images. *Image Processing Techniques, First Latino-american Seminar on Radar Remote Sensing*, 407:71.
- Moreira, A., Prats-iraola, P., Younis, M., Krieger, G., Hajnsek, I., and Papathanassiou, K. P. (2013). A tutorial on synthetic aperture radar. *IEEE Geoscience and Remote Sensing Magazine*, 1(1):6–43.
- mSAR (2018). M-sar. "https://www.aselsan.com.tr/tr-tr/basin-odasi/brosurler/radar-sistemleri/m-sar_tr.pdf". Accessed: 2018-11-30.
- Munson, D. C. and Visentin, R. L. (1989). A signal processing view of strip-mapping synthetic aperture radar. *IEEE Transactions on Acoustics, Speech, and Signal Processing*, 37(12):2131–2147.
- Mythili, C. and Kavitha, V. (2011). Efficient technique for color image noise reduction. *The Research Bulletin of Jordan ACM – ISWSA, Vol. 11 (I I I), 11 (I I I)*:41–44.
- Nar, F. (2018a). SAR image despeckling using quadratic-linear approximated ℓ_1 norm. *Electronics Letters*, 54(6):387–389.
- Nar, F. (2018b). SAR Image despeckling using quadratic linear approximated ℓ_1 norm. *Electronics Letters*, 54(6):387–389.
- Nar, F. and Atasoy, F. (2018). Fast quadratic-linear approximated L_1 -norm for SAR image despeckling. In *International Conference on Advanced Technologies, Computer Engineering and Science*.
- Nocedal, J. and Wright, S. J. (2006). *Numerical Optimization*. Springer.
- OilSpil (2018). Maritime surveillance. "<https://sentinel.esa.int/web/sentinel/user-guides/sentinel-1-sar/applications/maritime-monitoring>". Accessed: 2019-04-09.

- OldSAR (2018). Old SAR image. "[Http://www.mdaus.com/assets/site_18/images/services/sar%20text%20image_vws.png](http://www.mdaus.com/assets/site_18/images/services/sar%20text%20image_vws.png)". Accessed: 2018-12-04.
- Osher, S., Paragios, N., Rudin, L., and I. Lions, P. (2003). Multiplicative denoising and deblurring: Theory and algorithms, in geometric level set methods in imaging. *IEEE Geoscience and Remote Sensing Magazine*, pages 103–119.
- Ozcan, C., Sen, B., and Nar, F. (2016). Sparsity-driven despeckling for SAR images. *IEEE Geoscience and Remote Sensing Letters*, 13(1):115–119.
- Parrilli, S., Poderico, M., Angelino, C. V., and Verdoliva, L. (2012). A nonlocal SAR image denoising algorithm based on lmmse wavelet shrinkage. *IEEE Transactions on Geoscience and Remote Sensing*, 50(2):606–616.
- Perona, P. and Malik, J. (1987). Scale-space and edge detection using anisotropic diffusion. *Proc. of IEEE Computer Society Workshop on Computer Vision*, pages 16–22.
- Perona, P. and Malik, J. (1988). A network for multiscale image segmentation. *Proc. IEEE Int. Symp. Circuits and Systems*, pages 2565–2568.
- Perona, P. and Malik, J. (1990). Scale-space and edge detection using anisotropic diffusion. *IEEE Transactions on Pattern Analysis and Machine Intelligence*, 12(7).
- Pranali A. Hatwar, d. H. R. K. (2014). Analysis of speckle noise reduction in synthetic aperture radar images. *International Journal of Engineering Research & Technology (Ijert)*, 4(3):6–35.
- RadarOptical (2018). Radar vs. optical image. "http://www.newsecuritylearning.com/images/stories/feature/e05_2011/image005.png". [accessed: 2018-11-30].
- RAR (2018). Real aperture radar (RAR). "[Http://www.geo.uzh.ch/~fpaul/sar_theory.html](http://www.geo.uzh.ch/~fpaul/sar_theory.html)". Accessed: 2019-04-08.
- Rarvssar (2018). Relation between RAR and SAR. "[Http://wtlab.iis.u-tokyo.ac.jp/wataru/lecture/rsgis/rsnote/cp4/4-3-1.gif](http://wtlab.iis.u-tokyo.ac.jp/wataru/lecture/rsgis/rsnote/cp4/4-3-1.gif)". Accessed: 2019-04-09.
- Rehman, A. and Wang, Z. (2012). Reduced-reference image quality assessment by structural similarity estimation. *IEEE Transactions on Image Processing*, 21(8):3378–3389.
- Richards, J. A. (2009). *Remote Sensing With Imaging Radar*. Springer.
- Routray, S., Ray, A., and Mishra, C. (2016). Speckle noise removal in SAR images based on sparse coding by dictionary learning and collaborative filtering. In *International Journal of Engineering Research & Technology (Ijert)*.
- Rudin, L. I., Osher, S., and Fatemi, E. (1992). Nonlinear total variation based noise removal algorithms. *Physica D: Nonlinear Phenomena*, 60(1):259 – 268.
- Samuel, W., candleless Walt, M., Christopher, J., and Jackson, R. (2004). Chapter 1 . Principles of Synthetic Aperture Radar. In *SAR Marine User's Manual*.

- SARHistory (2018). Current and future SAR satellites. "<https://www.unavco.org/instrumentation/geophysical/imaging/sar-satellites/sar-satellites.html>". Accessed: 2019-04-09.
- Sarimagesamplegallery (2018). Airbus image sample gallery. "<https://www.intelligence-airbusds.com/en/8262-sample-imagery>". Accessed: 2019-04-02.
- Sarkka, S. (2013). *Bayesian Filtering and Smoothing*. Bayesian Filtering and Smoothing. Cambridge University Press.
- SARPER (2018). Sarper. "https://www.aselsan.com.tr/tr-tr/basin-odasi/brosurler/radar-sistemleri/sarper_tr.pdf". Accessed: 2018-11-30.
- SarSatellites (2018). Synthetic aperture radar (SAR) satellites. "<https://www.unavco.org/instrumentation/geophysical/imaging/sar-satellites/sar-satellites.html>". Accessed: 2019-04-08.
- Shi, Z. and Fung, K. (1994). A comparison of digital speckle filters. *Surface and Atmospheric Remote Sensing: Technologies, Data Analysis and Interpretation*, 2124:2129 – 2133 Vol.4.
- Soganlui, A. and Cetin, M. (2014). Dictionary learning for sparsity-driven SAR image reconstruction. *IEEE International Conference on Image Processing (Icip)*, pages 1693–1697.
- Solbo, S. and Eltoft, T. (2004). Homomorphic wavelet-based statistical despeckling of SAR images. *IEEE Transactions on Geoscience and Remote Sensing*, 42(4):711–721.
- Spaceborne (2018). Exploring the benefits of active vs. passive spaceborne systems. "<https://eijournal.com/print/articles/exploring-the-benefits-of-active-vs-passive-spaceborne-systems>". Accessed: 2018-11-30.
- Strang, G. (2016). *Introduction To Linear Algebra*. Wellesley - Cambridge Pres.
- Stroebel, L. and Zakia, R. D. (1995). *Polarimetric Radar Imaging*. Crc Press.
- Tasdizen, T. (2009). Principal neighborhood dictionaries for nonlocal means image denoising. *IEEE Transactions on Image Processing*, 18(12):2649–2660.
- Wang, Z. and Bovik, A. C. (2002). A universal image quality index. *IEEE Signal Processing Letters*, 9(3):81–84.
- Wang, Z., Bovik, A. C., Sheikh, H. R., and Simoncelli, E. P. (2004). Image quality assessment: From error visibility to structural similarity. *IEEE Transactions on Image Processing*, 13(4):600–612.
- Wicaksono, S. A., Bayuaji, L., Sze, L. T., Lateh, H., and Zain, J. M. (2016). Comparison of various speckle noise reduction filters on synthetic aperture radar image. *International Journal of Applied Engineering Research*, 11(15):8760–8767.
- WikipediaSAR (2018). Synthetic-aperture radar. https://en.wikipedia.org/wiki/synthetic-aperture_radar". Accessed: 2018-12-04.

- Wiley, C. A. (1985). Synthetic aperture radars - a paradigm for technology evolution. *IEEE Trans. Aerosp. Electron. Syst*, 21.
- Xu, L., Yan, Q., Xia, Y., and Jia, J. (2012). Structure extraction from texture via relative total variation. *Acm Transactions on Graphics (Tog)*, 31.
- Yin, L., Yang, R., Gabbouj, M., and Neuvo, Y. (1996). Weighted median filters: A tutorial. *Circuits and Systems I: Analog and Digital Signal Processing, IEEE Transactions on*, 43:157 – 192.
- Yu, Y. and Acton, S. T. (2002). Speckle reducing anisotropic diffusion. *IEEE Transactions on Image Processing*, 11(11):1260–1270.
- Zhong, S. and Cherkassky, V. (2000). Image denoising using wavelet thresholding and model selection. In *Proceedings 2000 International Conference on Image Processing (Cat. No.00ch37101)*, volume 3, pages 262–265 Vol.3.
- Zhuang, Y., Liu, X., Nguyen, T., He, Q., and Hong, S. (2013). Global remote sensing research trends during 1991-2010: A bibliometric analysis. *Scientometrics*, 96:203–19.
- Özcan, C., Şen, B., and Nar, F. (2014). Gpu efficient SAR image despeckling using mixed norms. *Proc.spie*, 9247:9247 – 9247 – 13.
- Özdemir, C. (2012). *Inverse Synthetic Aperture Radar Imaging With Matlab Algorithms*. John Wiley & Sons.

Appendix A

REAL-WORLD SAR IMAGE DATASET



Location : Barcelona, Spain
 Date : 05/15/2011
 Band : X
 Acquisition mode : StripMap
 Polarization channel : HH
 Polarization mode : Single
 Resolution : 3 m
 Orbit : Ascending
 Angle of incidence : 35.2
 Platform : Terrasar

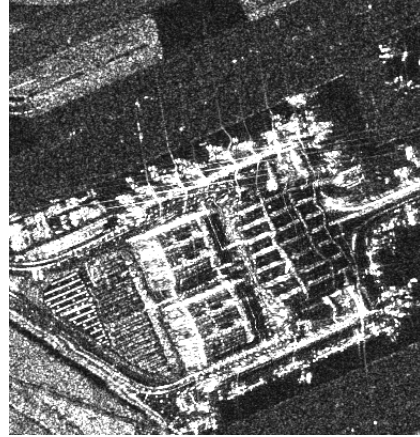


Table A.1: Barcelona SAR Image Information

Location : Toronto, Canada
 Date : 03/03/2008
 Band : X
 Acquisition mode : High Resolution SpotLight
 Polarization channel : HH
 Polarization mode : Single
 Resolution : 1 m
 Orbit : Ascending
 Angle of incidence : 48.8
 Platform : Terrasar



Table A.2: Toronto SAR Image Information

Location : Singapore
 Date : 05/17/2010
 Band : X
 Acquisition mode : StripMap
 Polarization channel : HH
 Polarization mode : Single
 Resolution : 3 m
 Orbit : Ascending
 Angle of incidence : 23.93
 Platform : Terrasar

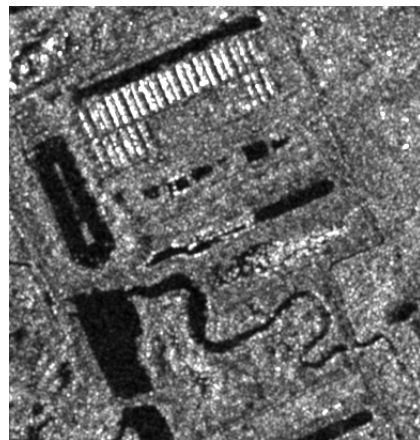


Table A.3: Singapore-2 SAR Image Information

Location : Singapore
 Date : 05/17/2010
 Band : X
 Acquisition mode : StripMap
 Polarization channel : HH
 Polarization mode : Single
 Resolution : 3 m
 Orbit : Ascending
 Angle of incidence : 23.93
 Platform : Terrasar

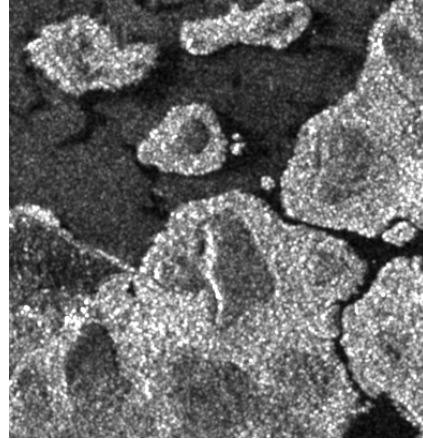


Table A.4: Singapore SAR Image Information

Location : Gulf of Mexico, Mexico
 Date : 05/19/2014
 Band : X
 Acquisition mode : Wide ScanSAR
 Polarization channel : VV
 Polarization mode : Single
 Resolution : 40 m
 Orbit : Ascending
 Angle of incidence : 33.75
 Platform : Terrasar

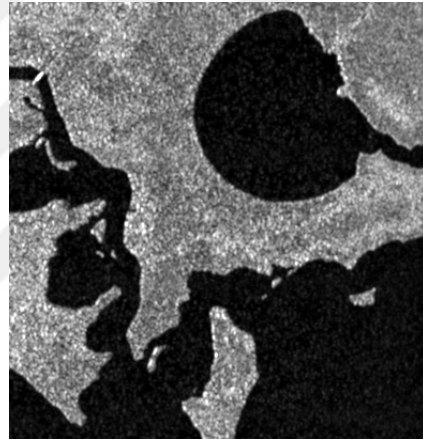


Table A.5: Gulf of Mexico SAR Image Information

Location : Dessau, Germany
 Date : 07/22/2010 - 09/04/2010
 Band : X
 Acquisition mode : StripMap
 Polarization channel : HH
 Polarization mode : Single
 Resolution : 3 m
 Orbit : Descending
 Angle of incidence : 41.10
 Platform : Terrasar



Table A.6: Germany SAR Image Information

Location : North Sea
 Date : 07/25/2013
 Band : X
 Acquisition mode : Wide ScanSAR
 Polarization channel : VV
 Polarization mode : Single
 Resolution : 34.9 m
 Orbit : Descending
 Angle of incidence : 42.3
 Platform : Terrasar

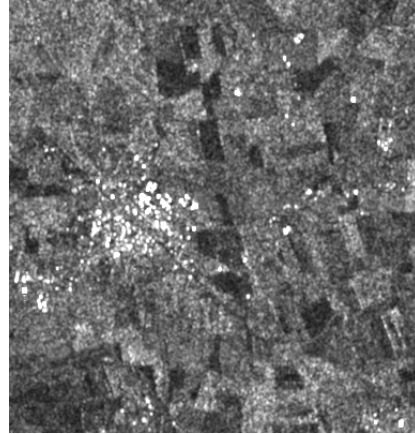


Table A.7: North Sea SAR Image Information

Location : Dessau, Germany
 Date : 07/22/2010 - 09/04/2010
 Band : X
 Acquisition mode : StripMap
 Polarization channel : HH
 Polarization mode : Single
 Resolution : 3 m
 Orbit : Descending
 Angle of incidence : 41.10
 Platform : Terrasar

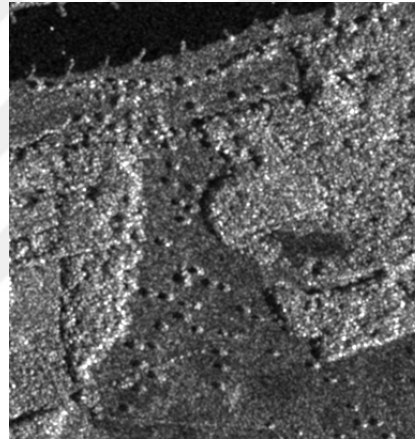


Table A.8: Dessau SAR Image Information

Location : Island Rügen, Germany
 Date : 03/03/2008
 Band : X
 Acquisition mode : ScanSAR
 Polarization channel : VV
 Polarization mode : Single
 Resolution : 18 m
 Orbit : Ascending
 Angle of incidence : 18
 Platform : Terrasar



Table A.9: Rügen SAR Image Information

Location : Island Rügen, Germany
Date : 03/03/2008
Band : X
Acquisition mode : ScanSAR
Polarization channel : VV
Polarization mode : Single
Resolution : 18 m
Orbit : Ascending
Angle of incidence : 18
Platform : Terrasar

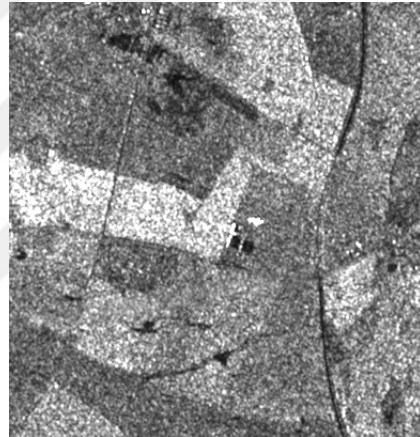


Table A.10: Island Rügen SAR Image Information

Appendix B

METRICS FOR QUANTIFYING SPECKLE NOISE

Measuring despeckling quality is important to for designing a despeckling method. Analysing the similarity between the the reference image and denoised image would help make improvements on the despeckling method. Visual analysis of image despeckling quality is tedious and error prone so lots of image quality metrics which try to correlate with perceived quality are proposed (Rehman and Wang, 2012). The signal-to-noise ratio (SNR), peak signal-to-noise ratio (PSNR), and structural similarity index (SSIM) are the popular quality measures.

Signal to Noise Ratio (SNR)

SNR is a representative reference when measuring ratio of signal level to noise level. In image processing, this representative signal is observed (noisy) image and the reference is noise-free (or noise reduced) image. The signal to noise ratio (SNR) measures relative power between the signal power and noise power. When SNR has a higher value, this indicates that signal is more powerful compared to noise so distortions and artifacts caused by noise occurs in lower amount.

$$SNR = \frac{P_{signal}}{P_{noise}} = \left(\frac{A_{signal}}{A_{noise}} \right)^2 \quad (\text{B.1})$$

where P is average power, and A_{signal} and A_{noise} operates on signal amplitude and noise amplitude such that $A_{signal} = \sqrt{P_{signal}}$ and $A_{noise} = \sqrt{P_{noise}}$. Figure B.1 shows SNR levels when noise increases.

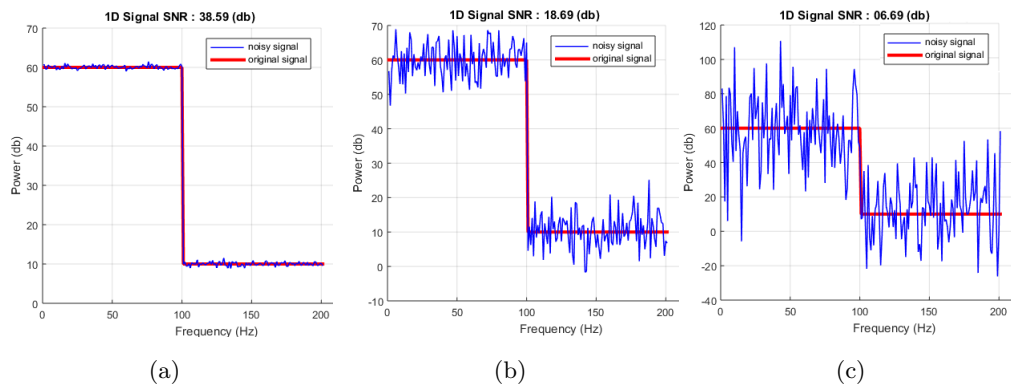


Figure B.1: Noise/SNR: a) low/high, b) mild/average, c) high/low

SNR is also formulated in Equation B.1 using the logarithmic decibel scale:

$$SNR_{db} = 10 \log_{10} \frac{P_{signal}}{P_{noise}} = 10 \log_{10} \left(\frac{A_{signal}}{A_{noise}} \right)^2 \quad (\text{B.2})$$

Peak Signal to Noise Ratio (PSNR)

Peak signal-to-noise ratio (PSNR) is another commonly used image despeckling metric. PSNR measures the relative value between the maximum power of a signal and the power of noise. Since signals may have a large dynamic range, PSNR is usually expressed in logarithmic decibel scale as given in equation B.3 where $MPPI$ is the maximum pixel intensity value in the image.

$$\begin{aligned} PSNR &= 10 \cdot \log_{10} \left(\frac{MPPI^2}{MSE} \right) \\ &= 20 \cdot \log_{10} \left(\frac{MPPI}{\sqrt{MSE}} \right) \\ &= 20 \cdot \log_{10}(MPPI) - 10 \cdot \log_{10}(MSE) \end{aligned} \quad (B.3)$$

Expected value of the squared error loss, known as the mean squared error (MSE), measures the average of the squared difference between the estimated values and what is estimated.

$$MSE = \frac{1}{m n} \sum_{i=0}^{m-1} \sum_{j=0}^{n-1} [I(i, j) - K(i, j)]^2 \quad (B.4)$$

where $I(i, j)$ is noise free image (unknown image we want to estimate) and $K(i, j)$ is approximation of $I(i, j)$ that we found for image with size of $m \times n$. Like SNR, when PSNR has a higher value, this indicates that signal is more powerful compared to noise so distortions and artifacts caused by noise occurs in lower amount.

Structural Similarity (SSIM)

The Structural Similarity Index (SSIM) measures the structural difference between two images. Reference image and denoised image are used for obtaining SSIM value in denoising method evaluation. Reference image, which is generally unknown, is degradation free image which we desire to recover from noisy image. Second image is the denoised image where a denoising method is applied to the noisy image to estimate the reference image. One can say that denoising method performs well if structures of the reference image and denoised image are very similar. In short, when SSIM value increases ($0 \leq SSIM \leq 1$), similarity between reference image and denoised image is increases (Wang and Bovik, 2002). Unlike SNR or PSNR which uses only pixel values, SSIM uses structures which is evaluated using pixel neighbourhood information such as edges or image gradients. Thus, SNR/PSNR and SSIM are complementary measures which should be used together to evaluate the quality of the denoising method (Wang et al., 2004). SSIM equation is given in Equation B.5 as below:

$$SSIM(x, y) = \frac{(2\mu_x\mu_y + c_1)(2\sigma_{xy} + c_2)}{(\mu_x^2 + \mu_y^2 + c_1)(\sigma_x^2 + \sigma_y^2 + c_2)} \quad (B.5)$$

where μ_x is the mean of x , μ_y is the mean of y , σ_x^2 is the variance of x , σ_y^2 is the variance of y , σ_{xy} is the covariance of x and y , $c_1 = (k_1L)^2$ and $c_2 = (k_2L)^2$ are two variables to increase numerical stability (L is the dynamic range of the image, with constraint $L > 0$).

Appendix C

SPARSE MATRICES

In computer science, two-dimensional arrays are used for representing the matrices. For a matrix with size $n \times m$, as much memory as the dimension of the matrix (nm elements) needs to be stored. For some problems, employed matrices can be comprised of mostly zero values, i.e. number of cells with zero values are dominant over the number of non-zero values. Such matrices are called as sparse matrices whereas a matrix contains few number of zero elements is called as dense matrix (Duff et al., 1989). Below, a small example of a sparse matrix $S_{(n \times n)}$ where $n = 9$ is illustrated:

$$S = \begin{pmatrix} -1 & 0 & 0 & 0 & 0 & 0 & 0 & 0 & 0 \\ 0 & -1 & 0 & 0 & 0 & 0 & 0 & 0 & 0 \\ 0 & 0 & -1 & 1 & 0 & 1 & -3 & 0 & 0 \\ 0 & 4 & 0 & -1 & 1 & 0 & 0 & 0 & 0 \\ 0 & 0 & 0 & 0 & -1 & 0 & 0 & 0 & 0 \\ -5 & 0 & 0 & 0 & 0 & -1 & 0 & 0 & 0 \\ 0 & 0 & 7 & 0 & 0 & 0 & -1 & 0 & 0 \\ 0 & 0 & 0 & 0 & 0 & 0 & 0 & -1 & 0 \\ 0 & 0 & 0 & 0 & 0 & 0 & 0 & 0 & -1 \end{pmatrix}_{9 \times 9}$$

Main advantages of using sparse matrices are obtained computational efficiency and lower storage requirement (Strang, 2016). Simply, there is no need to store elements without data and there will no computation for the cells with zero value. Therefore, data is kept as much as it needed which is much more efficient approach. For example, content of a diagonal matrices can be kept in a simple vector (as one dimensional array). If we know that this information is the data in the diagonals of a matrix, we can reconstruct the matrix from that information which is a diagonal matrix. In another words, sparse matrices are very efficient in terms of data compression where various data representations can be used. Thus, almost all algorithms, from the simplest to the most complex compression algorithm, can successfully compress sparse matrices. In addition, it is possible to consider multi-repetitive matrices as sparse matrices (Strang, 2016). Sparse matrices are used in a lot of research areas such as Computer Science, Physics, Chemistry, Geography, and Economics.

Appendix D

EXPLICIT AND IMPLICIT METHODS

Differential equations are heavily employed for modelling various real life problems such as simulating fluid flow and modelling motion of a robot. These differential equations can be an ordinary differential equation (ODE) or a partial differential equation (PDE). Although there are simple real life problems, in general real life problems are highly nonlinear and complex. So generally there is no analytical solution for such complex problems that are modelled using differential equations. Thus, numerical approaches are employed for solving such differential equations.

First step of numerical solution of ODE or PDE is the discretization of the ODE or PDE (i.e. using a finite difference or finite volume method). Generally, this discretization step generates considerable amount of dependent variables that are need to be determined. For the solution of time-dependent ODEs or PDEs, such numerical approaches are categorized as explicit or implicit based on in which way the dependent variables are determined (Ascher et al., 1997). Numerical schemes which define dependent variables as a sets of (system of) equations are called as implicit which are solved using a matrix inversion technique or an iterative technique (see Equation D.2). The numerical method is said to be explicit if dependent variables are directly computed using known quantities (see Equation D.1) (Baraff and Witkin, 2001). In other words, explicit methods calculate the dependent variables of a system at a later time from the dependent variables of the system at the current time in an iterative manner. As a mathematical formulation for implicit and explicit approaches; in below equations, $Y(t)$ is the dependent variable values of the current system, $Y(t + \Delta t)$ is the dependent variable values at the later time, and Δt is a small time step.

$$Y(t + \Delta t) = F(Y(t)) \quad (\text{D.1})$$

$$G(Y(t), Y(t + \Delta t)) = 0 \quad (\text{D.2})$$

Consider the ODE given in Equation D.3 for the comparison of explicit methods versus implicit methods which are given in Figures D.1 and D.2 according to change of step size.

$$\frac{dy}{dt} = -y^2, \quad t \in [0, a] \quad (\text{D.3})$$

where the initial condition $y(0) = 1$, $t_k = a \frac{k}{n}$ for $0 \leq k \leq n$ is the discretization grid, $\Delta t = a/n$ is the time step, and $y_k = y(t_k)$.

Forward Euler method is used as an explicit approach to find y_{k+1} for each $k = 0, 1, \dots, n$ as shown in Equation D.4. Even though Explicit Euler integration is a very simple scheme, it creates numerical instability unless the time step in simulation is small enough. So, the time step $\Delta t = \frac{1}{\sqrt{\text{stiffness}}}$ (Desbrun et al., 1999). However,

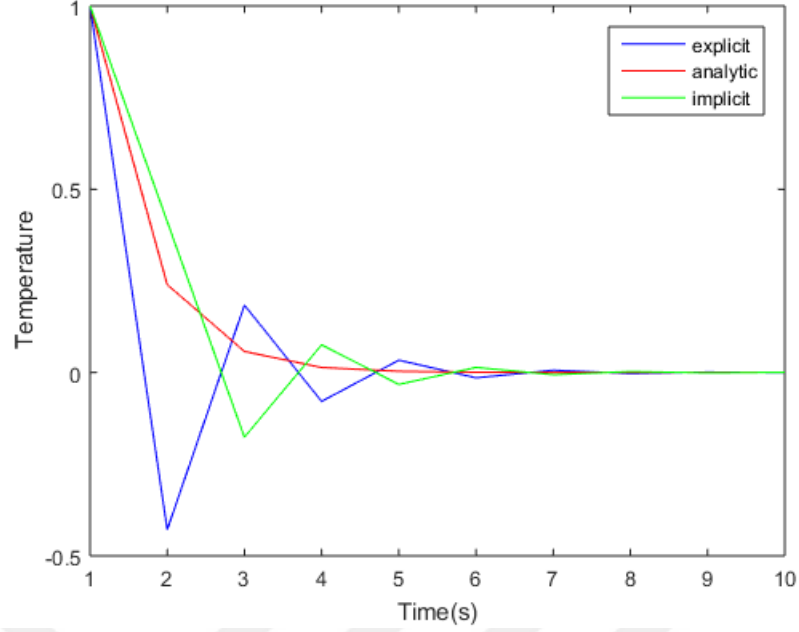


Figure D.1: Explicit method versus implicit method $\Delta t = 1.0$

small Δt values cause extremely longer integration times and also numerical precision of the employed processor may become insufficient.

$$\left(\frac{dy}{dt}\right)_k \approx \frac{y_{k+1} - y_k}{\Delta t} = -y_k^2 \quad (\text{D.4})$$

yields

$$y_{k+1} = y_k - \Delta t y_k^2$$

Implicit Euler integration scheme can be shown as in Equation D.5. To find implicit equation $y_{k+1} + \Delta t y_{k+1}^2 = y_k$ for finding y_{k+1} backward Euler method is used as shown in equation D.5.

$$\frac{y_{k+1} - y_k}{\Delta t} = -y_{k+1}^2 \quad (\text{D.5})$$

Implicit integration schemes are more stable and larger time step can be used (see Figure D.3) while explicit integration schemes are easy to implement and provides better parallelization during the implementation. So, whether to use implicit method or explicit method depends on the goal of the computation.

Also, in nonlinear equations such as contact, it is difficult to predict a future from the past state. So, in these cases, it is recommended that you use the implicit method rather than the explicit method.

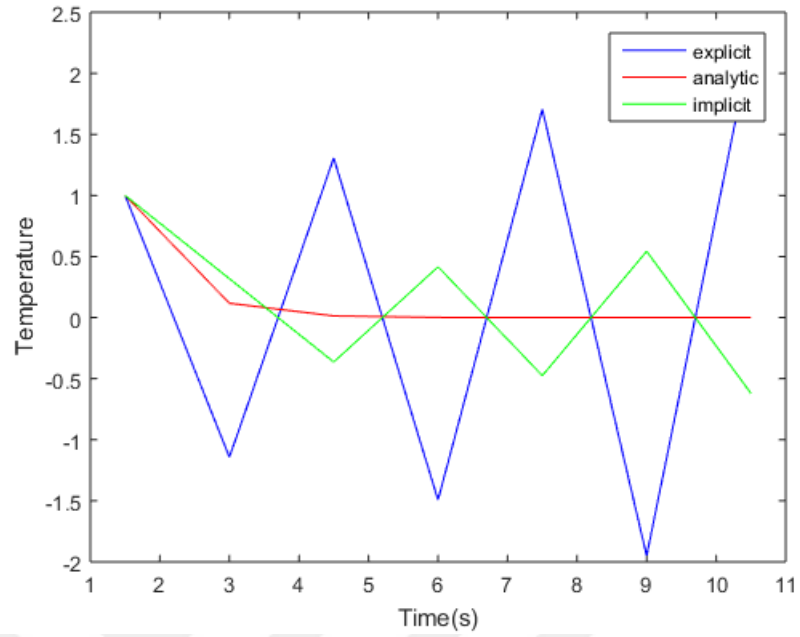


Figure D.2: Explicit method versus implicit method $\Delta t = 1.5$

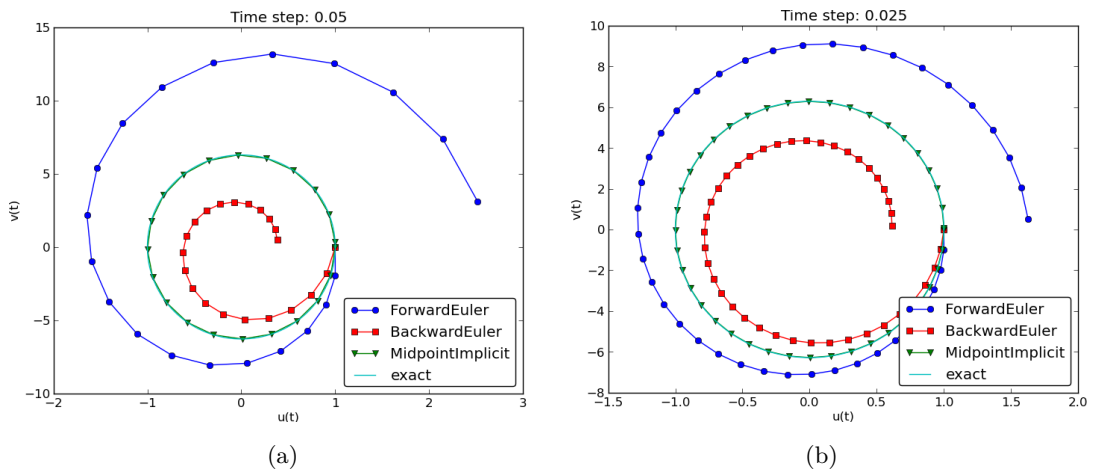


Figure D.3: Comparison of the Forward Euler method and the Forward-Backward Euler method $timestep = 0.05$ and $timestep = 0.025$ (Implicit, 2019)